Quantitative Microscopic Methods for Crystal Growth and Dissolution Processes

Amelia Ruth Perry

Thesis submitted for the degree of

Doctor of Philosophy
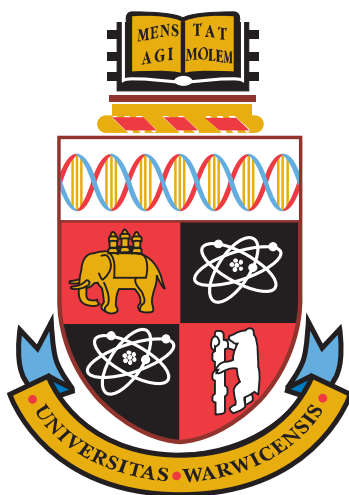
Electrochemistry and Interfaces Group,
Department of Chemistry,
University of Warwick.

April 2015

CONTENTS

LIST OF FIGURES

LIST OF TABLES

DECLARATION AND INCLUSION OF PUBLISHED WORK

This thesis is submitted to the University of Warwick in support of my application for the degree of Doctor of Philosophy. It has been composed by myself and has not been submitted in any previous application for any degree.

The work presented (including data generated and data analysis) was carried out by the author except in the cases outlined below:

- UME fabrication, detailed in Section 2.3.1, was done by Robert Lazenby.

- Figure 4.9 was produced with the help of Maria Adobes-Vidal.

- Some flow cell experiments were performed by Hannah Colledge.

- Experiments detailed in Chapter 6 were performed alongside David Perry.

Parts of this thesis have been published by the author:

Perry, Amelia R., Massimo Peruffo, and Patrick R. Unwin. 'Quantitative plane-resolved crystal growth and dissolution kinetics by coupling in situ optical microscopy and diffusion models: the case of salicylic acid in aqueous solution' *Crystal Growth & Design* 13(2) **2013** 614-622.

Amelia R. Perry, Robert A. Lazenby, Massimo Peruffo, Kim McKelvey, Micheal E. Snowden and Patrick R. Unwin. 'Hopping Intermittent Contact-Scanning Electrochemical Microscopy (HIC-SECM) to Investigate Dissolution Kinetics of Salicylic Acid Crystals in Aqueous Solution' submitted to *Crystal Engineering Communications*.

DEFINITIONS OF ACRONYMS

0.1 Acronyms

AFM atomic force microscopy

API active pharmaceutical ingredient

BCF Burton Cabrerra Frank
    Theory about crystal growth describing how screw dislocations can emerge on a crystal surface from a defect.

CNT classical nucleation theory

FEM finite element method

HDTMP hexamethylenediamine tetra(methylene phosphonic acid)

HIC hopping intermittent contact

IC intermittent contact

KSV Kossel, Stranski and Volmer
    Theory describing the crystal surface as a series of terrace surfaces, ledges and kinks

NTMP nitrilotris(methylene)triphosphonic acid

PDE partial differential equation

PGA poly-L-glutamic acid

PLL poly-L-lysine

QCM quartz crystal microbalance

QRCE quasi-reference counter electrode

RDE rotating disk electrode

SCE saturated calomel electrode

SAM self assembled monolayer

SECM scanning electrochemical microscopy

SICM scanning ion conductance microscopy

SPM scanning Probe Microscopy

STM scanning tunnelling microscopy

UME ultramicroelectrode

VSI vertical scanning interferometry

XRD X-ray diffraction

0.2 Glossary of Symbols

a_j	activity of species j
a	UME radius
c	concentration
d	tip-substrate separation
d_{sp}	spacing of planes in a crystal lattice
D	diffusion coefficient
E	potential
$E^{\ominus}$	standard electrode potential
F	Faraday's constant
F_c	force
G	Gibbs free energy
i	current
I	normalised current
J	interfacial flux
K_a	acid dissociation constant
k_{dis}	dissolution rate constant
k_B	Boltzmann's constant
k_b	backward reaction rate constant
k_f	forward reaction rate constant
k_{sc}	spring constant
K_{sp}	solubility constant
m	mass
n	number of electrons transferred
N_A	numerical aperture
n_{int}	integer number

n_r	refractive index
$\mathbf{n}$	unit normal vector
p	pressure
pK_a	logarithmic acid dissociation constant
r	particle radius
R	ideal gas constant
RG	RG value of electrode
S	supersaturation ratio
T	absolute temperature
u	fluid velocity
$\mathbf{v}$	velocity field
V	potential energy
z	charge on species
α	electron transfer coefficient
θ	angle
λ	wavelength
μ	dynamic viscosity
ρ	density
ϕ	electric field strength
$\omega_\circ$	resonant frequency

ABSTRACT

The aim of this thesis was to investigate crystal nucleation, growth and dissolution processes, focussing particularly on the behaviour of the crystal surface. To facilitate this various methods of microscopy were used, as well as electrochemical techniques, with the goal to separate mass transport towards the crystal surface and the processes which occur close to the crystal surface, and measure intrinsic growth/dissolution rates.

In order to do this, crystal systems were screened for their relevance to applications in industrial processes, and those chosen were related to pharmaceutical crystallization and scale formation in off shore oil wells. For each system, different methods of electrochemical measurement and microscopy were investigated to chose a technique which works best for the problem in hand. Further to the experimental data produced, these were supported by mass transfer models, with the aim of finding out more quantitative information about the surface behaviour of the crystal systems observed.

Firstly, salicylic acid micro-crystals were observed in aqueous solution by optical microscopy to visualise growth/dissolution rates of individual faces. It was found from finite element method (FEM) simulations that the most active (001) face was strongly mass transport controlled, and that the (110) and ($\bar{1}$10) were closer to the surface controlled regime. Salicylic acid crystals were further analysed by scanning electrochemical microscopy (SECM) using 3 dimensional (3D) scans containing a series of approaches to the surface. By inducing dissolution on the crystal surface, and measuring a change in ultramicroelectrode (UME) current, the dissolution rate constant of the (110) face of salicylic acid was determined for this heterogeneous surface.

Barite nucleation and growth was observed by optical microscopy, using a flow cell

with hydrodynamic flow. High supersaturations were used and the crystals were deposited onto foreign surfaces with differing surface charge. It was found that the flux of material, once initial nucleation was achieved, matched closely to simulated mass transport fluxes. Finally, nanoprecipitation was induced at the opening of a nanopipette (ca. 100 nm) diameter and an ion current was applied to induce the early stages of barite nucleation. It was possible to observe nucleation and blockage of the nanopipette from the current transient produced. This process was used to test the effectiveness of different phosphonate inhibitors.

CHAPTER 1

INTRODUCTION

1.1   Abstract

This thesis is concerned with crystal growth and dissolution using methods of imaging and microscopy to focus on the surface and interfacial properties of crystals. In particular, we aim to investigate the effect of mass transport and surface kinetics of all systems studied, which were selected due to their applications to pharmaceutical production, as well as tackling issues encountered as a result of scaling in off-shore oil rigs. Various methods of microscopy will be introduced and the strengths, as well of the shortcomings of each technique will be assessed based on the data obtained. Organic salicylic acid single crystals are analysed during growth and dissolution by optical microscopy to observe their mass transport behaviour, and the surface kinetics

are further probed using scanning electrochemical microscopy (SECM). The nucle-
ation process of barite is observed using hydrodynamic flow and optical microscopy,
and then by following precipitation in a nanopipette using ion conductance.

This chapter covers the principles behind crystal nucleation, growth and dissolution
and outlines the theoretical background of the experimental techniques utilized in
this thesis.

1.2   Crystals

1.2.1   Applications of Crystal Nucleation, Growth and Dissolution

The formation of crystals from solution is a topic which has interested scientists for
generations, but it is surprisingly relatively poorly understood considering this. It
would be of great benefit to many industries to gain a better understanding of the
growth and dissolution of crystalline material in order to control nucleation, size
and morphology of crystals [1], which impacts on other properties; from availability
to strength, for example.

Many biological processes utilize the formation of solid particles, sometimes in an
amorphous state [2, 3], but often a degree of crystallinity is necessary in order for
the 'biomineral' to be strong [4, 5, 6, 7]. For example, the formation of bones

and teeth requires hydroxyapaptite rods [8, 7] to form within an organic matrix to produce a material which can undergo stress and strain readily. The shells of many molluscs are formed from similar matrices containing calcite [9, 10, 11, 12], the most stable form of calcium carbonate [13, 14]. By replicating and understanding the behaviour of these materials in a laboratory settings, we would be a step closer to being able to protect these structures for environmental or personal health. It is also vital to investigate how to inhibit or enhance growth of materials such as hydroxyapatite [15, 16, 17] and calcite [18, 19, 20, 21]. There is also research into crystal growth and dissolution processes of organic materials which occur naturally in biological systems [22, 23, 24]. For example, the investigation of uric acid which contributes towards the problem of kidney stones [25].

In the construction industry the building materials used often contain crystalline materials [26, 27, 28] (in cement or plasterboard, for example) and it is essential to be able to predict possible dissolution processes of these crystals in order to predict how they may weather under various environmental conditions, and if it is possible to slow down these undesirable effects [29]. For example, there has been much research into the dissolution of gypsum [30], the main crystalline form of hydrated calcium sulphate. Gypsum is often used, along with its derivatives, as an additive to cement, giving the material strength and allowing it to set quickly.

The oil well business, as well as construction industries are also very interested in controlling and preventing the nucleation of crystalline materials in situations where

scaling may occur. There is a common problem in oil wells where various kinds of scale appear [31, 32, 33, 34]. For example, gypsum [35], as well as calcite [36, 37], is observed along with other sulphates such as barite and strontium sulphate, and there is great interest in controlling this process by altering the surface effects and the additives present. The problem of barite scale is of particular interest in this thesis and will therefore be discussed later in more detail.

In the fine chemical industries, in particular for the production of food or pharmaceuticals [38, 39, 40, 41] it is necessary to produce crystals built from organic materials [42, 43]. The case of the pharmaceutical industry is analysed in particular in the current study, due to the fact that the pharmaceutical industry contributes to a huge amount of research and development of medicine in the developed world. Oral administration is the safest, cheapest and easiest method of drug delivery, and is therefore also the most popular. In order to control the production of these materials, and to deliver an effective drug dose, it is imperative that the growth and dissolution behaviour and kinetics are well understood. This area is also of great interest to this thesis and will also be described in greater detail below.

A primary goal of this thesis is to develop and apply methods that control the conditions under which crystal growth occurs by drawing on configurations where diffusion (and mass transport generally) in the system is well understood using theories derived from the field of electrochemistry [44]. By doing this we are able to accurately and quantitatively describe the behaviour and kinetics of the systems

being investigated, using mathematical models [45, 46, 47] to further draw out quantitative kinetic information. All systems are visualized using modern microscopic techniques to observe systems on the micro-scale and the nano-scale, techniques where, again, mass transport of the system is well defined or may be easily modelled. Techniques include observation of single crystals by optical microscopy, atomic force microscopy (AFM) [48, 49], interferometry and SECM.

1.2.2 Theory and Background

Supersaturation and Undersaturation

The discussed equations in this section will describe the following generalized crystal system [50, 51], in which A and B are dilute species in an ionic solution, and come together to form a crystal with a formula AB. In an aqueous solution the equilibrium which exist is as follows in Equation 1.1 [51]:

$$A^{m+}_{(aq)} + B^{n-}_{(aq)} \underset{k_b}{\overset{k_f}{\rightleftharpoons}} AB_{(aq)} \tag{1.1}$$

where k_f and k_b are the forward and backward reaction rate constants, respectively. Crystallization is only able to happen when the system has a supersaturation ratio

S of higher than unity. The supersaturation ratio is defined as follows:

$$S = \sqrt[(m+n)]{\frac{a_{\mathrm{A}} a_{\mathrm{B}}}{K_{sp}}} \tag{1.2}$$

where K_{sp} is the solubility product of AB and a_{A} and a_{B} [52, 51] are the activities of A^{m+} and A^{n-} respectively. A solution is supersaturated if it has a concentration equal to, or higher than the solubility product ($S \geq 1$) [53, 51].

Nucleation

Nucleation is defined as a distinct change from one phase to another [54]. In the case all crystal systems discussed in this thesis, this involves a phase change from a solution (phase I) to a solid (phase II) [55] where the driving forces are the concentration [56, 57] (supersaturation, as discussed above) and the surrounding temperature [53]. In order to control the habit of the resulting crystal, it is necessary to understand the fundamentals of nucleation, as these early stages of nucleation and growth have great bearing on the structure of the crystal produced. This is challenging to determine experimentally, as an initial nucleus which defines the phase change to the solid state is approximately 100-1000 atoms in size [57], and therefore it is impossible to observe it's morphology at this stage.

For classical nucleation theory (CNT), the rate of nucleation, J follows the Arrhenius
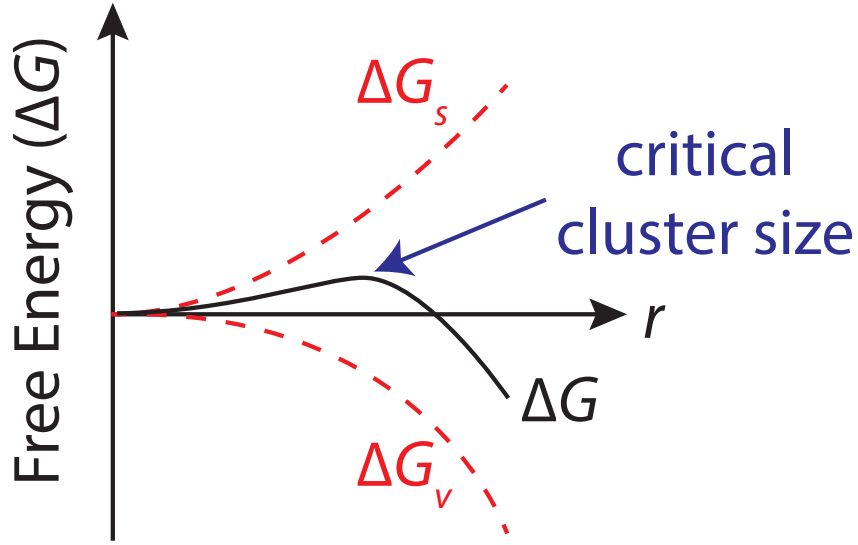
Figure 1.1: Graph showing free energy diagram for nucleation.

form, as described in Equation 1.3 [52, 58]:

$$J \propto e^{-\Delta G/k_B T} \tag{1.3}$$

where ΔG is the Gibbs free energy of the system, k_B is Boltzmann's constant, and T is the temperature. ΔG is equal to the sum of the surface free energy ΔG_s and the volume free energy ΔG_v. This is also illustrated in Figure 1.1. r is the radius of the particle, which is modelled as a perfect sphere (due to a sphere having the lowest possible surface tension, and therefore being the most energetically stable nucleus shape) [58, 59]. ΔG_v is the free energy term for a phase change from liquid to solid and is proportional to the volume of the particle (r^3). ΔG_s describes the free energy change for the formation of the surface, which is proportional to the particle's surface area (r^2). Initially during nucleation the surface energy term will dominate,
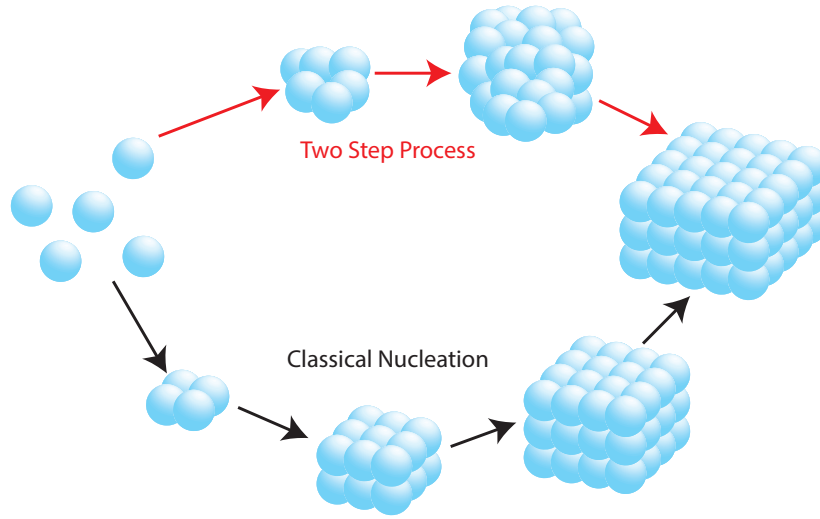
Figure 1.2: Illustration of classical nucleation theory compared to a two-step nucleation process

and cause an increase in the free energy of the system. If the resulting nucleus is larger than the critical radius, $r*$, a value which will depend on the thermodynamic conditions of the system, the activation barrier for nucleation has been overcome, and the nucleus will continue to grow, as the volume term then dominates, causing a drop in Gibb's free energy [54].

CNT has some limitations, in that it assumes that the particles produced are ordered within the modelled spherical particles, in the same uniform fashion as an established crystal. Surface effects are dismissed, which is an important consideration when nucleus size is small [60, 51], and one monomer is added at a time. The two-step process was introduced to amend some of these short comings, and address the fact that nucleation is based on the complexity between kinetic and thermodynamic effects. The differences between these two proposed theories are illustrated in Figure 1.2.

The two-step process describes small, amorphous clusters being formed as a precursor to nucleation of the final crystal structure. These clusters do not have the same crystallinity as the final crystal, and the lack of order means that their structure results in less of a decrease in Gibb's free energy compared to that of the crystalline product in relation to that of the reagent solution. However, kinetically this route is more energetically favourable, due to the fact that the activation energy required to produce these clusters is lower than that required to form a crystalline nucleus from scratch, as described by CNT. It is therefore possible for nucleation to occur by the two-step process even in under saturated solutions, as was observed by Gebauer [61]. This intermediate state is known as a metastable form [62], and also explains why polymorphism occurs; a phenomenon whereby a crystal may have more than one form, and may exist in the metastable form before transforming into a more stable form.

Crystal nucleation can be classified as either heterogeneous or homogeneous [54]. The Gibb's free energy for heterogeneous nucleation ΔG_{het} is lower than that of homogeneous nucleation ΔG_{hom} due to a property known as wetting. In general, a crystal on a surface will have lower surface energy than a crystal in solution, this makes crystal growth more favourable in the heterogeneous case. This gives a larger value for the rate of nucleation [63], which agrees with observation because crystals have a higher tendency to nucleate on imperfections even at much lower supersaturations than is possible for homogeneous nucleation. However, depending on the substrate the energy barrier for nucleation may be higher or lower. Some
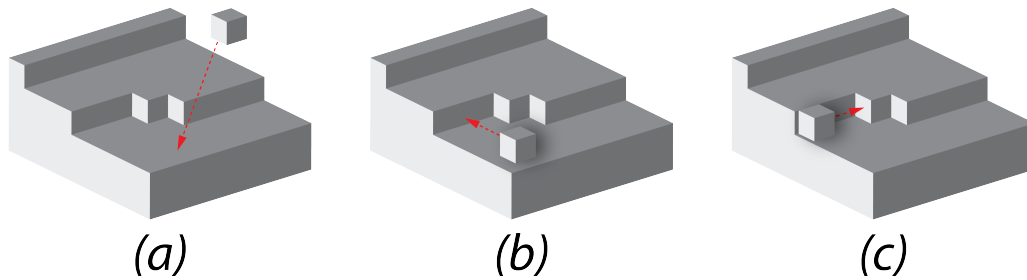
Figure 1.3: Illustration of a growth unit combining with a crystal lattice via the KSV mechanism. (a) a growth unit, depicted here as a cube, diffuses to the terrace surface from bulk solution and becomes adsorbed, (b) The growth unit is mobile on the terrace and migrates to a ledge, (c) Finally, the growth unit is incorporated into a kink on the crystal surface.

surfaces favour the nucleation of a particular crystals, for example, if the charge on the surface allows for a crystal of a particular unit cell to nucleate, but it is possible that a substrate can also inhibit this growth. The effect of surface modification on the habit of crystal nucleation will be further investigated in Chapter 5.

Crystal Growth

In order for crystal growth to occur following the establishment of a crystal nucleus, a series of steps must occur for the incorporation of a growth unit from the solution to the crystal lattice [54, 51, 64, 65]. it is not well understood what the form of this growth unit is, it may be an ion or a molecule, or a cluster of either, and it may vary depending on the system. The first step involves the mass transport of the growth unit from bulk solution to the solid-liquid interface, after which the molecule is adsorbed onto the terrace surface. This is illustrated in Figure 1.3a. It is energetically favourable for the growth unit to do this as it loses one degree
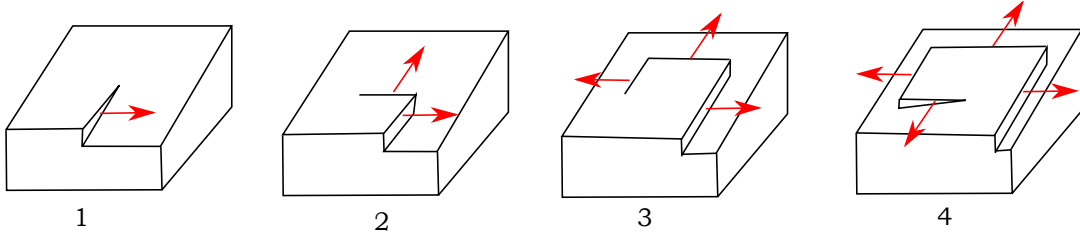
Figure 1.4: Diagram showing how a screw dislocation can form a mismatch in planes

of freedom when it meets the terrace. Further incorporation into the lattice of the crystal then occurs as the growth unit has mobility on the surface terrace, and then attaches to the ledge as illustrated by Figure 1.3b, and loses a second degree of freedom due to the additional point of attachment of the crystal lattice. Finally, the growth unit loses a third degree of freedom by attaching to a kink, as shown in Figure 1.3c [52, 64]. The processes following the mass transport step are collectively described as the surface kinetics of crystal growth. Whichever of these steps is the slowest is the one that determines the rate of crystal growth. In the case of crystal dissolution, the same process occurs in reverse.

As discussed, the most energetically favoured endpoint of a growth unit is to attach to a kink on the crystal surface, and this is generally the mechanism by which crystal growth can continuously propagate by the addition of further units and the production of layers of the crystal. This is known as the KSV model [66, 67, 68]. This theory is further extended by the BCF theory [69, 70, 71] in which crystal growth is modelled as the movement of steps across the surface [52, 56, 72]. BCF theory goes on to explain that a defect on the surface, such as an absent atom, a foreign atom or a missing line of atoms can cause a mismatch in the crystal structure and go on to
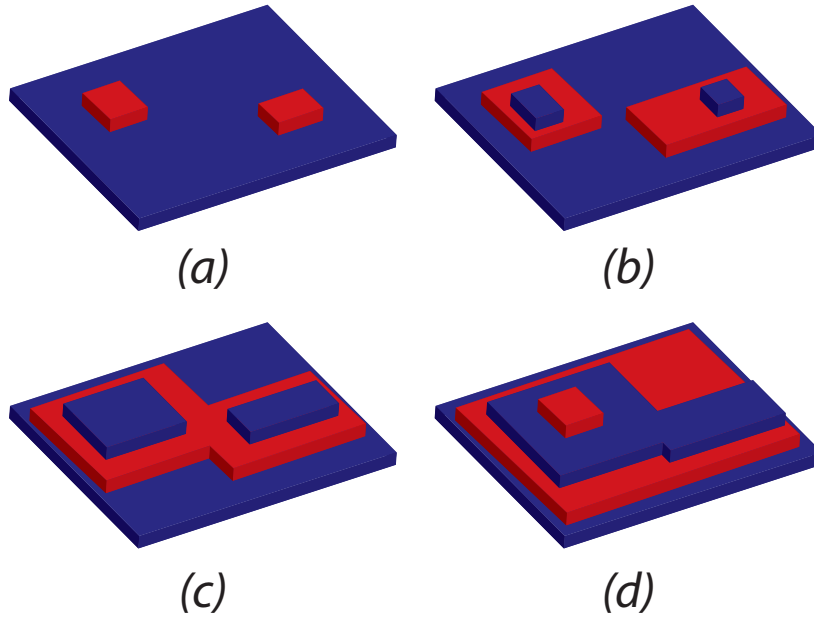
Figure 1.5: Illustration of the birth and spread model of crystal growth, showing poly-nuclear growth

produce a screw dislocation, as illustrated in Figure 1.4. The resulting spiral shape is an infinite source of steps by which crystal growth can occur continuously. Screw dislocations have been observed experimentally by techniques such as AFM [73, 74].

Theories such as Burton Cabrerra Frank (BCF) and Kossel, Stranski and Volmer (KSV) are applicable even in systems with small driving forces, such as low super-saturations. At higher supersaturation, instantaneous nucleation on the surface is also possible, where a nucleus can form on the crystal surface and continue to propagate in two dimensional layers. This nucleus becomes the source of steps. It is also possible to have multiple nucleation sites which then merge, as shown in Figure 1.5, known as poly-nuclear growth [75]. The rate of this microscopic growth, no matter what the mechanism, has great bearing on the growth rate of that face of the crystal

and therefore the macroscopic morphology of the resulting crystal.

1.3 Applications of Crystal Growth in this Thesis

The following subsections will detail the systems of interest in this thesis. In particular, crystals with pharmaceutical applications and the behaviour of a well known organic crystal, salicylic acid, is investigated, and the nucleation and growth of barite, an undesirable crystal form of barium sulphate which grows as a scale in oil wells.

1.3.1 Pharmaceutical Crystals

As discussed in Section 1.2.1, the pharmaceutical industry is responsible for a vast amount of research and development of wide and varied scientific fields. Crystal growth and dissolution is very relevant to the pharmaceutical industry, as many drugs, known as active pharmaceutical ingredient (API)s come in a solid form which is delivered orally and it is regularly the case that a crystalline version of the API is preferable to the amorphous version for higher physical and chemical stability [40]. Crystallizing the drug also makes it purer. Therefore a great amount of research exists which aims to understand the kinetics of growth and dissolution of pharmaceutical crystalline materials.

Fundamentally, an understanding of the growth of crystals is required in order to

control the nucleation and continued growth of the crystal during manufacture. The conditions under which the crystal nucleates will impact on the structure, habit and size distribution of the resulting crystals. Factors which may affect this include the concentration, temperature and pressure of the reaction vessel and the population of already nucleated crystals and the material which the vessel is made of. Also of interest when producing a drug is the dissolution kinetics, as the drug will undergo dissolution upon administration to the patient.

Polymorphism

It is common for organic crystals to exhibit polymorphism, where it is possible for one chemical to have more than one possible crystalline structure [76, 11, 77, 78, 45, 79], affecting the stability, solubility and dissolution rate of the API. It is essential for the drug manufacturer to understand which of these forms are present as their behaviour upon administration vary, as the different crystal shapes may affect the bioavailability of the API. It is possible to control or suppress the growth of a particular polymorph by finely tuning the solvent used, the temperature and supersaturation, or by using additives which inhibit or encourage a particular morphology [80]. As discussed in Section 1.2.2, adjusting the conditions during nucleation can have an effect on whether the nucleation acts via the thermodynamically favourable route, to immediately produce a stable form of the crystal, or if kinetics are more relevant and the crystal may nucleate by first being produced in it's metastable state [62], and over time gaining stability as the stable polymorph. The
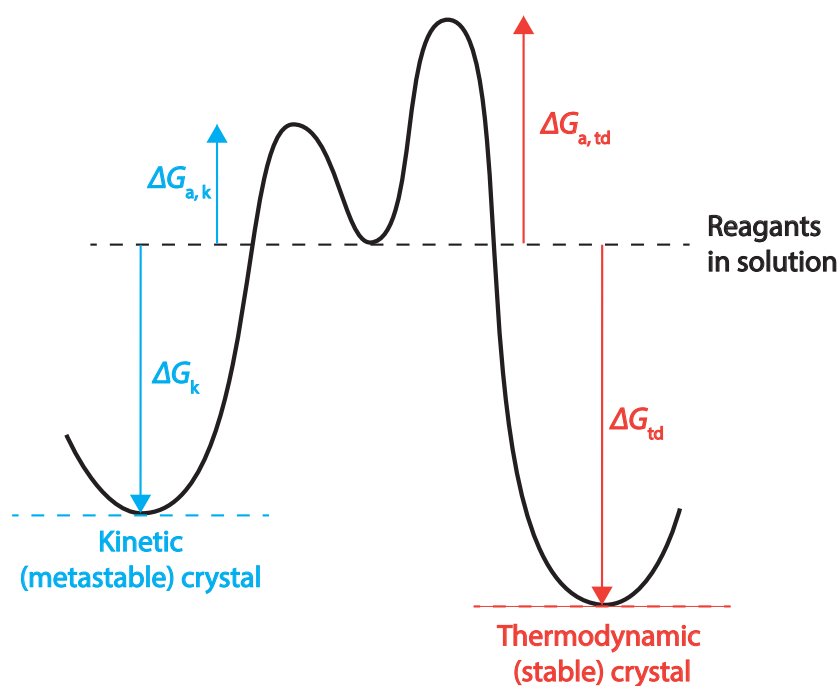
Figure 1.6: Energy diagram showing the energy change for a typical crystal system with stable and metastable polymorphs from nucleation from solvent

Otswald rule describes the series of metastable phases which the crystal will undergo before achieving thermodynamic stability [81].

For many pharmaceuticals it is desirable to produce the most stable form due to its physical and chemical strength making it unlikely to transform during and after manufacture. However, there are drugs which require a metastable form of the API to be administered, due to the typically higher solubility and greater dissolution rate, for more sparingly soluble pharmaceuticals. When this is necessary, a major challenge is to completely prevent the stable form from growing, and prevent transformation from the metastable to the stable drug over time, by choosing appropriate conditions during laboratory crystal growth, and then scaling the process up accu-

rately during large scale plant production[82, 83]. Further discussion on the trials of scaling up production will be discussed below in Section 1.3.1

Cocrystals

As well as using metastable polymorphs to improve the solubility of pharmaceutical crystals with poor bioavailability, various other approaches may be used [84]. Sometimes the amorphous form of the API is used, which has the advantages that it dissolves easily and is more compressible to be easily formed into a tablet. However, as previously discussed, the amorphous form is less chemically and physically stable. One approach is to produce the API as a salt, this can make it more bioavailable, but there are still some APIs which are unsuitable to be formed into salts.

A relatively new approach to this problem is to produce cocrystals, which are multi-component crystal systems which are joined by hydrogen bonds or other non-covalent interactions [84]. The API is combined with a substance which is regarded as safe for consumption, for example a food preservative or a biomolecule, known as the cocrystal former (CCF). A suitable CCF is selected and the cocrystal designed based on the rules of hydrogen bonding by Etter [85, 86]. Although cocrystallization is not yet a concept that is widely used in manufacture of pharmaceuticals, there has been much research into looking at organic cocrystals containing APIs [87, 88, 89, 90]. As with metastable polymorphs, great care has to be taken to ensure that the correct form is produced, especially when scaling up the process in a factory.

Scaling Up of APIs

A major challenge in drug production is the scaling up of crystallization from small scale production in a laboratory where micro-milligrams of the API is produced, to plant production for commercial purposes with resulting kilograms-tons of API [40, 90]. Most crystallization processes in the pharmaceutical industry involve either cooling or the addition of an antisolvent or a reactant. The scaling up must be done in such a way that the properties are reproducible in size, shape, form and purity, and to ensure that this happens at a reasonable cost to make the drug profitable. This is made even more difficult by the fact that the process often has to be adapted to existing vessels which are not custom designed for the particular reaction. The time taken for complete crystallization in large scale production is much longer, as there is a large volume of slurry, and this increases the probability of an undesirable morphology will form. Also when reactants are added to the mix, it is essential that any increase or decrease in temperature is controlled so that the conditions under which nucleation and growth occur are as similar to laboratory conditions as possible. Many industrial crystallizers contain an impeller which rotates to mix the slurry, nucleation on the blades and damage to the existing crystals during stirring is undesirable.

Initial approaches to crystallization on a large scale involves a batch crystallizer [59], which is a vessel containing a large volume with a mixer. The shortcomings of this method are extensive. It is difficult to produce a consistent crystal size distribution

and morphology. The crystals produced during nucleation affect the ease of processes further along drug manufacture, for example during filtration, drying and milling of the finished product.

There is now some move towards to a continuous flow system [59], where a steady state is reached and the reagent or antisolvent is added at various points along the crystallization process [91, 92]. Despite the difficulty in development of this kind of system, they allow for much greater control and efficiency. Continuous processors are typically smaller in footprint and mass of material and for this reason usually cheaper to buy and store. Often in batch crystallizers the drugs will be milled in order to improve the biovailability by decreasing particle size, this agitation can risk a solid state transformation and the addition of a process will increase costs to drug production. They come in two main forms, one where a series of batch systems are used, most appropriate for crystal systems with slower kinetics. They tend to be cheaper and easier to maintain, but are less efficient than plug flow reactors, which continuously flow the material along a single crystallizer, adding the reagent or antisolvent at each stage. These kinds of crystallizer are more appropriate for crystals with faster kinetics which happen over shorter periods of time.

Salicylic Acid

Salicylic acid (2-hydroxybenzoic acid) is a well known pharmaceutical with pain killing effects which occurs naturally in willow bark. In modern medicine, it is
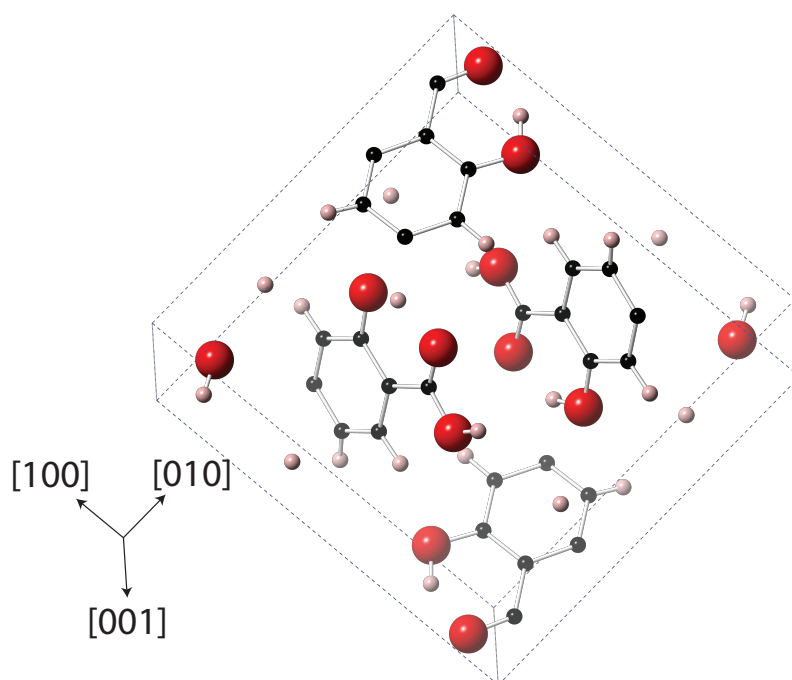
Figure 1.7: The crystal structure of the unit cell of salicylic acid crystals. The white spheres represent hydrogen atoms, black represent carbon, red represent oxygen.

much more commonly seen as its derivative, aspirin (acetylsalicylic acid). However, salicylic acid itself is still commonly used to treat many skin ailments. The crystal structure of the one known polymorph of salicylic acid is monoclinic, and in fact, almost cuboidal with unit cell dimensions of a = 11.52, b = 11.21, c = 4.92 Å, $\beta = 90°50$', as determined by Cochran [93] and further refined by Sundarlingam [94]. The unit cell of salicylic acid is shown in Figure 1.7.

A large percentage of studies into the kinetics of salicylic acid involve batch system [95, 96, 97, 98], similar to the ones used in pharmaceutical production, discussed above. The crude nature of these systems means that crystal nucleation and growth is not well controlled and there is a large variation ion the size, morphology and habit of the crystals produced. These systems are often used to measure bulk crys-

tal growth over time, which means that surface kinetics and mass transport effects are not well separated. It was iterated in some of these studies [96, 95] that the system was mass transport controlled.

A better attempt at separating mass transport and kinetics of the dissolution of salicylic acid was observed by Compton *et al* [99, 100, 101], in their studies which observe planes of salicylic acid using AFM using a hydrodynamic flow cell. In these studies the surface flux was measured and it was suggested that a surface controlled process was in operation. This was questioned in our article [102] where plane resolved kinetics of whole salicylic acid were deduced from a combination of optical microscopy videos and finite element method (FEM) simulations, due to the discrepancy in measured flux and the observation of dissolution in a saturated solution. The work done in that particular article will be detailed in this thesis in Chapter 3.

In Chapter 4 the dissolution kinetics of salicylic acid is further investigated. Here we resolve quantitative rate constants of the dissolution of the (110) face of salicylic acid by measuring the current response when a SECM ultramicroelectrode (UME) is approached toward the crystal surface whilst held at a reducing potential. The theory and background of SECM is covered further in Section 1.5.

1.3.2 Barite Scale

Another system studied in detail in this thesis is barium sulphate ($BaSO_4$). The uses of barium sulphate are diverse, and mostly take advantage of the high density of barium sulphate. It is added to drilling fluid in the production of boreholes, as a radiocontrast agent in radiography, for a 'barium meal', and as a white pigment in paint. However, the interest in the field of crystal growth and dissolution is an undesirable quality; namely barite, the only possible morphology of barium sulphate, forming in oil wells and causing scale and blockages [103, 104].

The unit cell of barite is orthorhombic with a pyramidal point group and dimensions $a = 8.884(2)$ Å, $b = 5.457(3)$ Å, $c = 7.157(2)$ Å; $A = 4$, as is shown in Figure 1.8, as was determined by Hill [105].

Formation of Barite Scale

Barite is rather insoluble in aqueous solution, with a K_{sp} value of 1×10^{-10} [106, 107, 108] leading to the ease of formation even in very low concentrations of barium and sulphate in solution. Of all scales which form in oil wells, barite is one of the most insoluble and resistant to chemical treatments, so research into the prevention and removal of barite is very valuable. Barite formation occurs when the formation water occurring naturally mixes with sea water, which has a high sulphate content.

Traditionally, methods were implemented to remove this scale using mechanical
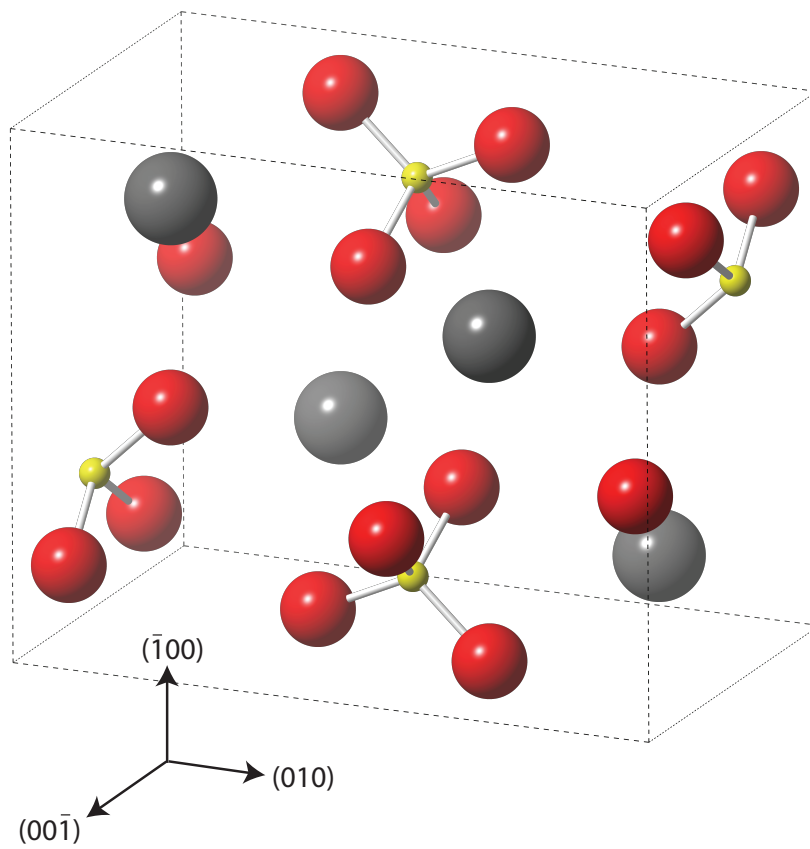
Figure 1.8: The crystal structure of the unit cell of barite. The grey spheres represent barium ions, yellow represent sulphur, red represent oxygen

approaches such as drilling or chemical methods such as removal by acid. Now that the issue is well documented, much research into these systems involve the prevention of nucleation and continued growth of the mineral by functionalization of the surface and using additives which inhibit the process in the formation and sea water. Functionalization is often performed using self assembled monolayer (SAM)s [109, 110, 111]. Chemical inhibitors commonly used include phosphonate [112, 113, 114, 115] molecules to either chelate barium ions in solution, or bind to the emerging crystal structure.

Much existing literature observes nucleation islands of barite by use of AFM [116, 117, 118, 119], but the approaches in this thesis focus on optical microscopy combined with image processing, and the use of a nanopipette to observe nucleation processes of barite particles.

1.4 Mass Transport and Surface Kinetics

During any surface process, the overall rate is dependent on two main processes. The first is mass transport of species to the surface, and the second is the surface reactions required to allow the process to happen [44]. These theories are applicable to both crystal growth and dissolution, and electrode reactions (discussed further in Section 1.5)

Mass transport is described by the Nernst-Plank equation [120] which describes

terms for diffusion, convection and migration (in that order) in the system to calculate the flux, J of species of concentration, c:

$$J = -D\nabla c + uc - \frac{zF}{RT}Dc\nabla\phi \qquad (1.4)$$

where D is the diffusion coefficient of the species, u is the fluid velocity, z is the charge on the species, F is Faraday's constant, R is the ideal gas constant, T is the absolute temperature and ϕ is the electric field strength. Diffusion describes the movement of the species due to a difference in concentration, with a tendency for the species to travel from a high concentration to a low concentration, as described by Fick's 1$^{\text{st}}$ Law [120], as follows:

$$J = -D\frac{\partial c}{\partial x} \qquad (1.5)$$

where x describes a length dimension. Convection is caused by the movement of species due to turbulence in the system, and migration is due to the movement of charged species caused by an electric field.

For crystal growth and dissolution, the process of adsorption and incorporation of growth units is described in Section 1.2.2. For electrochemical reactions involving a redox transformation at an electrode [121], the electron transfer process is described

by:

$$O + ne^- \rightleftharpoons R \tag{1.6}$$

where O is the oxidized species and R is the reduced species, for a process where n electrons, e^- are transferred from the electrode. Prior to this any necessary chemical reactions must occur at the surface and the species may be adsorbed, or approach close to the electrode (at the outer Helmholtz plane) [120, 44]. This adsorption is illustrated in Figure 1.9, as is the formation of the inner and outer Helmholtz planes for cations in aqueous solution, with a negative potential applied to the electrode.

The rate determining step describes the slowest step. For a system where the mass transport is sluggish, it is described as 'mass transport controlled', and when mass transport is sufficiently high that surface kinetics are slow by comparison, the system is described as 'surface controlled'.

1.4.1 Bulk Crystal Growth Studies

There are many studies into crystal nucleation and growth which involve the use of a batch system in which growth can be measured over time, which is comparable to those crystallizers used during the manufacture of the drug [38, 59, 91], as discussed in Section 1.3.1. These systems are informative for identifying general growth trends of crystallization, but are often under strong mass transport conditions. Further-
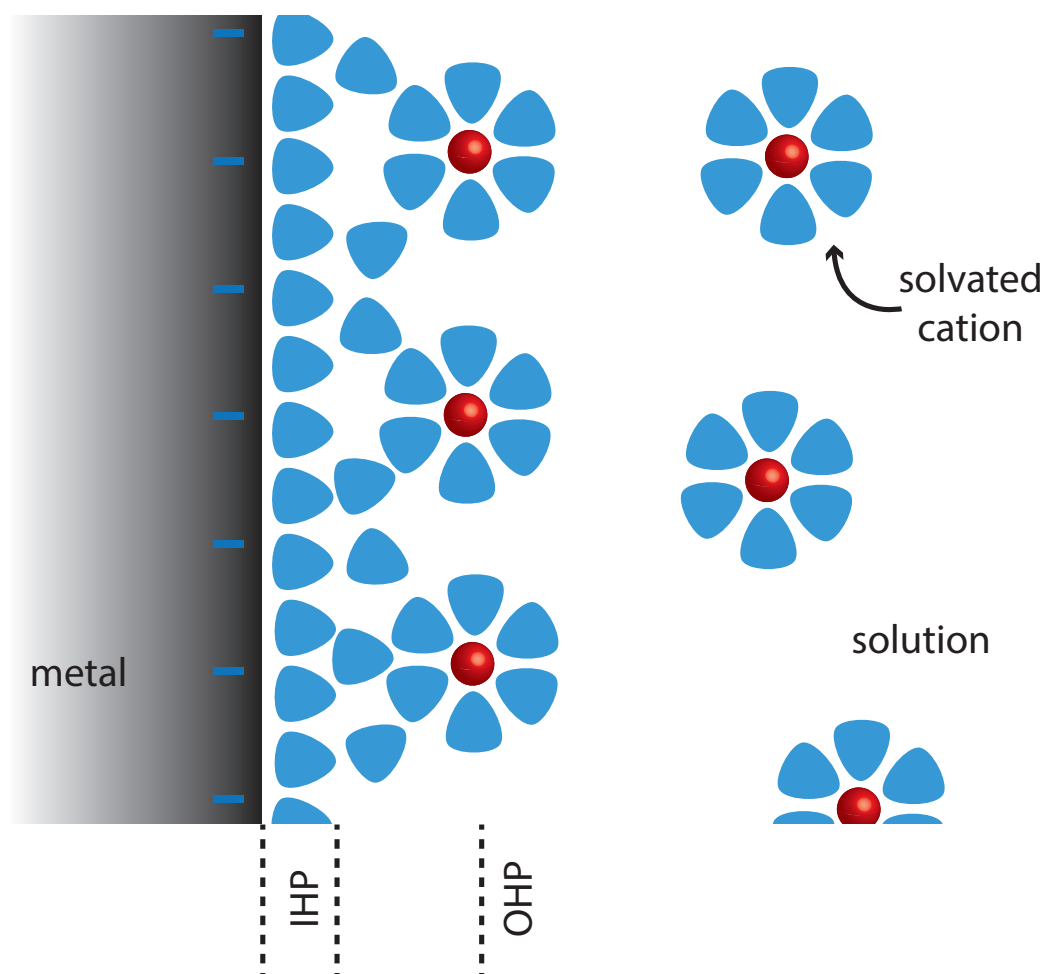
Figure 1.9: Schematic showing the inner (IHP) and outer (OHP) Helmholtz planes for the area close to an electrode surface. Red spheres represent cations in solution, blue rounded triangles represent water molecules.

more, the conditions under which drugs nucleate is not well controlled and it is difficult to determine intrinsic kinetics at all.

1.4.2 Micro-crystals

As was discussed in Section 1.2.2, in order for crystal growth to occur, the first step is for a growth unit to diffuse to the surface of the crystal before being incorporated into the surface. If the diffusion is slow, there is a low concentration of the growth unit on the surface of the crystal due to the fact that the kinetic step can easily keep up with the incoming species. During dissolution, the concentration near the surface will be much higher than in bulk, as is observed by FEM simulations in Chapter 3. This kind of system is known as a mass transport controlled system. The faster the mass transport, the closer the interfacial concentration will be to that in bulk solution. This is synonymous to an electrochemical reaction where the species in solution must diffuse to the surface of the electrode before electron transfer can occur.

The concept of micro-crystals is one which is used to describe a crystal with small dimensions, say of than 100 μm, and is a concept which is derived from the field of electrochemistry and UMEs [44]. If the crystal is larger than this, the diffusion across the surface will be planar and the diffusion will be slow. Both of these cases are illustrated in Figure 1.10. Close to the edges of the crystal, and more so the corners, species can diffuse from the side of the crystal, and mass transport in these

areas will be higher (Figure 1.10a). For a micro-crystal, the diffusion tends towards a hemispherical case as species can diffuse from all directions, and diffusion is high and well defined (Figure 1.10b). In this regime it may be possible to probe and measure surface kinetics and in this thesis, many projects aim to produce micro-crystals with small dimensions [122, 123]. In some systems, different faces of the same crystal may have different characteristics, as the speed of the surface kinetics may vary for different crystal structures. Macroscopically this can (and will) determine the morphology of the crystal [42, 124].
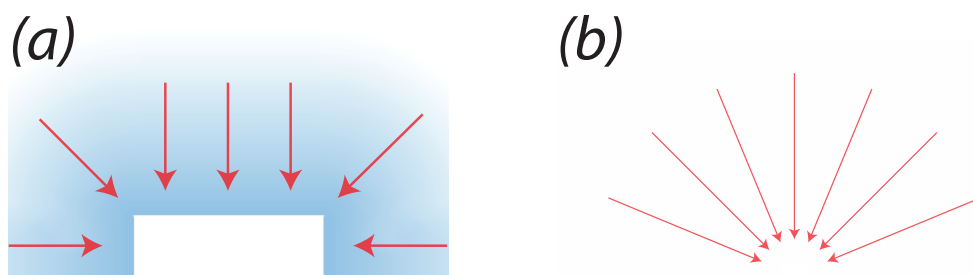
Figure 1.10: Diagram showing the diffusion fields observed for (a) a macro crystal with some planar diffusion and (b) a micro-crystal with a hemispherical diffusion field

Another method often employed to produce higher mass transport is to introduce hydrodynamic flow, for example, by rotating disk method [125, 126] and channel flow method [127, 128] to push the species towards the surface of the crystal. This however has the disadvantage that any kinetics measured are not easy to measure directly, but rather inferred from the perturbation. There are many examples of this in literature, and these are often coupled with another method to monitor the retreat or advance of the crystal, such as some kind of microscopic technique or

electrochemical measurement. An overview of these are detailed below.

1.5 Electrochemistry

1.5.1 Electron Transfer at an Electrode Surface
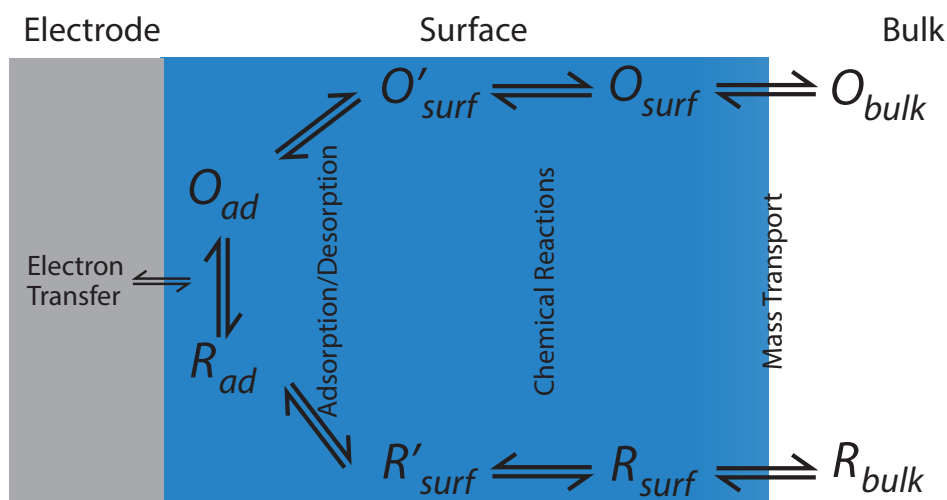
Figure 1.11: Processes which occur close to the surface of an electrode. Adapted from Bard and Faulkner.

Electron transfer processes occur when an electrode is placed in a solution containing an electrochemically active species. By applying a potential to the electrode (with respect to an electrode), the species can undergo oxidation or reduction at the surface, following mass transport. These processes are illustrated in Figure 1.11. As described in Equation 1.6, the redox reaction involves the transfer of an electron for electrode to solution species. If oxidation occurs, it is because the potential is such that the highest occupied molecular orbital (HOMO) has a higher energy than that
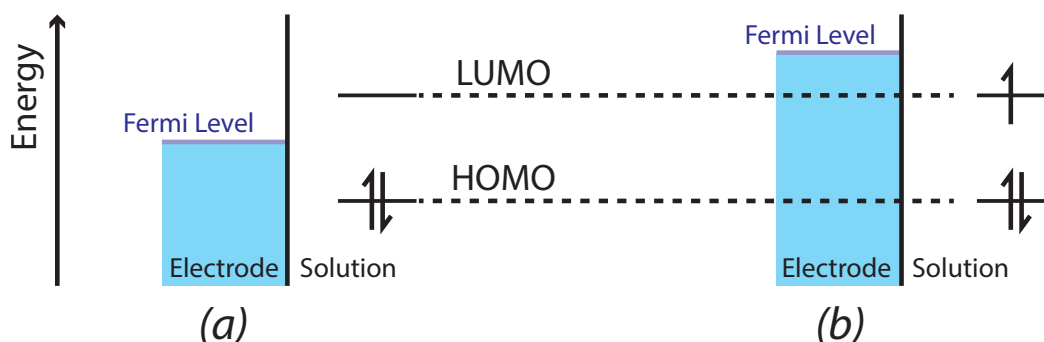
Figure 1.12: Energy level diagram showing (a) case where there is insufficient energy (due to potential applied to electrode) to drive reduction and (b) sufficient energy that electron transfer can occur, as the Fermi level is tuned by altering the potential.

of the electrons in the electrode. When the lowest unoccupied molecular orbital (LUMO) of the electrode has a lower energy than the Fermi level of electrons in the electroactive species, resuction will occur [44]. This is illustrated in Figure 1.12.

When electron transfer is fast compared to the mass transport of the system, the Nernst equation, as follows, is true at the electrode surface:

$$E = E^{\ominus} + \frac{RT}{Fn} \ln \frac{O}{R} \tag{1.7}$$

where E is the electrode potential and $E^{\ominus}$ is the standard electrode potential for the electron transfer reaction in question. When kinetics are more significant, Butler-Volmer equations become more relevant, which describe k_f and k_b for the reaction

in Equation 1.6:

$$k_f = k° \exp{-\alpha \frac{nF}{RT}(E - E^{\ominus})} \tag{1.8}$$

$$k_b = k° \exp{(1 - \alpha) \frac{nF}{RT}(E - E^{\ominus})} \tag{1.9}$$

where $k°$ is the intrinsic rate constant of the reaction and α is the electron transfer coefficient.

1.5.2 Ultramicroelectrodes (UMEs)
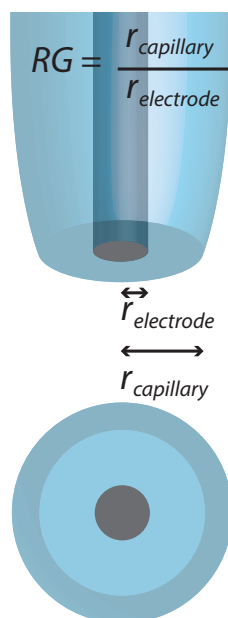
Figure 1.13: Illustration of a UME illustrating what is meant by the RG value.

UMEs are small electrodes which have a diffusive mass transport layer which is

smaller than the size of the electrode. Typically this applies when the size of the electrode is smaller than about 100 µm. UMEs are made in many different geometries [129, 130], but all UMEs discussed in this thesis are disc shaped and embedded in an insulating surface. The RG value describes the ratio between the radius of the active part of the electrode and the radius of the insulating surface, which has a typical value between 2-20 [131]. Figure 1.13 illustrates the definition of the RG value.

Using the same concepts previously described for micro-crystals, the small dimensions of the UME mean that the diffusion field observed is hemispherical and well defined. Mass transport is very high which means that the electron transfer processes on the electrode surface are less likely to be mass transport limited [132]. Low currents are observed when using UMEs and this means that a two electrode set up is adequate, as charge does not accumulate on the reference electrode, causing a change in it's relative potential, with the UME as the working electrode and a reference electrode. Measurements are performed with a high background electrolyte concentration ($100\times$) than that of the redox mediator. For a disk electrode, the limiting current, i_∞, is calculated by solving Fick's 2nd Law, to give:

$$i_\infty = 4naFDc_\infty \tag{1.10}$$

where D is the diffusion coefficient of the species of interest and c_∞ is the concen-

tration of the species in bulk solution (far from any surfaces or other interference).

1.5.3   Scanning Electrochemical Microscopy

SECM is the original electrochemical scanning Probe Microscopy (SPM) technique originally used by Bard in 1989[133]. The tip (probe) is an UME immersed in a solution containing the electroactive species and the supporting electrolyte [44]. The UME is placed very closely to an interface of interest and the electrochemical response is measured. In this thesis SECM is used in an amperometric configuration, which means that a constant potential is applied and the current due to the electrochemical reaction is measured. The current measured near to the surface will depend on which mode of SECM is used. In the experiments described in this thesis, 'induced transfer' is used. It differs from some other modes such as tip collection/substrate generation and tip generation/substrate collection because only the tip (electrode) current is measured. The tip is set to a potential such that oxidation or reduction of the species of interest occurs, which, in turn, may drive a process at a nearby surface. To a varying degree, it is also possible that a reduction or oxidation process can occur at the surface.

Approach Curves

Approach curves are the most simple measurement to take using SECM [134, 135], and involve taking a current measurement at a tip UME as from bulk solution,
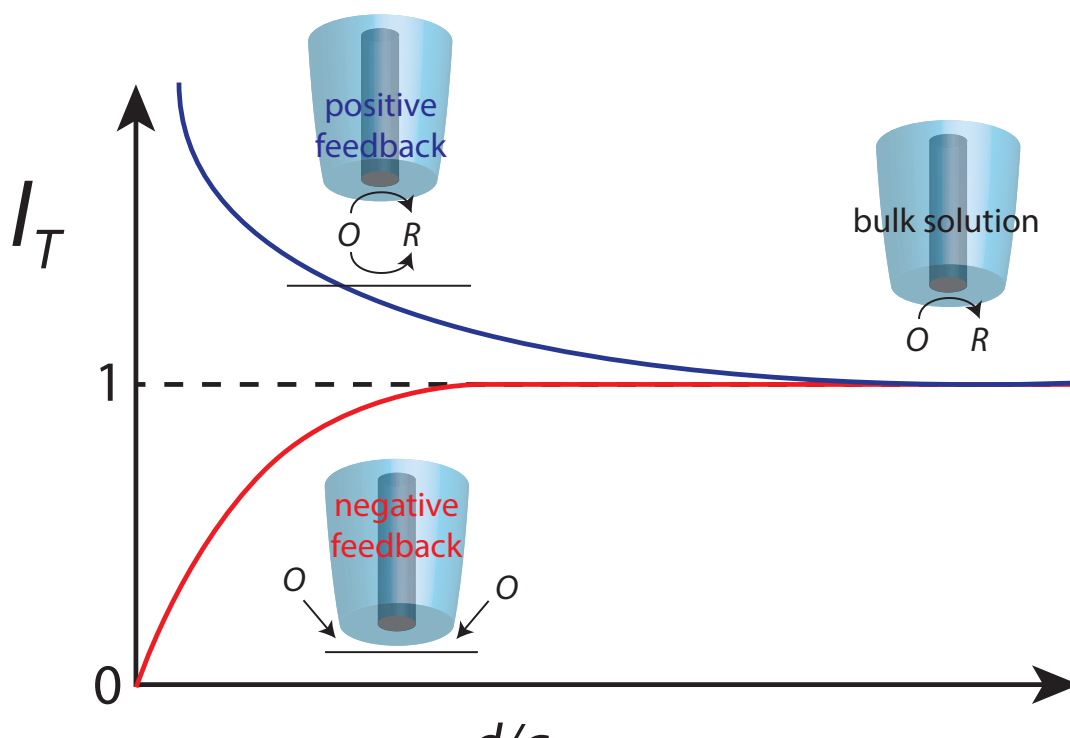
Figure 1.14: Graph showing the normalized current for the cases of positive and negative feedback in SECM. Diagrams illustrating the redox behaviour at the electrode for these cases are also shown.

moving vertically towards the surface [44]. The rate of approach must be sufficiently slow to avoid convection from being induced by the motion, which could affect the mass transport of species to the electrode surface. For an inert surface, the electrode will eventually reach a point where diffusion to the electrode is hindered by having the tip-substrate separation close enough that species can not enter the area close to the electrode as easily. This translates on the approach curve as the current eventually reaching zero for a perfectly aligned tip. If the surface is conducting, the regeneration of tip-generated species at this point will lead to a steep increase in electrode current close to the surface (positive feedback). These two cases are shown in Figure 1.14. A surface may exhibit behaviour which falls somewhere between these

two extremes, especially when regeneration of the species at the surface is a rate limiting step and the substrate has both active and insulating areas [136].

Scanning and Imaging

It is useful to build a 2 dimensional (2D) map of the surface, to measure the activity across the surface [137, 135]. In order to do this, the tip can be brought near to the surface and then scanned in a raster pattern (the tip moves left and right horizontally across the surface at a steady rate, whilst also moving vertically). The simplest form is constant height mode where the tip is brought close, and then scanned at a constant height, as shown in Figure 1.15. However, this is not ideal if the surface and the tip are misaligned or there are topographic features, as the tip moving further from the surface will equate to a change in current which is closer to the bulk value. This means that the contrast of this measured current is much lower between surfaces of different activity. If the misalignment is such that the initial point is a lower than other areas of the scan, it is likely that the tip will collide with the surface and become damaged. There is also no mechanism of determining whether change in tip current is due to topography or activity of the surface. Therefore, constant tip-substrate distance is implemented throughout the scan by a feedback loop [138, 139, 134].

Traditionally this constant tip-substrate separation is achieved by keeping a constant current response. This is only ideal for a surface where the activity is uniform, which,
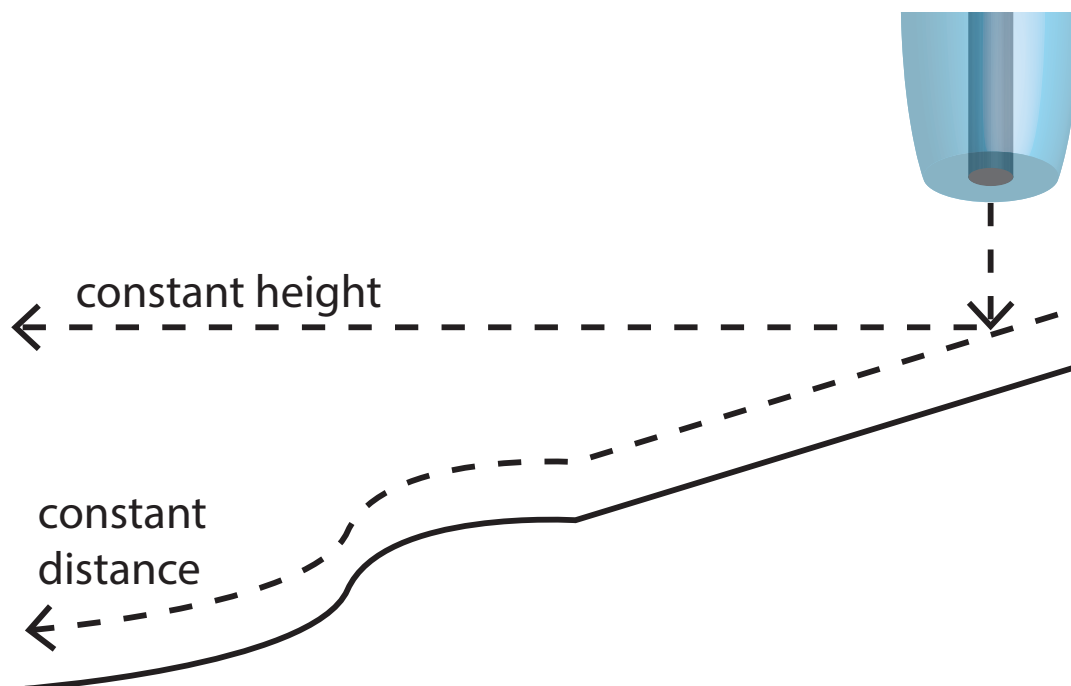
Figure 1.15: Diagram showing the difference between scanning at a constant height and a constant distance.

in reality is unlikely to be the case. In this thesis, intermittent contact (IC)-SECM is used to overcome this issue. IC involves oscillating the UME at a constant amplitude, and approaching the surface. When the tip-substrate separation becomes very low, the oscillation of the tip is damped by the presence of the surface. The reduction in amplitude of the tip oscillation is measured and a feedback loop will use this to halt the approach curve. Throughout the scan the amplitude is monitored and the tip is moved up and down to keep it at a constant value, as shown in Figure 1.16. HIC-SECM (Hopping IC-SECM)[140] is a more modern technique used in this thesis where the surface is mapped by performing a series of approaches in the scan area. This allows the surface, and a 3 dimensional (3D) area above, to be mapped.

UME path

surface

current
response

(a)   (b)
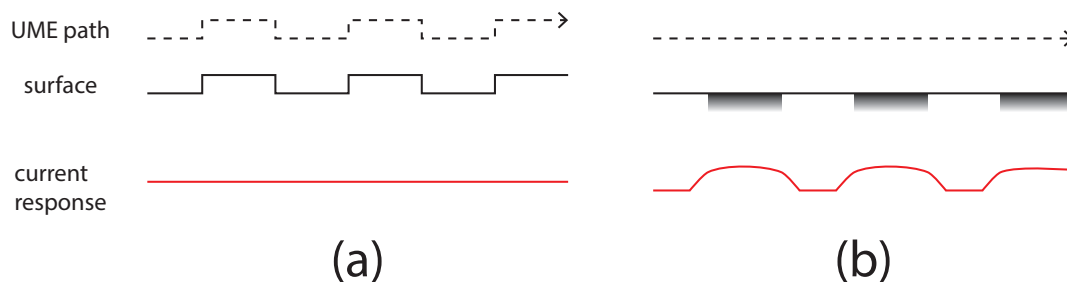
Figure 1.16: The topography, the UME path followed using IC and the current measured for (a) a uniformly active surface with topographical features and (b) a flat surface with electrochemically active regions.

1.5.4 Nanopipettes

Nanopipettes are also used as electrodes in this thesis. These are small pipettes pulled to a fine point which contain an electrolyte solution and a quasi-reference counter electrode (QRCE) inside the pipette, as well as a second in bulk solution, in which the nanopipette is immersed, as shown in Figure 1.17. As with SECM probes, the resolution is improved as smaller tip radii are achieved, but nanopipettes are much easier to fabricate, so smaller tip sizes are achievable, and therefore higher resolution scans to be produced. The method of scanning using nanopipettes is called scanning ion conductance microscopy (SICM) [130], as an ions conductance between the two QRCEs is applied. Therefore, the flux measured is due to migration of species due to an electric field rather than being due to diffusion or convection. SICM is a method which was first implemented by Hansma in 1989 [141].

Various methods are used to maintain feedback of the nanopipettes during a scan, such as using the change in ion current [142] or by using bias modulation, however these scanning methods are beyond the scope of this thesis, as the project included
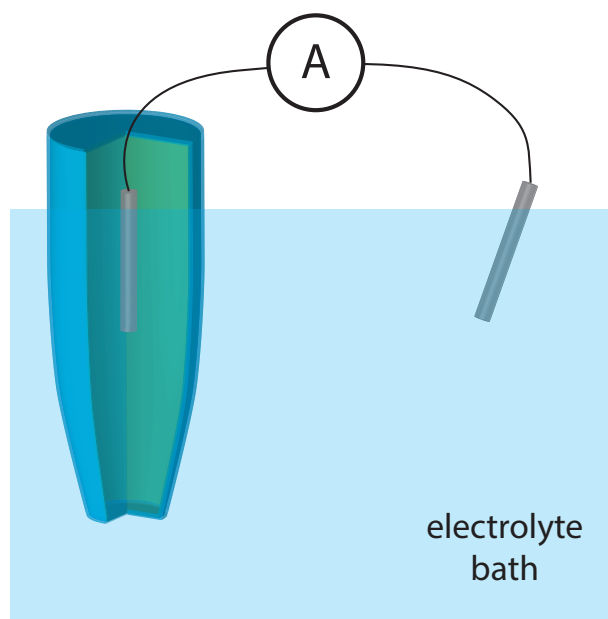
Figure 1.17: Schematic showing the set up for SICM.

which utilises nanopipettes (Chapter 6), does so using current measurements during nanoprecipitation, and is not for scanning purposes.

Nanopipettes, and closely related nanopores, have been used to study a range of systems [143], from biological samples [144, 145, 146], and as is the case in this thesis, crystal nuclei.

1.6 Additional Microscopy Techniques

1.6.1 Optical Microscopy

Optical microscopes allow the user to view a sample at a high magnification which would not be achievable with the naked eye. An optical microscope takes advantage
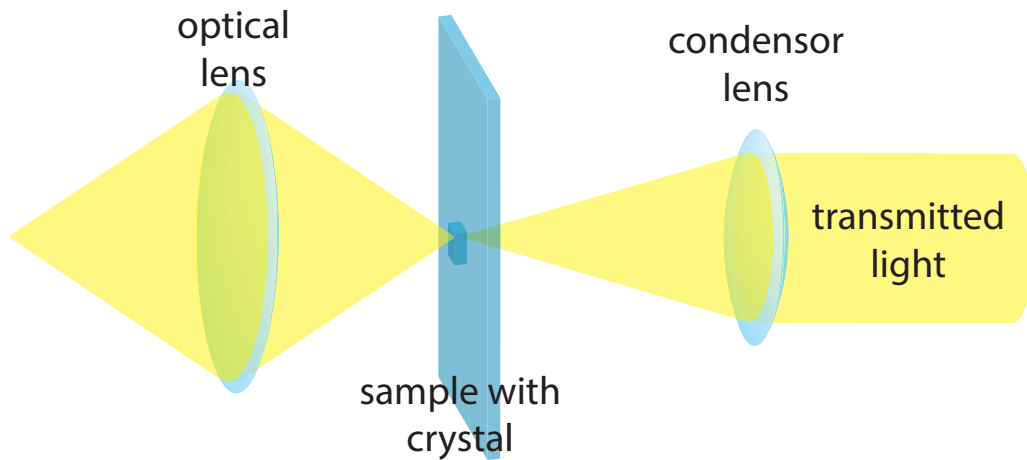
Figure 1.18: Diagram showing how light is transmitted through an optical microscope

of the ability of light to diffract and refract when it passes through lenses [147]. A basic schematic of a wide-field microscope is shown in figure 1.18, showing the most important features. The light from the source first passes through a condenser which gathers the light and focuses the beam onto the sample and then onto the objective lens which creates an inverted image of the crystal. The magnified image passes through the eyepiece where it is magnified to be viewed by a camera (which has an output to a computer screen). It is possible to reflect all light to the camera, to view directly by eye, or half of the light to each.

In place between the light source and the condenser is a field diaphragm followed by an aperture diaphragm. The numerical aperture N_A [148] of any optical system is defined as follows in equation 1.11 and is a measure of the range accepted or emitted

light:

$$N_A = n_r \sin \theta \tag{1.11}$$

where n_r is the refractive index of the medium (in the case of the microscope in air $n = 1$) and θ is the half angle of the cone of light captured by the lens. For a compound microscope the numerical aperture is a summation of the numerical apertures for the objective and condenser lenses. This depends on a value known as the angular aperture for each lens θ_{obj} and θ_{con} respectively [147]. This relationship is shown in equation 1.12:

$$N_A = n_r \sin \theta_{obj} + n_r \sin \theta_{con} \tag{1.12}$$

Because the numerical aperture defines the cone of light accepted or emitted by the lens, it is better to have as large a value as possible. This is because when the objective lens accepts light from over a wider angle a greater amount of light is available to form the image [147].

The resolution of images in optical microscopy is limited by the wave properties of light. When light passes through an aperture it produces a diffraction pattern known as an Airy disk [148]. The intensity profile for a point light source being diffracted in this way is shown in figure 1.19a. When two points are separated by

(a) Intensity distribution of airy disk   (b) Intensity distribution for two points
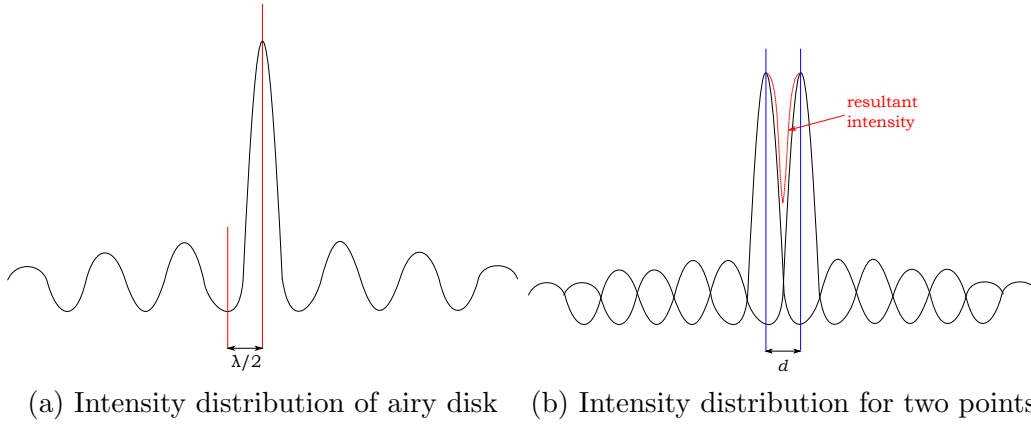
Figure 1.19: The diffraction patterns produced when light passes through an aperture.

a certain distance d_{sep}, the diffraction patterns overlap and constructively interfere as is shown in figure 1.19b. The minimum resolvable separation is as described in equation 1.13:

$$d_{sep} = \frac{\lambda}{2NA} \qquad (1.13)$$

where λ is the wavelength of the light used. This proves that a better resolution may be obtained by either increasing the numerical aperture or decreasing the wavelength used. For the latter reason the electron microscope was invented, as electrons have a smaller wavelength than visible light allowing higher magnification. SPM was a great advance into looking at features on the nano-scale as it does not require light to be used. SPM can provide a numerical insight into the height information of a surface, so that 3 dimensional information may be obtained. This is advantageous for crystal growth because it is useful to gain growth information in all directions.

1.6.2 Interferometry
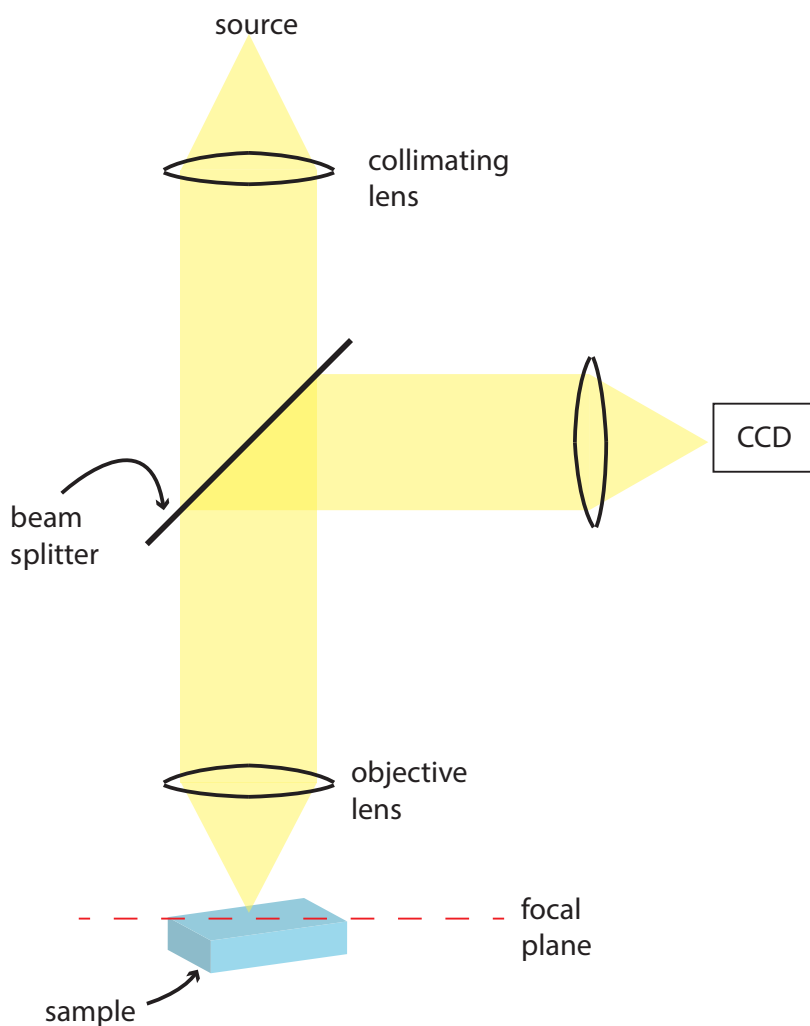
Figure 1.20: Diagram showing a typical interferometer, used to profile surfaces.

In order to profile crystals of slightly higher dimensions (20-200 µm) vertical scanning

interferometry (VSI) was used in the study in Section 3 on salicylic acid crystals. A

typical set up used for surface profiling [149], to reveal surface topography, is shown

in Figure 1.20. The light is typically a point source white light and is passed through

a collimating beam followed by a beam splitter. This is transmitted to an objective

lens which focuses the light onto a sample. Light from both the objective and the source is received by a CCD, if these beams are in phase an interference pattern is observed. This also corresponds to when the focal plane from the objective lens is in line with the surface being profiled. To observe different depths, the objective is scanned vertically using a piezo, and from the corresponding interference at each observed focal plane, a topography map is produced.

1.6.3 Atomic Force Microscopy

AFM is a scanning probe imaging technique developed from the technique of scanning tunnelling microscopy (STM) which relies on the quantum mechanical phenomenon of electron tunnelling [150]. In order for a surface to undergo electron tunnelling it should ideally be conducting, whereas AFM has the advantage that it is easily used to study insulating surfaces [151, 152].

A typical AFM experimental set up is illustrated [153, 150] in Figure [154]. A tip is mounted on the end of a cantilever which has a certain spring constant k_sc given by the manufacturer [155]. The tip is brought into contact with the sample. The sample is mounted on a piezoelectric scanner which allows the tip to raster scan the sample across the surface and alter the height, therefore controlling the x, y and z-directions. As the tip comes into contact with the sample it experiences a deflection l due to the force F_c between the two. This deflection is dependent on the spring constant of the cantilever and is determined by Hooke's law [156] as is

shown in equation 1.14: A typical AFM experimental set up is illustrated [153, 150] in Figure [154]. A tip is mounted on the end of a cantilever which has a certain spring constant $k_s c$ given by the manufacturer [155]. The tip is brought into contact with the sample. The sample is mounted on a piezoelectric scanner which allows the tip to raster scan the sample across the surface and alter the height, therefore controlling the x, y and z-directions. As the tip comes into contact with the sample it experiences a deflection l due to the force F_c between the two. This deflection is dependent on the spring constant of the cantilever and is determined by Hooke's law [156] as is shown in equation 1.14:

Figure 1.21: Diagram showing a typical set up for an AFM

$$F_c = -k_{sc}l \tag{1.14}$$

where k_{sc} is the spring constant of the cantilever. To capture the forces experienced in AFM (pN-nN) the spring constants of the cantilevers used are of the order 0.01-1 Nm^{-1} [155]. This deflection is measured using a laser which is aligned to reflect off the cantilever onto a photodiode. In the case of standard contact mode AFM, the feedback mechanism is employed to ensure that the force between the tip and sample remains constant by adjusting the height (z-direction). This is achieved by the piezo.

A piezoelectric material has the ability to turn mechanical strain into electrical charge, and vice versa [157, 158]. To create a piezoelectric material the material must first be heated up above its Curie temperature [159]. This makes the material exhibit paramagnetic behaviour, where all of the nuclei have a randomly aligned dipole giving no overall magnetization. A direct current (DC) field is applied which makes the nuclei align in one direction. Upon removing the electric field most of the nuclei are stuck, being nearly aligned with where the magnetic field was. This process is known as 'poling' [160]. Compressing a piezoelectric material along the direction of the poling voltage or applying tension perpendicular to this direction generates an electric field in the same direction as the poling voltage, and the opposite directions in the case of obtaining a voltage of opposite polarity to the poling voltage. Similarly this phenomenon is observed in reverse when a voltage is applied to the material. In the AFM scanner there are Piezoelectric scanners to move the sample, one for moving in x and y, and one for moving in the z direction.

Force Curves

The force between the tip and the sample can be modelled using a Lennard-Jones
(L-J) [150, 120] potential energy $V(r)$ (equation 1.15) which is used to describe the
interaction between any two atoms as they come into contact.

$$V(r) = \epsilon \left[\left(\frac{\sigma}{d} \right)^{12} - 2 \left(\frac{\sigma}{d} \right)^{6} \right] \tag{1.15}$$

where d is the separation of the tip and sample and ϵ and σ are parameters defined
by the L-J approach curve shown in Figure 1.22. The d^{12} term describes Pauli re-
pulsion [161] of the two atoms brought into contact; as this happens the electron
clouds overlap and the Pauli exclusion principle prevents two identical fermions from
having identical positions. The d^{6} term represents the attractive forces experienced
by two atoms as they come into contact initially caused by Van der Waals interac-
tions [120]. At a separation of σ the system is in equilibrium between the two forces.
The force is related to the potential by the following expression shown in equation
1.16 [156]:

$$F_c = -\frac{dV(r)}{dz} \tag{1.16}$$

AFM has been developed over the years to adapt to image different samples with
different types of mechanical characteristics. For example, biological samples are
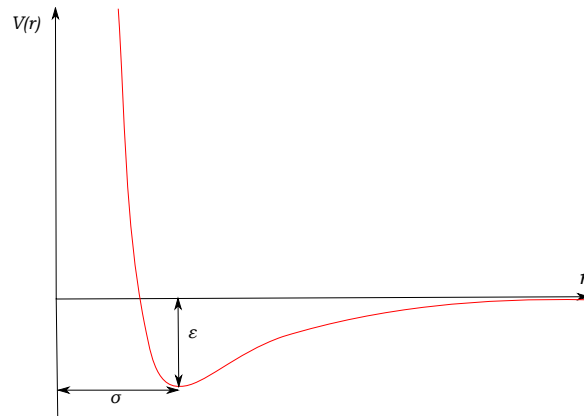
Figure 1.22: Plot showing the Lennard-Jones potential including the parameters σ and ϵ

usual soft and can not withstand large forces as this may cause the material to move around on the surface of the sample, or become ruptured. Crystals often have a robust structure but it is important that during nucleation the crystal is bound to the surface strongly. It is often the case that organic crystals are not as hard as inorganic crystals, this was certainly found to be the case for salicylic acid where preliminary experiments using contact mode AFM in air moved crystals and damage the surface.

Contact mode is the most primitive of the modes of AFM. A constant separation between tip and sample (and therefore constant force) is maintained via the feedback signal. In tapping mode the AFM tip 'taps' the surface with a frequency usually set to be slightly below the cantilever's resonant frequency. The resonant frequency $\omega_{\circ}$ [153] of the cantilever is related to its spring constant k and its mass m by the

(a) Dependence of force during an approach and retraction of the tip.

(b) Dependence of force on distance.
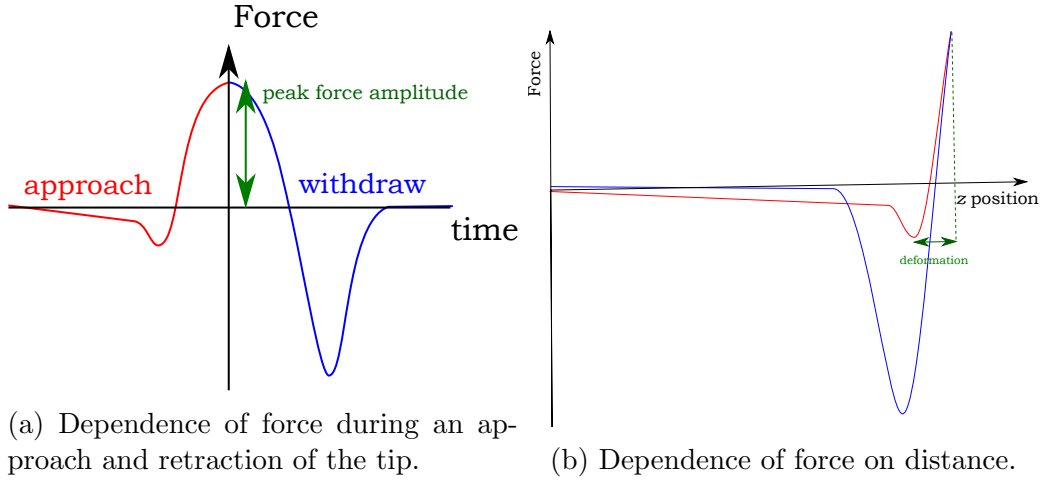
Figure 1.23: Force curves showing the approach (in red) and withdrawal (in blue) of the tip to the surface. Upon approach the force is reduced on initial contact and then reaches a maximum (peak force - in green), upon withdrawal there is adhesion between the tip and the sample.

following relationship shown in equation 1.17:

$$\omega_\circ = \sqrt{\frac{k}{m}} \tag{1.17}$$

Tapping mode [162, 163] is generally better for work in solution, due to the fact that lower shear forces can be utilized; the tip is only in contact with the sample for a short time, meaning that movement in the plane of the sample are minimized reducing risk of tearing or breakage [164]. The amplitude of oscillation is maintained by altering the height of the sample using the feedback mode and the z piezo.

1.7 Modelling

Numerical modelling is regularly used in this thesis as a method of finding numerical simulations, to give information about our system. In particular we aim to find out what transport processes occur in a system and to predict reaction kinetics of an interface. This kind of numerical simulation allows for a system with a complicated geometry, for example, a crystal with an unusual morphology, and allows for multiple physical processes to be considered. Most physical processes modelled require use of partial differential equation (PDE)s to solve them, for example, the transport of diluted species, fluid dynamics and the application of an electric field.

COMSOL Multiphysics is used, which is a program which uses the FEM [165]. It works by first splitting the domain, which is the area which is being modelled, into subdomains. The structure of the subdomains is described as a 'mesh' and usually contains increasingly smaller elements the closer to an area where a physical property changes rapidly, for example, the surface of a crystal or an electrode. Starting with an initial value, given by the user, the software runs a series of iterations whereby a trial function is fitted to the PDE and the error is observed. Through each iteration, the error is minimized. Each PDE is approximated locally with algebraic equations for steady state systems and ordinary differential equations for time dependent models.

The FEM has been applied to many systems related to mass transport in the literature, and features heavily in this thesis.

1.8 Thesis Aims

The primary aim of this thesis is to investigate the growth and dissolution of crystals from aqueous solution which have potential real world applications, and focusing on what happens near the solid-liquid interface and how the growth or dissolution depends on mass transport and surface dissolution kinetics. In order to do this, we choose systems in which the mass transport is enhanced in order to quantify surface controlled systems where possible. We aim to observe these processes using a broad variety of microscopic techniques such as optical microscopy, electrochemical scanning probe techniques, AFM, and interferometry, for example. All techniques are used in a novel way which provides a new way of measuring the properties of crystal systems. Most studies involve the use of FEM simulations to draw out a deeper understanding of the processes measured by microscopy. Due to the large number of processes which occur, for example the application of an ion current, or a hydrodynamic flow alongside the transport of diluted species, this is a valuable method for modelling systems like those presented here.

The first system studied is salicylic acid, which is an organic crystal and is presented within this work as a model pharmaceutical crystal. As outlined above, understanding of crystal systems which have relevance to the pharmaceutical industry is essential for control over crystal morphology, habit and bioavailability. Therefore, it is essential to produce methods which show information about the growth and dissolution properties of organic crystals. Chapter 3 demonstrates this by observing

growth and dissolution of micro-crystals of salicylic acid. By measuring the changing dimensions of the crystals and modelling with the FEM it is possible to elucidate the nature of the surface behaviour on individual planes of the crystals observed. The system is also characterized by VSI and this reveals that some crystals develop unusual hollow features, which are further explained using the results of simulation.

The work on salicylic acid is further developed in Chapter 4, but this time the dissolution kinetics are probed further using IC-SECM, an electrochemical technique which is able to separate the topography and the activity of the crystal surface. The surface is imaged, and a 3D region above the crystal surface is observed, containing a series of tip approaches onto the surface of the crystal. The tip approach is also modelled by FEM simulations and it is possible to predict quantitative surface kinetics of this plane of the crystal by comparing the experimental data with simulations.

The second system of interest is barium sulphate, which produces insoluble barite crystals readily. The barite growth is put into the context of off-shore oil rigs, where a dense, hard barite scale often forms in pipes. Techniques which aim to find methods of preventing the formation and continued growth of the barite particles are the focus of this part of the thesis. The first of these methods is described in Chapter 5 involves using hydrodynamic flow in order to produce high and well defined mass transport to a functionalized surface. Nucleation is observed by optical microscopy and monitored over time to derive the flux of material. This is compared

to FEM simulations to compare to the theoretical flux.

Finally, in Chapter 6 barite nucleation is studied by nanoprecipitation of crystals in a nanopipette like those used for SICM. An ion current is used to drive barium and sulphate ions together in order to observe the initial nucleation of the particle. This method is extended to form a robust technique to monitor the performance of phosphonate additives which are commonly used to prevent the formation of barite scale.

In each case, the microscopy method is assessed to show the strengths of the techniques, and each technique has its own advantages for measuring surface processes, whether that involves the quantitative determination of surface kinetics, or general revelations regarding the mass transport behaviour of the system. Some techniques have the ability to observe single crystals and others allow bulk observations. Whichever the method, it is found to be valuable to combine microscopic methods and simulations to extract a deeper understanding of the system in question.

CHAPTER 2

EXPERIMENTAL METHODS

2.1   Chemicals

All aqueous solutions were prepared using MilliQ reagent grade water (Millipore Corp.) with a resistivity of c.a. 18 MΩ cm at 25 °C. Chemicals used are summarised in Table 2.1.

2.2   Materials

Some of the materials used in this thesis are summarised in Table 2.2.

Table 2.1: Table showing the chemicals used in this thesis, their purity or grade, and the supplier

Chemical	Purity	Supplier
aluminium oxide suspension, 0.05 µm		Buehler
barium chloride ($BaCl_2$)	99.9%	Sigma Aldrich
ferrocenylmethyltrimethylammonium ($FcTMA^+$)		prepared in house
HDTMP	$> 95\%$	Sigma Aldrich
NTMP	$> 95\%$	Sigma Aldrich
PGA sodium salt	$> 99\%$	Sigma Aldrich
PLL	0.01% solution	Sigma Aldrich
potassium chloride (KCl)	$> 99\%$	Fischer
sodium sulphate (Na_2SO_4)	$> 99\%$	Fischer
sulphuric acid (H_2SO_4)	$> 95\%$	Sigma Aldrich
Trizma® hydrochloride	99.0%	Sigma Aldrich

2.3 Electrodes

2.3.1 UME fabrication and characterisation

For SECM experiments detailed in Chapter 4, a UME was used for a working electrode [166]. Silver coated platinum Wollaston wire (Goodfellow), which was a 25 µm Ag with a 2 µm Pt core, was inserted into a borosilicate glass capillary

Table 2.2: Table showing the materials used in this thesis and the supplier

Item	Supplier	Details
Petri dishes	Greiner bio-one	perspex, 30 mm diameter
Glass bottom petri dishes	Willco Wells	for 42 mm diameter cover slips
Microscopy slides	Thermo Scientific	various geometries
Polishing Cloths and paper	Buehler	various materials
Syringes	Becton Dickinson	various sizes used
Filters	Sartorius Stedim/Whatman	0.2 µm/0.02 µm
Microfluidic tubing	Cole Parmer	Various widths used
Microfluidic junctions	Omnifit Ltd.	3 way valves single key, and straight/small bore (0.8 mm)
o-rings	Omnifit	various sizes used

(1.16 mm inner diameter, 2.00 mm outer diameter). The silver coating near the end

of the capillary is removed using a 30 % nitric acid solution. After silver from the

bottom of the capillary is completely removed, excess acid was washed away using

deionised water, and then acetone was used to remove water and dirt. The pipette

is closed using a Bunsen flame. The silver wire near the top of the capillary was

connected by solder to a copper wire for connection, and the unit was sealed using

Araldite. The Pt tip was exposed by polishing using 600 grit polishing paper, and then polished at an angle to achieve an RG value of approximately 10 and ensure that the disk electrode was located centrally in the glass. To make the surface of the electrode flat, it was polished using a 0.1 µm diamond lapping disk (PSA, Buehler) on a spinning hard drive.

The tips were characterised and their radius estimated using FcTMA$^+$ oxidation, and recording the limiting current, i_{lim}, and using the diffusion coefficient, $D = 6.0$ $\times$ 10^{-6} cm^2 s^{-1}, and using Equation 1.10. This was further supported by use of optical microscopy to observe the tips citefan1992permeability.

where n is the number of electrons transferred in the reaction (1 for the case of FcTMA$^+$), F is Faraday's constant, a is the electrode radius and c is the concentration of the redox species.

A commercial reference saturated calomel electrode (SCE) was also used (CH Instruments, UK).

Cleaning of UMEs   Prior to every measurement, Pt disk UMEs were polished using a polishing pad (Buehler) stuck inside a petri dish, immersed in a mixture of alumina and water, rinsed with ionised water and then polished by a pad immersed in water only.

2.3.2 Nanoprecipitation experiments

Two QRCEs were used, one of which was contained in a borosilicate glass capillary (o.d. 1.2 mm, i.d. 0.69 mm, Harvard Apparatus), pulled to a fine point in a commercial laser puller (P-2000, Sutter Instruments) detailed above, using the following pulling parameters: Line 1: Heat 350, Fil 3, Vel 30, Del 220 Line 2: Heat 350, Fil 3, Vel 40, Del 180, Pul 120.

The QRCEs themselves were produced from a silver (Ag) wire (Goodfellow), which had been coated in silver chloride (AgCl) by performing oxidation of Ag in a saturated solution of KCl.

2.4 Sample Preparation

2.4.1 Functionalisation of Glass

Glass surfaces were functionalised in much of the work in this thesis in order to encourage or prevent nucleation of crystals. Glass cover slips (Willco Wells) were cleaned with ethanol and dried with a nitrogen line, and then a solution of 1 mg ml^{-1} poly-L-lysine (PLL) was pipetted onto the glass slide. It is left for approximately 30 minutes and then removed, and the slide was rinsed. This gave a substrate with a positively charged surface.
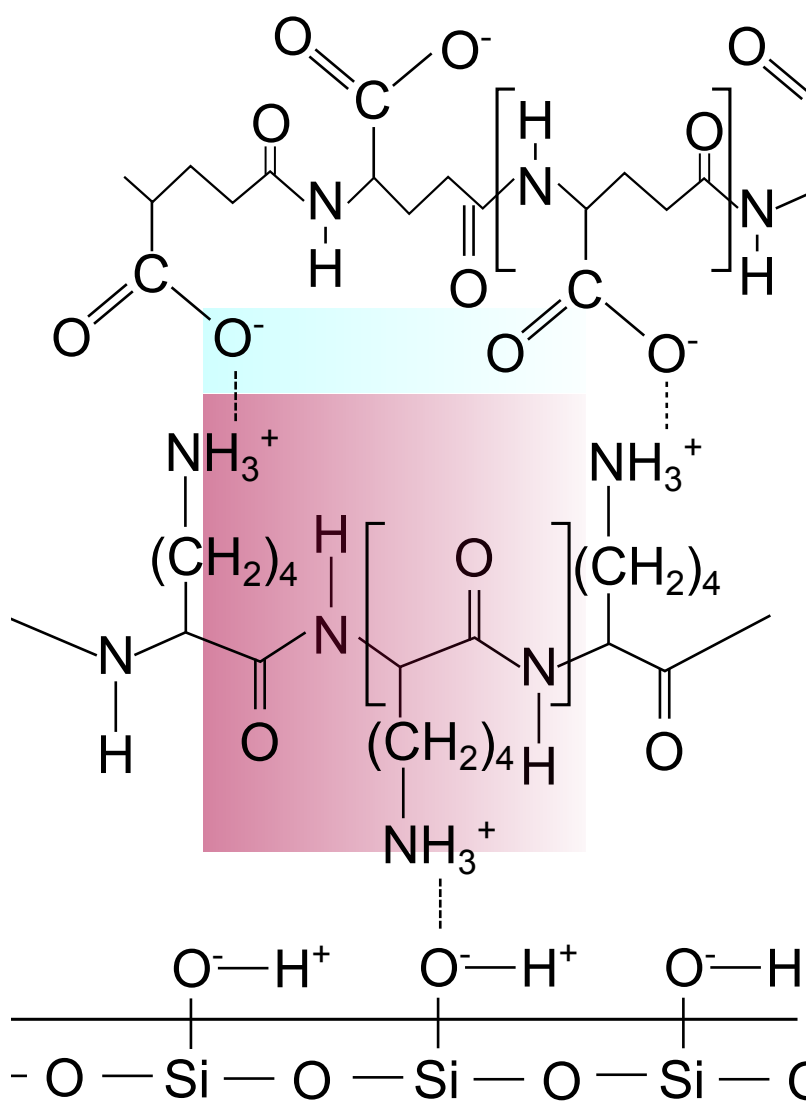
Figure 2.1: Diagram showing how glass surfaces were functionalised with PLL (red area) and then PGA (blue area). Ionic bonds are represented by dashed lines.

To functionalise with poly-L-glutamic acid (PGA), the PLL-coated slides were taken and a 1 mg ml^{-1} solution of PGA is pipetted onto them, and left for a further 30 minutes. Again, the solution was then removed and the slide dried. This produces a glass slide with a strong negative charge on the surface. The mechanism of functionalisation of these two chemicals is shown in Figure 2.1.

2.4.2 Crystal Seeding

In order to seed samples such as those described above, the slides are assembled into petri dishes (Willco Wells) and the relevant supersaturated growth solution is pipetted inside and left for a sufficient amount of time. For example, in Chapter 3, equal parts of 37.5 mM sodium salicylate and 90 mM sulphuric acid were pipetted into the petri dish and left for 45 minutes without perturbation.

2.5 Instrumentation

This sections details instrumentation used for experiments and characterisation throughout the thesis.

2.5.1 Optical Microscopes

In Chapter 3 a Leica DM4000 M microscope was used and time lapse images were captured using Leica Application Suite via a Leica DFC490 digital camera. Images were recorded using bright field microscopy, using a $40\times$ dipping lens. Images were recorded typically once every 30 seconds for a period of either 1 hour or 2 hours.

In Chapter 5 a Zeiss Axiovert 40 MAT is used to record time lapse images using a Pixelink camera and Pixelink Capture OEM software. Dark field images were obtained, once every 15 seconds for a period of 15, 30 or 45 minutes.

2.5.2 Atomic Force Microscopy

AFM measurements were performed on a Bruker Bioscope Catalyst equipped with an inverted optical microscope. The images were obtained using Bruker antimony doped silicon AFM tips (model MPP-21100-10), the rectangular cantilever of which has a spring constant of 3 N m^{-1}. Bruker's NanoScope was used to produce scans. PeakForce tapping mode was used and typical settings are shown in Table 2.3.

Gain and Peakforce setpoint were altered by trial and error to produce a line scan where the trace and retrace matched closely, and signal to noise ratio was reasonably low, as is illustrated in Figure 2.2.
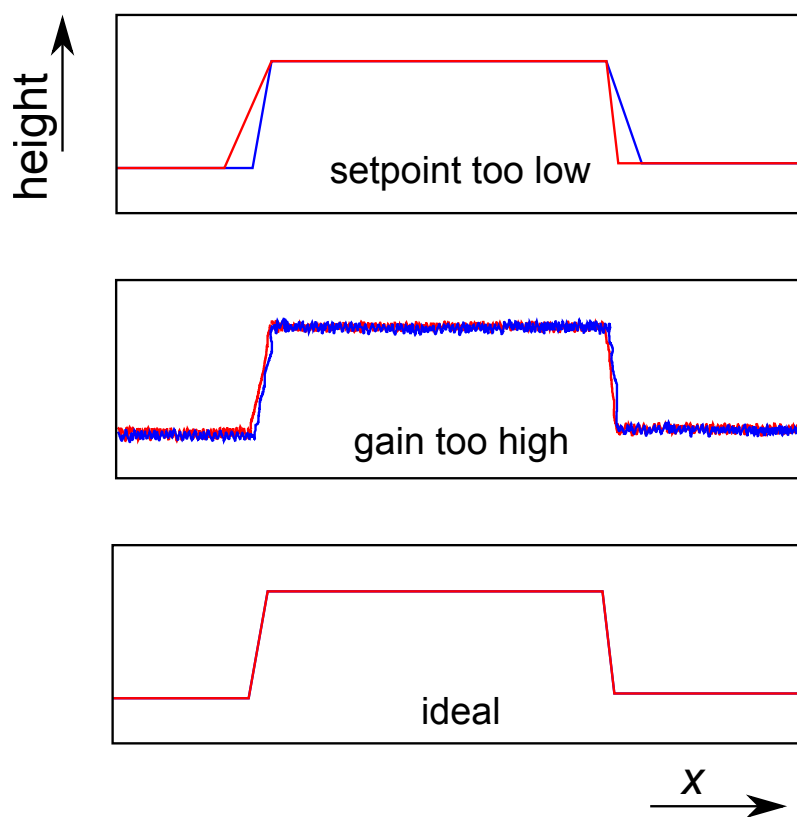
Figure 2.2: Figure showing typical trace (blue) and retraces (red) for a line scan in an AFM image.

Table 2.3: Typical settings used for AFM images which characterise barite particles on a glass slide.

Setting	Value
Scan size	50 µm
Scan rate	0.2 - 0.5 Hz
z-range	5 µm
Samples/line	512

2.5.3 Interferometry

White light interferometry was used to characterise crystals, like the salicylic acid crystals described in Section 2.4, and its use is discussed in Chapter 3. The images produced are 3D and show the topography of the surface imaged. A sample of seeded crystals on glass was sputtered with gold to produce a coating of approximately 12 nm thick (Crystals had a considerably larger dimension of the order of 100 µm). The interferometer used was the Bruker WYKO NT-2000 Surface Profiler, WYKO System, and the 3D images were produced by VSI.

2.5.4 X-ray diffraction

Powder X-ray diffraction (XRD) was performed to further characterise these salicylic acid crystals. The spectrum produced is shown in Figure 2.3. It shows a very strong signal for a peak around $2\theta = 11°$, where θ is the angle at which the X-rays travel with respect to the orientation of the sample. This suggests that the spacing
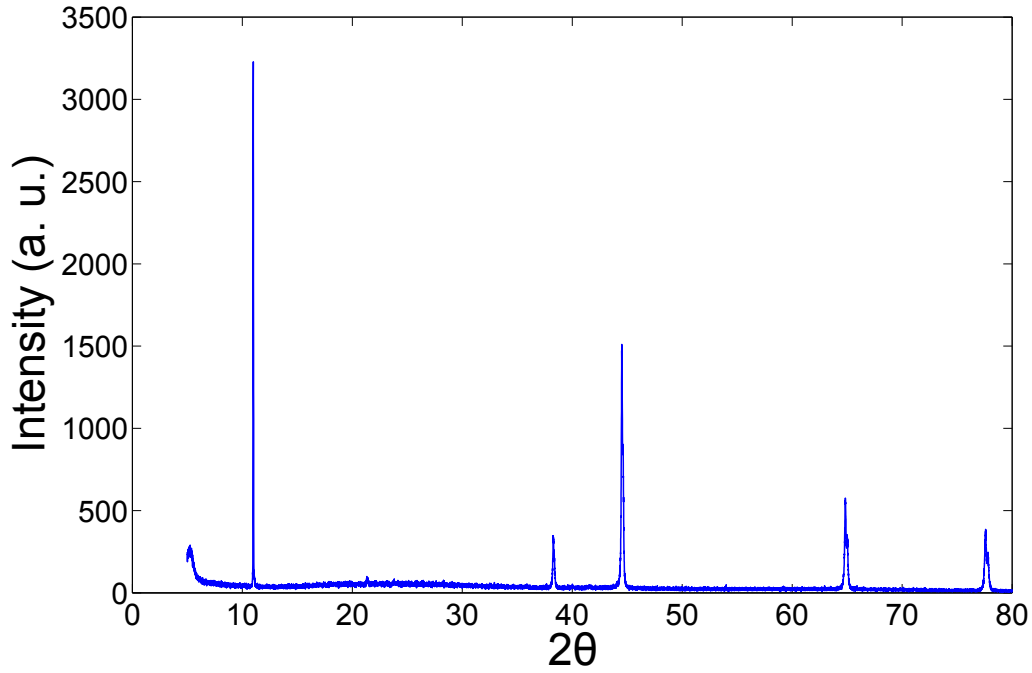
Figure 2.3: Plot showing the results of XRD of a sample of salicylic acid crystals seeded on PLL on glass.

in the crystal lattice, d_{sp}, is 8.05 Å, as calculated from Bragg's law described by Equation 2.1:

$$n_{int}\lambda = 2d_{sp}\sin\theta \tag{2.1}$$

where n_{int} is an integer number, and λ is the wavelength of X-rays applied (1.5406 Å). This gives strong evidence that the typical crystal orientation is with the (110) face parallel with the glass slide. Other visible peaks are known to correspond to the aluminium holder on which the sample was mounted, there are no other peaks which seem to account for other faces of the salicylic acid crystal.
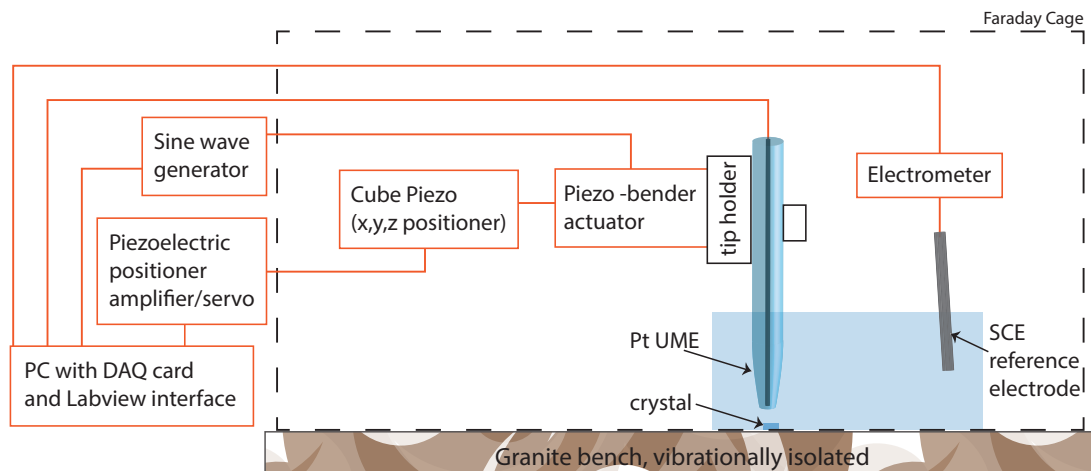
Figure 2.4: Schematic showing the set-up for IC-SECM.

2.5.5   Electrochemistry

SECM set up   The instrumentation used for hopping intermittent contact (HIC)-SECM experiments is shown in Figure 2.4. It is modified from a recently reported set-up [167], in that there was a piezo-bender actuator (PICMA P-871.112, Physik Instrumente) with a strain gauge sensor, on which the SECM tip was mounted. Coarse control of the SECM tip was realised using manual micrometers mounted on the stage, in x, y and z. In order to aid placement of the SECM tip prior to scanning, an inverted optical microscope, on which the stage was mounted, was used (Axiovert 25, Zeiss). This allowed for visualisation of the UME tip in relation to the surface of the crystal.

Fine control in x-y-z was achieved by the piezoelectric positioner (P-611.3S Nanocube, Physik Instrumente), which was able to move within a range of 100 µm $\times$ 100 µm $\times$ 100 µm, in closed loop operation. Therefore, it was necessary to have the tip within this range
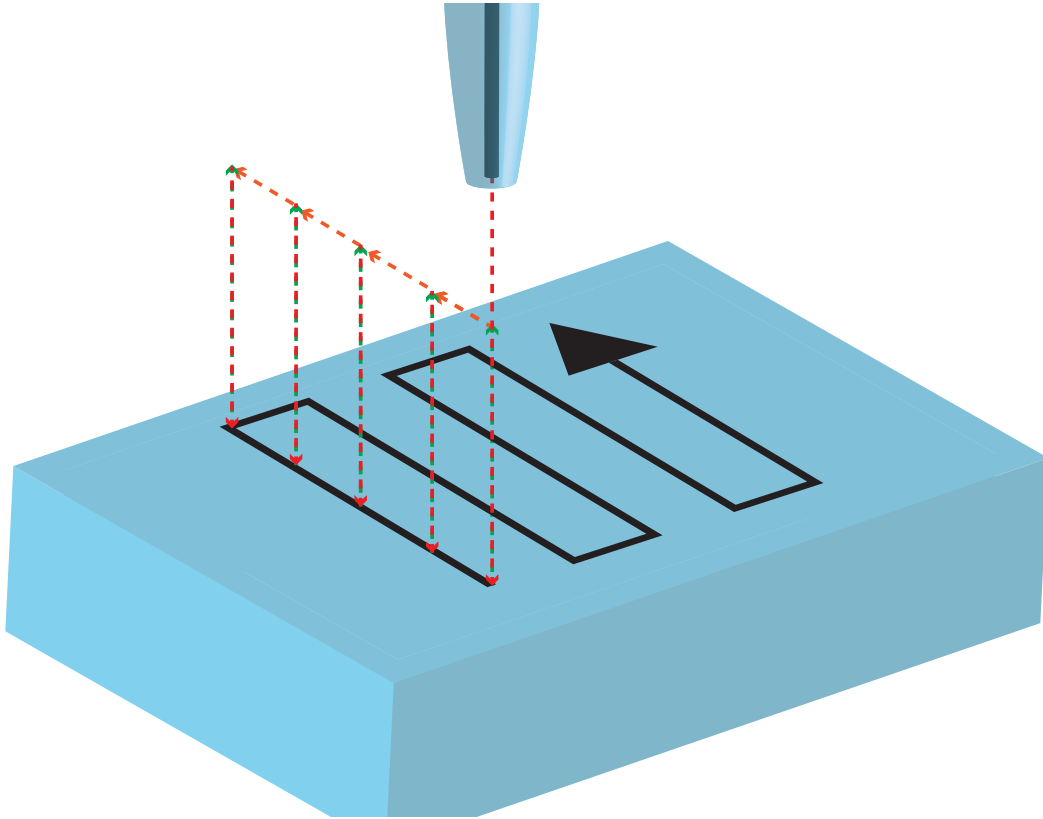
Figure 2.5: Schematic showing a hopping mode scan.

before a full hopping scan on the surface could be produced. The piezoelectric posi-

tioner was controlled through a data acquisition (DAQ) card (PCIe-6259, National

Instruments) from a PC running a custom LabVIEW code (LabVIEW 9.0, National

Instruments). The tip was oscillated using a sine wave generator (Digimess TG100,

Digimess), which was applied to the piezo-bender actuator.

HIC-SECM is a method of scanning which relies on IC, as is discussed in recently

reported work [140]. It is illustrated in Figure 2.5. The tip UME was oscillated at

a frequency of 70 Hz, and the piezoelectric positioner moved the tip in z, closer to

the substrate at a rate of between 50-100 nm s^{-1} (See longest red, dashed line in

Figure 2.5). During this time the oscillation amplitude is measured, and is usually of

the order of 40 nm for a 2 μm Pt UME. When the oscillation amplitude falls by 10 %
for 3 consecutive measurements the approach is paused and the tip is retracted in z
(See the green, dashed line in Figure 2.5) by a given value (5 μm for the experiments
performed in this thesis). The tip is then moved to the next position in x-y (See the
orange, dashed line in Figure 2.5) and another z approach occurs, this is repeated
for a scan which follows a raster pattern (raster pattern on crystal is shown by solid,
black line in Figure 2.5).

2.5.6 Flow Cells

Flow cell experiments discussed in Chapter 5 are used for high supersaturation
measurements of barite nucleation. The delivery system and flow cell is described
here.

Delivery System The delivery system consists of two 60 ml syringes (Becton
Dickinson) on a dual driven syringe system (KD Scientific). One syringe contained
barium chloride, and the other sodium sulphate. From the syringe system, a filter
and then a straight teflon junction was placed and attached to teflon tubing. This
tubing was connected to a T-mixer (Omnifit) for mixing of the solution in equal
parts, resulting in a supersaturated solution able to drive homogeneous nucleation.
The syringe pump was set to flow material from the syringes at a rate of 1 ml min^{-1}.
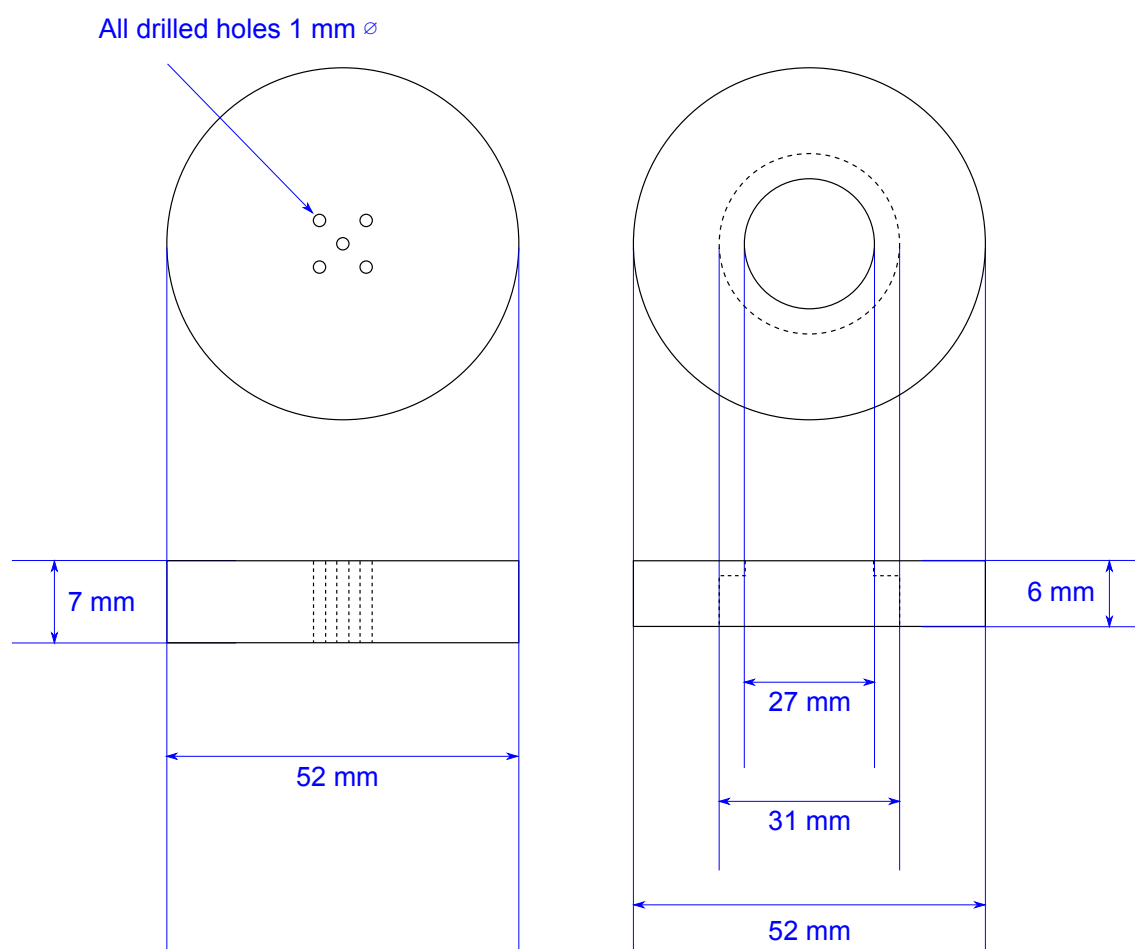
Figure 2.6: Dimensions of the flow cell used for barite nucleation experiments.

Flow Cell   The flow cell was built in house from a teflon block. It consisted of two cylindrical pieces of teflon, one of which had 1 central hole drilled for the inlet, and four additional outlets through which waste material flows. The second piece of teflon had a circular hole in the centre through which the nucleation was viewed, as this was where the glass slide was placed. It also contains a recess in which an o-ring (Omnifit Ltd.) sits to form the chamber of the flow cell. The precise dimensions of the flow cell are shown in Figure 2.6.

2.6   Software

2.6.1   Finite Element Method Simulations

In many studies in this thesis, the FEM is used in order to produce simulations of the systems, as was described in Chapter 1. As was discussed earlier, FEM is so called because it involves creating a geometry which is broken down into elements which make up an overall mesh of the model. In the case of this thesis, all 3D models consist of many tetrahedral elements, and all 2D models are made up of triangular elements. A PDE is solved at each node of the mesh, and a higher density mesh (smaller finite elements) gives a higher resolution. However, this comes at a computational cost, and a challenge of building an effective model is to manage the trade off between these two factors. There are various ways in which we handle this, for example, where possible any symmetry in the geometry is represented in the model, which
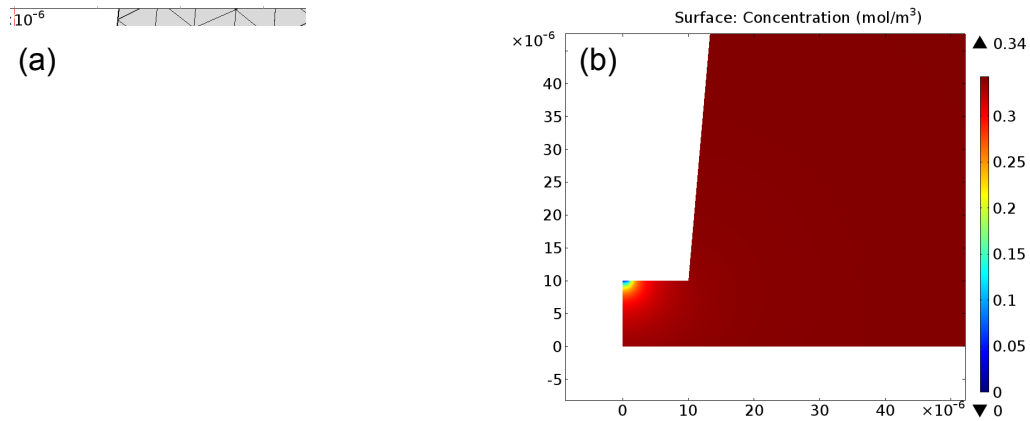
Figure 2.7: Plots showing a typical mesh inside a FEM geometry (a) with high density close to boundaries where there is expected to be a high flux. This model shows a UME in solution above a dissolving crystal surface. Boundaries which represent the dissolving crystal and the electrode surface has a higher mesh density. A 2D concentration plot is also shown (b), it can be seen that there is a large change in concentration of species near to the electrode surface.

allows for a smaller model to be produced. In the models in this thesis, a higher mesh density is applied close to areas of the model where there is a large change in conditions. For example, if there is a part of the model which has a large change in concentration, or a strong hydrodynamic flow, a higher mesh density is applied to those particular boundaries (See Figure 2.7.

Typically, the mesh density of the model is gradually increased and relevant parameters are measured. When increasing the mesh density has no considerable effect on the results of the model, or, where possible, the results closely match theoretical conditions, the mesh density is deemed suitable.
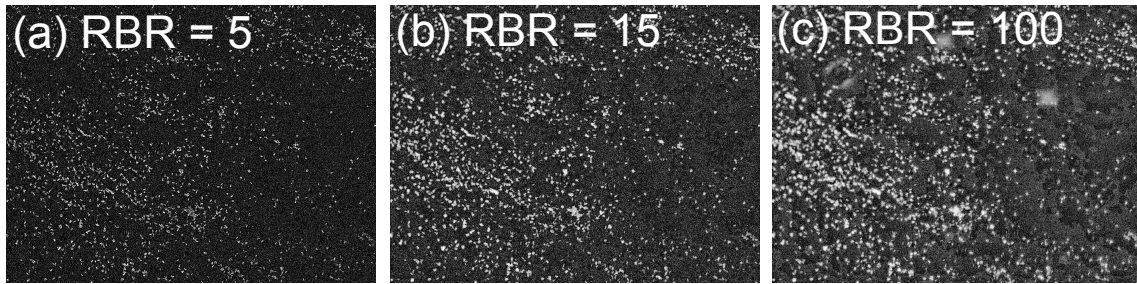
Figure 2.8: Grey-scale images showing the effect of changing the rolling ball radius when performing a background subtraction. RBR in pixels is shown labelled for each image.

2.6.2 Image Processing

In Chapter 5 we outline how we analysed very large sequences of images in order to produce an accurate particle count throughout the sequence. In order to isolate the particles reasonably the images were recorded using dark field microscopy. This meant that all particles were lighter than the background, making background subtraction of the image simpler. Image J was used to do the image analysis, using a Macro with a for loop to run through the entire sequence.

Initially the image was converted to an 8-bit image, as it makes image processing more straightforward than having a RGB image, and the image does not have a colour component. In the sequences analysed, any colour in the image is unimportant for the particle analysis. Then the background was subtracted from the image where a dark background is assumed, and a rolling ball radius of 15 pixels was used (the scale of the image is 3.313 pixels/µm, as measured from a sample of gold bands with known dimensions, to calibrate), this defines the smallest particle size which is picked out from the background. If the rolling ball radius is set too low then extraneous noise is counted, and if it is much larger than the particle size, the background
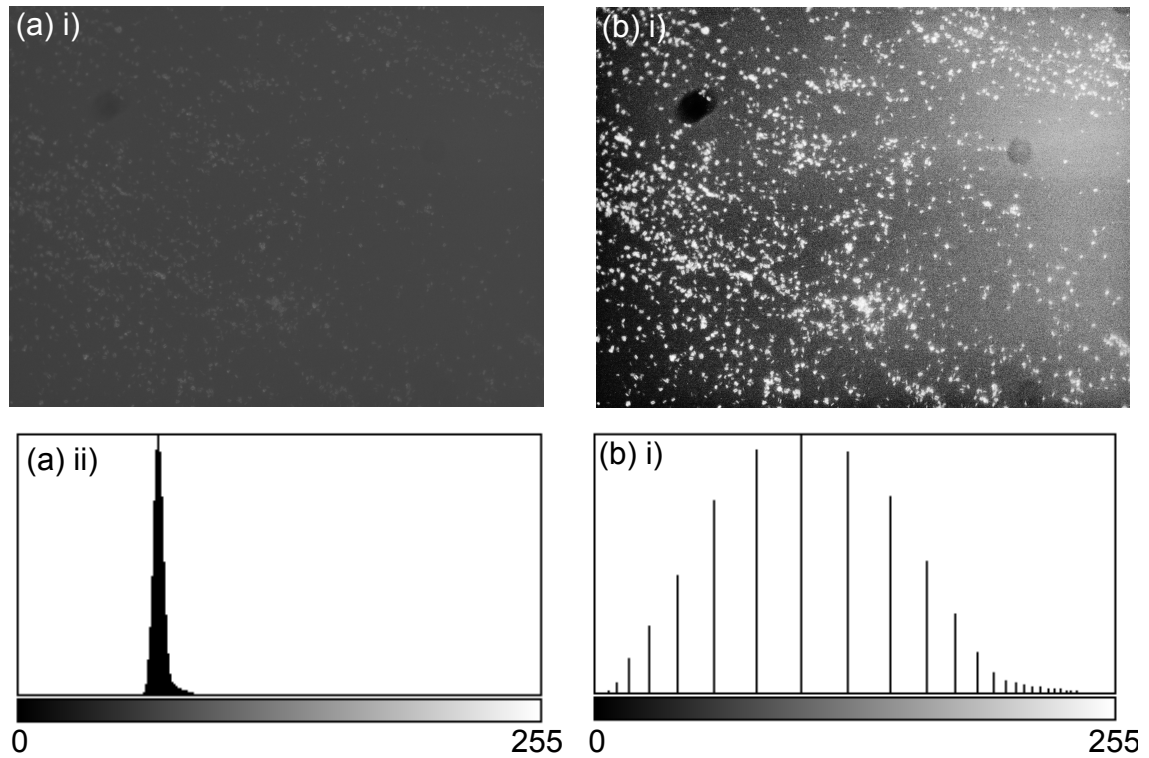
Figure 2.9: Grey-scale images (i) and histograms (ii) for images with (b) and without (a) contrast enhancement.

subtraction looks patchy, and large areas of the background are seen as particles. These extremes of having a rolling ball radius which is too low and too high are illustrated in Figure 2.8 a and c respectively. It was sometimes necessary to alter this value throughout the sequence if a particularly low or high supersaturation was used.

Next, the contrast was enhanced, with histogram equalisation. This meant that the histogram of the image took full advantage of the whole grey scale spectrum, and had the maximum possible contrast. This is illustrated in Figure 2.9. This ensured that images throughout the sequence were made more consistent, so that further image processing could be applied to each image, and the particle count produced
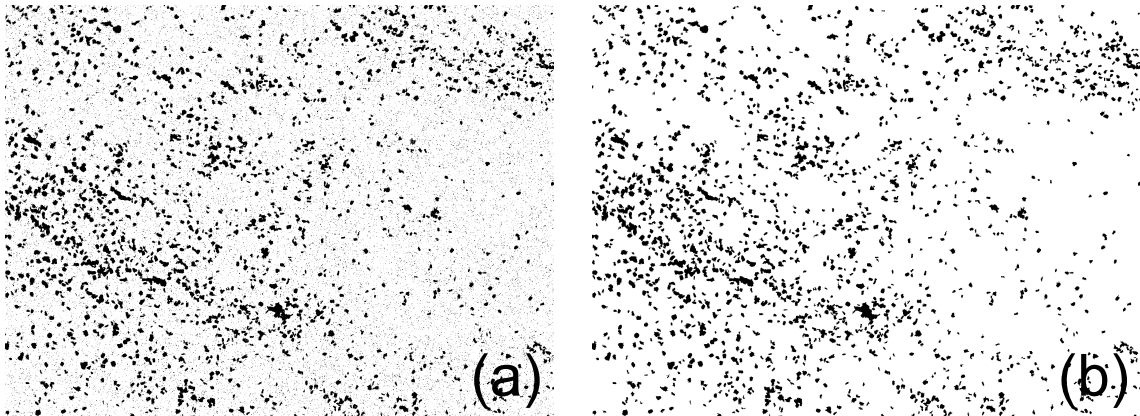
Figure 2.10: Binary images showing (a) an image of surface nucleation of barite which has been converted to binary and (b) the same image which has had a particle analysis performed which excludes noise and includes holes.

was unaffected by the original brightness of the image (which often fluctuated due to alterations made to the microscope mid-experiment, and by nucleation material in bulk solution aggregating and obscuring light as it flowed through the cell).

The image was converted to a binary image with a given lower threshold, which was dependent on the size of particles in the image (upper threshold was always set to a maximum of 255). In order to set an appropriate lower threshold throughout the sequence, a cross section of images in the sequence were tested for a suitable lower threshold, and a rough relationship between image number and lower threshold was calculated and applied to the for loop of the Macro.

When the binary image was produced, the particle analysis was performed, this involved removing very small particles (area ≤ 40 square pixels) and filling particles which contained holes. This is illustrated in Figure 2.10. The parameters that can be calculated as a result of this are inexhaustible, but typically, the area coverage, number of particles and average particle size was printed into a table for further

analysis.

CHAPTER 3

PLANE-RESOLVED KINETICS OF SALICYLIC ACID CRYSTALS

3.1   Abstract

The growth and dissolution kinetics of salicylic acid crystals are investigated *in situ* by focusing on individual micro-scale crystals. From a combination of optical microscopy and FEM modelling, it was possible to obtain a detailed quantitative picture of dissolution and growth dynamics for individual crystal faces. The approach uses real-time *in situ* growth and dissolution data (crystal size and shape as a function of time) to parameterise a FEM model incorporating surface kinetics and bulk to surface diffusion, from which concentration distributions and fluxes are obtained directly. It was found that the (001) face showed strong mass transport

(diffusion) controlled behaviour with an average surface concentration close to the solubility value during growth and dissolution over a wide range of bulk saturation levels. The ($\bar{1}10$) and (110) faces exhibited mixed mass transport/surface controlled behaviour, but with a strong diffusive component. As crystals became relatively large, they tended to exhibit peculiar hollow structures in the end (001) face, observed by interferometry and optical microscopy. Such features have been reported in a number of crystals but there has not been a satisfactory explanation for their origin. The mass transport simulations indicate that there is a large difference in flux across the crystal surface, with high values at the edge of the (001) face compared to the centre, and this flux has to be redistributed across the (001) surface. As the crystal grows, the redistribution process evidently can not be maintained so that the edges grow at the expense of the centre, ultimately creating high index internal structures. At later times, we postulate that these high energy faces - starved of material from solution - dissolve and the extra flux of salicylic acid causes the voids to close.

3.2   Introduction

The study herein concerns salicylic acid (2-hydroxybenzoic acid or *o*-hydroxybenzoic acid), which has been used throughout history as a painkiller and anti-inflammatory, as described in Section 1.3.1. In modern medicine it is much more commonly seen in its esterified form, aspirin, although salicylic acid itself is used to treat various

skin ailments. Despite these important uses, the crystallisation and dissolution kinetics of salicylic acid have not been investigated extensively. The investigations we report herein are aimed at providing considerable new information on the growth and dissolution of individual crystals of salicylic acid at a level where the behaviour of each exposed crystal face can be determined. Furthermore, the methodology described should be of widespread utility and general interest.

A range of imaging methods have been proposed to address crystal growth and dissolution at the level of an individual crystal face [168]. Phase shift interferometry (PSI) [169, 170], AFM [171, 74, 172] and confocal microscopy [173] have all been used to investigate the kinetics of crystal growth [174]. However, for salicylic acid, only dissolution kinetics have been investigated using *in situ* AFM [99, 101, 100]. In water, the (110) and ($\bar{1}$10) faces were studied [99] and dissolution rates determined. These findings are compared to the results later on in Section 3.5.2.

The most common type of investigation of crystal growth and dissolution involves batch stirring systems where bulk rates are measured over time [175, 96, 95]. While such systems provide some insights into crystal growth kinetics, data are averaged over a range of different crystal sizes, and exposed crystal faces, as was described in more detail in Section 1. Furthermore, although mass transport correlations are available for such suspensions [176], they are rather crude which makes it difficult to precisely separate mass transport and surface kinetic effects. Salicylic acid crystal growth has been studied and modelled using such approaches [96, 95, 97, 98].

Blandin *et al.* [96] proposed that the growth of salicylic acid crystals is diffusion controlled at low supersaturations, as did Nallet *et al.* [95].

Quantitative methods which examine micro-crystals are valuable because of the many and varied applications of crystals on this scale, as highlighted in Section 1.4.2. Furthermore, as we show herein, micro-crystals are easier to fully characterise (i.e. to determine the reactivity of individual exposed crystal planes). Moreover, if isolated, micro-crystals are subject to a well-defined mass transport (diffusion) regime, as exemplified by electrochemical studies of UMEs [177]. Put simply, just as reducing the size of a voltammetric/amperometric UME enhances the diffusion rate (magnitude proportional to the inverse of the characteristic electrode dimension), so does shrinking the size of an isolated crystal. Thus, as shown in this chapter, one can promote well-defined (and high) diffusion rates by studying micro-scale crystals. This enhances the opportunity to observe the influence of surface kinetics in heterogeneous physicochemical processes. Herein, we visualise the growth and dissolution of micro-crystals *in situ* and use the experimental data obtained as parameters for a FEM model that then reveals the kinetic regime. The importance of diffusion compared to surface reactions in determining the reactivity is revealed, and the approach allows concentration distributions around growing and dissolving crystals to be predicted.

A further consideration in the growth and dissolution of salicylic acid is polymorphism [178, 179, 180]. Nordström *et al.* [181] have shown that for salicylic acid

crystals formed from aqueous solution, there is only one polymorph, but that the crystals often produced 'peculiar, hollow tubes with square cross sectional areas' as well as simple needle structures. Blandin *et al.* [96] describe the crystals as 'prismatic needle or rod shaped'. Xu *et al.* [182] have described four different morphologies of salicylic acid crystallites when prepared in the presence of four different modifiers.

There is a fairly limited body of work on hollow crystals [183, 184] and the mechanism of their formation has not clearly been established, although it has been postulated that the presence of hollow features is due to dislocations [185]. In the present study, hollow features in salicylic acid crystals were sometimes observed, and the mass transport simulations that are an integral part of these studies provide key insights into the conditions under which hollow features appear. Trapped bubbles which result may be a concern for producing crystalline drug forms, and studies such as those described herein could be used to set conditions under which these undesirable features could be avoided.

3.3 Experimental

3.3.1 Solutions and Samples

All solutions were prepared using ultrapure water (Milli-Q Reagent, Millipore) with a typical resistivity of 18.2 MΩ cm at 25 °C.

Seed micro-crystals were produced on 47 mm diameter circular glass microscope slides (Thermo Scientific) assembled into petri dishes (Willco Wells), using the method described in Section 2.4. The surface of the slides was functionalised with a thin film of PLL which provided a surface for the nucleation of well-defined micro-crystals.

Micro-crystals were produced using 3 ml each of 37.5 mM sodium salicylate (Sigma, > 99.5%) and 90 mM sulphuric acid (Sigma, > 95%) pipetted into the PLL-functionalised petri dishes, mixed and left stationary for 45 minutes in order to nucleate micro-crystals on the surface. The petri dish containing the micro-crystals was rinsed with water and dried using nitrogen.

This method successfully produced a surface with crystals with a typical largest dimension of 40-80 µm. The crystals produced were usually orientated with the (110) plane perpendicular to the glass surface, as shown in Figure 3.1. The salicylic acid crystals had a tabular morphology, as shown. The unit cell, as described by Cochran [93], and further refined by Sundaralingam *et al.* [94] is monoclinic, but
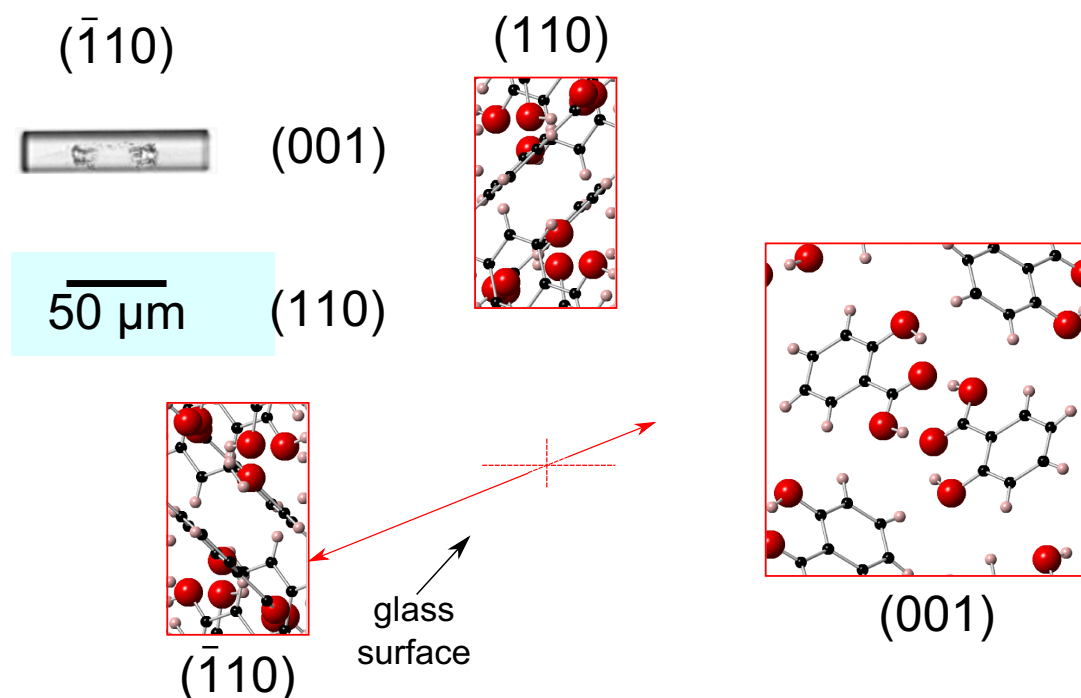
Figure 3.1: Morphology of the salicylic acid crystals. A 3D representation of the morphology with the defining exposed crystal planes labelled, and a bright field microscopy image (top left) of a typical salicylic acid crystal, with the corresponding planes shown.

almost tabular.

3.3.2   Crystal Growth Investigations

3 ml of sodium salicylate (of a defined concentration in the range 14-30 mM) and 3 ml of 60 mM sulphuric acid were pipetted and mixed in a petri dish containing the micro-crystals. A $40\times$ dipping lens on a Leica DM4000 M compound microscope was lowered into the solution and a suitably isolated micro-crystal was located such that the nearest crystal on the surface of the slide was at a distance of at least $30\times$ the largest dimension of the crystal. The lateral resolution was ca. 0.5 µm. This ensured that the micro-crystal investigated was essentially diffusionally isolated for

t = 0

t = 1 hr

(a)

50 μm

t = 0

t = 2 hr

(b)

50 μm
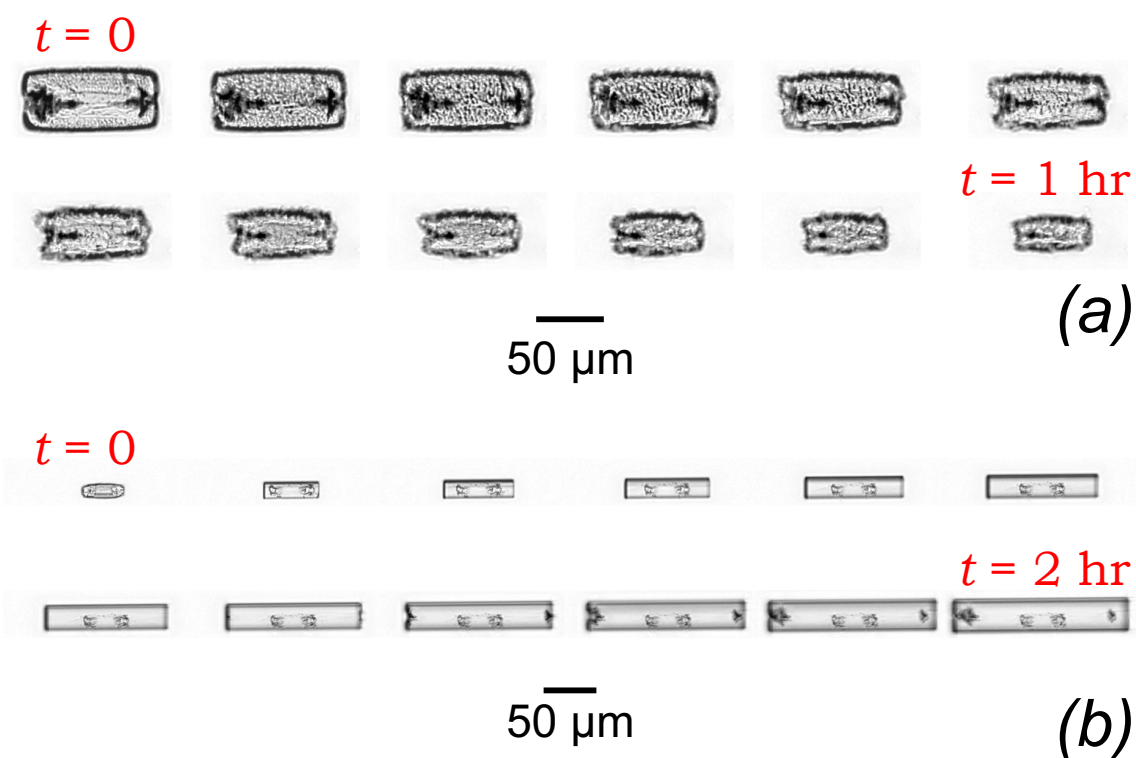
Figure 3.2: Time sequences for crystals during (a) dissolution over a period of 1 hour and (b) growth over a period of 2 hours, taken using optical microscopy. Dissolution is shown in a solution of 8.4 mM salicylic acid and growth is shown for the case of 13.0 mM salicylic acid.

the purpose of crystal growth rate analysis.

A time sequence of images was taken for a particular crystal, typically every 30 s for a duration of one to two hours. Examples of time sequences for dissolution and growth are shown in Figure 3.2, which highlight how the crystal dimensions change over time. From the time lapse sequence, the expansion or contraction of the (001) and ($\bar{1}$10) faces of the crystal (see Figure 3.1) were measured directly with the aid of ImageJ (Version 1.45, NIH).

3.4 Simulations and Modelling

Salicylic acid solution in the presence of the solid (crystal) phase is characterised mainly by the following equilibria:

$$\text{Sal}^-_{\text{(aq)}} + \text{H}^+_{\text{(aq)}} \underset{k_b}{\overset{k_f}{\rightleftharpoons}} \text{HSal}_{\text{(aq)}} \tag{3.1}$$

$$\text{HSal}_{\text{(aq)}} \rightleftharpoons \text{HSal}_{\text{(s)}} \tag{3.2}$$
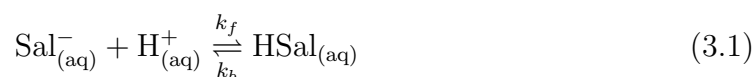
where Sal^- represents the salicylate ion and HSal is salicylic acid.

Speciation in the solution was calculated using MINEQL$^+$ (Environmental Research Software, version 4.6), which also allowed the ionic strength and pH of the solution
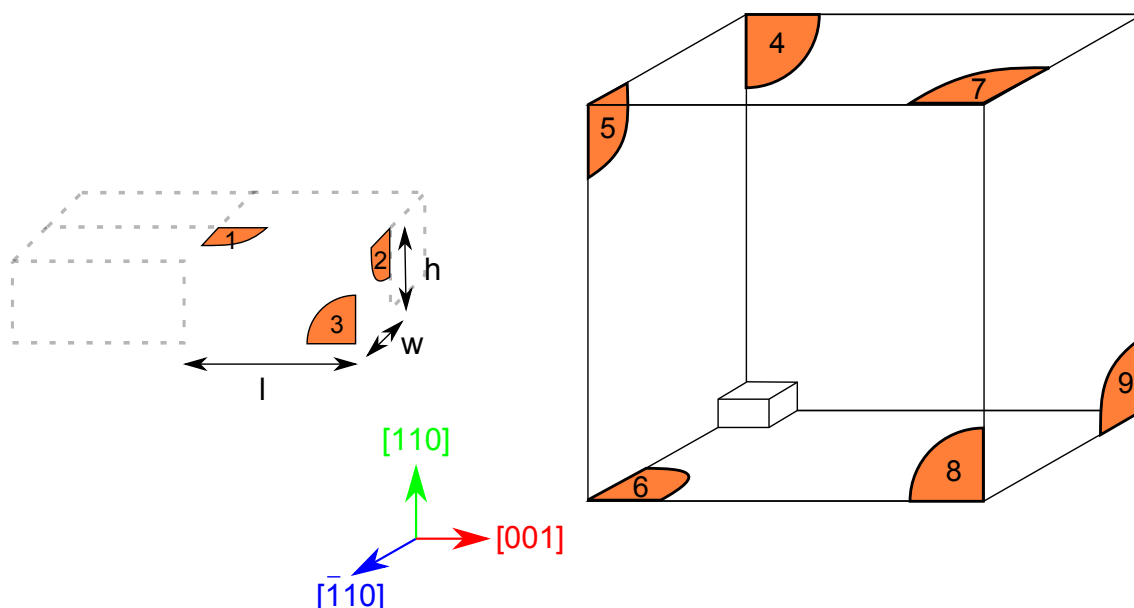
Figure 3.3: Model showing one quarter of the crystal (left), making use of two planes of symmetry to increase computational efficiency. The bulk solution consists of a cube with a dimension of $30l$, and the crystal dimensions are as follows; l is half of the crystal size along the [001] direction (the length), w is half of the crystal size along the $[\bar{1}10]$ direction (the width), and h is the crystal size in the [110] direction (the height). The boundary conditions applied to the labelled faces are detailed in the text.

to be calculated. The temperature was set to the experimental value of 22 °C. The

pK_a of salicylic acid was taken from literature as 2.98 [186].

Finite element modelling was performed using Comsol Multiphysics 4.2a (Comsol

AB, Sweden) using a Dell Intel core 7i Quad 2.93 GHz computer equipped with

16 GB of RAM running Windows 7 Professional ×64 bit. The basic geometry for

the model is shown in Figure 3.3. Simulations were carried out with $> 12,000$

tetrahedral mesh elements. The mesh resolution was defined to be finest near the

surface of the crystal (close to boundaries 1, 2 and 3). Simulations of varying mesh

density were performed to ensure that a fine enough mesh was used for the model

calculations reported herein. Boundaries 4 and 5 are planes of symmetry, as defined

earlier.

The three inter-dependent species Sal^-, H^+ and HSal (Equation 3.1) were considered in the model. For the experimental length scale, mass transport is predominantly controlled by diffusion, for which the following equation was solved:

$$D_j \nabla^2 c_j + R_j = 0 \tag{3.3}$$

where D_j is the diffusion coefficient, c_j is the concentration and j is the species of interest. R_j is a kinetic term representing the the loss and/or formation of species j according to Equation 3.1 which is always at equilibrium. The diffusion coefficients of the individual species can be considered to be constant over the spatial domain investigated: $D_{Sal^-} = D_{HSal} = 8.4 \times 10^{-10}$ m^2 s^{-1} [187] and $D_{H^+} = 7.6 \times 10^{-9}$ m^2 s^{-1} [188].

The boundary conditions applied to the model can be understood with reference to Figure 3.3. Boundaries labelled 1, 2 and 3, representing the growing or dissolving crystal faces, had experimentally determined fluxes of salicylic acid imposed. Thus, the equations satisfied on these boundaries are as follows:

$$\text{boundary 1: } \mathbf{n}.(D_{HSal} \nabla c_{HSal}) = -J_{(001)} \tag{3.4}$$

$$\text{boundary 2: } \mathbf{n}.(D_{\text{HSal}}\nabla c_{\text{HSal}}) = -J_{(\bar{1}10)} \tag{3.5}$$

$$\text{boundary 3: } \mathbf{n}.(D_{\text{HSal}}\nabla c_{\text{HSal}}) = -J_{(110)} \tag{3.6}$$

where $J_{(001)}$, $J_{(\bar{1}10)}$ and $J_{(110)}$ define the flux of HSal incorporated into the (001), ($\bar{1}$10) and (110) face, respectively, and $\mathbf{n}$ is the inward unit vector normal to the boundary. Note that we only needed to consider HSal and not the individual ions at the boundary itself because a rapid equilibrium between H^+, Sal^- and HSal is reasonably assumed (on the time scale of the diffusion process). For computational efficiency we made use of symmetry planes denoted by boundaries 4 and 5, which have no-flux boundary conditions, so that just one quarter of a crystal is simulated. Boundary 6 is constrained by a no-flux condition, to represent the unreactive glass slide on which the crystal grows. Hence:

$$\text{boundary 4-6: } \mathbf{n}.(D_j\nabla c_j) = 0 \tag{3.7}$$

Boundaries 7-9 are set by a bulk concentration condition, because they are a considerable distance away from the crystal to be considered as bulk solution (typically at least 40 times the largest dimension of the crystal in the simulation). We may

reasonably write:

$$\text{boundary 7-9: } c_j = c_{bulk,j} \tag{3.8}$$

where $c_{bulk,j}$ is the bulk concentration of $j = \text{Sal}^-$, HSal and H$^+$. The pH values calculated from MINEQL$^+$, which were consistent with those measured experimentally, were used to calculate $c_{bulk,\text{HSal}}$. The concentration of the protonated and unprotonated salicylate were calculated from the acid dissociation constant K_a (see above; corrected for ionic strength) and the total concentration of the two species HSal$_{tot}$ (known from the dissolved quantity of sodium salicylate).

The reaction rates in Equation 3.3 were calculated based on the equilibrium in Equation 3.1 with the ratio fixed by the acid dissociation constant:

$$K_a = \frac{k_f}{k_b} \tag{3.9}$$

and rate constants sufficiently high to maintain equilibrium at all points in solution.

3.5 Results and discussion

3.5.1 Characterisation of Salicylic Acid Micro-crystals

The orientation of crystals, typically represented by that in Figure 3.1, was determined by powder XRD, as described in Section 2.5.4, to elucidate that the (110) face of the micro-crystal was usually parallel with the glass surface. The other two faces were determined from this result, guided by literature [101, 100], and the known crystal structure [93, 94].

The 2D *in situ* data from optical microscopy, which determined growth/dissolution of the (001) and ($\bar{1}$10) faces, were combined with information from VSI to determine the height, in order to provide 3-D growth rates of crystals, needed for FEM simulations. For this purpose, samples were produced as described previously and then sputtered with a layer of gold of approximately 10 nm. Interferometry images were obtained for a range of crystals with dimensions of 50-250 μm. It was deduced that the height, h, of the crystals was related to the width, w, by $h = 0.76(^{+}_{-}0.3)w$.

3.5.2 Determination of *in situ* Crystal Growth Rates and Interfacial Concentrations

Plots of the displacement of the (001) and ($\bar{1}$10) faces over time were produced from *in situ* optical microscopy for crystal growth and dissolution. Typical example plots
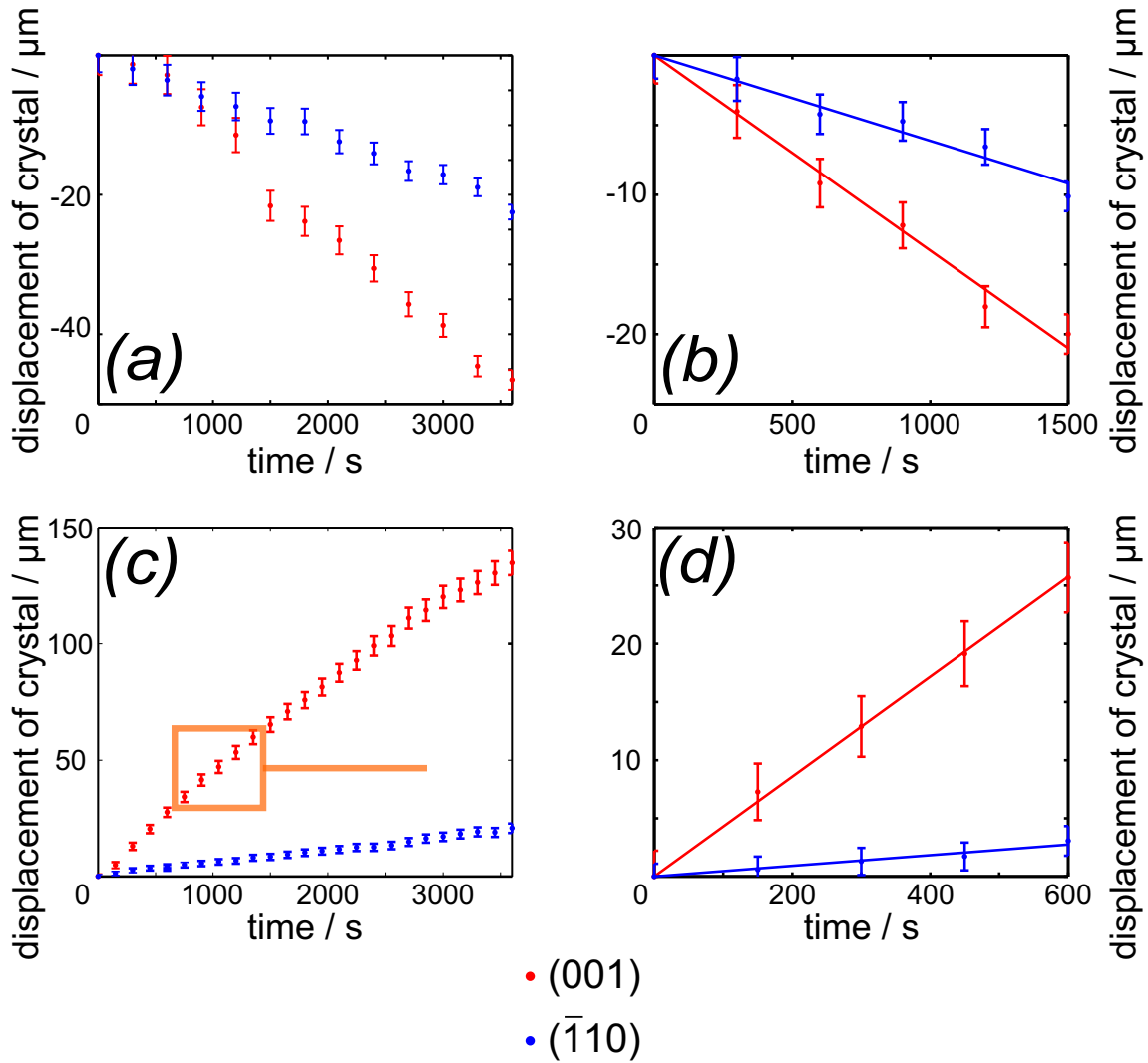
Figure 3.4: Plots showing the change in size of the two crystals in Figure 3.2 over time. Dissolution of a salicylic acid crystal (top) with average dimensions 56.5×23 µmin a solution of sodium salicylate concentration 8.4 mM. Growth of a salicylic acid crystal (bottom) with average dimensions 166.5×32 µm in a solution of salicylic acid concentration 13.0 mM. The plots on the left hand side correspond to the entire dissolution/growth period recorded and the graph on the right hand side corresponds to a short period of time of this experiment, as illustrated. Over a shorter period of time a constant dissolution/growth rate is observed for a particular solution composition.

in Figure 3.4 show the expected features of a shrinking crystal for dissolution and expanding planes for crystal growth. It is evident that the (001) plane is much more active than the ($\bar{1}$10) face for both dissolution and growth. It is also clear from the long time plots (3.4a and c) that although the growth and dissolution rate of the crystal is close to linear with time, the relationship is not strict, especially for the (001) face, where the apparent growth rate evidently decreases at longer times for growth (corresponding to increased crystal size) and increases at longer times for dissolution rate (decreased crystal size). This can be attributed to the influence of mass transport, because diffusion rates alter as the micro-crystal dimension changes with time. In brief, diffusion rates to micro-scale interfaces scale with the inverse of the characteristic dimension This effect does not seem to be as evident in the growth and dissolution behaviour of the ($\bar{1}$10) face.

For quantitative analysis, I focused on growth over relatively short times (as indicated, for example, to the right of Figure 3.4). For shorter periods of time, where the overall crystal dimensions change less, a close to linear relationship between crystal dimensions and time is evident. A static FEM model, relevant to the crystal size for the time period of interest, could be used to analyze mass transport and crystal reactivity, because the characteristic diffusion time of the experimental micro-crystal system was much faster than that for changes in crystal dimensions by growth and dissolution. This resulted in considerable computational efficiency compared to an equivalent time-dependent moving boundary model.

The flux $J_{(xyz)}$ of salicylic acid was determined for each face (xyz) of the crystal from:

$$J_{(xyz)} = v_{(xyz)}\rho_{\text{HSal}} \tag{3.10}$$

where $v_{(xyz)}$ is the experimentally determined growth or dissolution velocity of face (xyz) and ρ_{HSal} is the molar volume of salicylic acid, calculated from the density of salicylic acid (1.443 g cm^3 [94]).

Figure 3.5 shows the relationship between flux into or out of the two characteristic crystal faces as a function of the bulk solution concentration. The saturation ratio of the solution is given by:

$$S = \frac{c_{bulk,\text{HSal}}}{c^*_{bulk,\text{HSal}}} \tag{3.11}$$

where $c^*_{bulk,\text{HSal}}$ is the concentration in bulk when there is neither dissolution or growth. This is determined by the intercept on the y axis in Figure 3.5. When $S \geq 1$ the system is supersaturated, meaning that crystal growth occurs, and when $S < 1$ the crystal will dissolve. In equilibrium, the bulk solution concentration (of fully protonated salicylic acid) at $S = 1$ are as follows for the (001) face and the
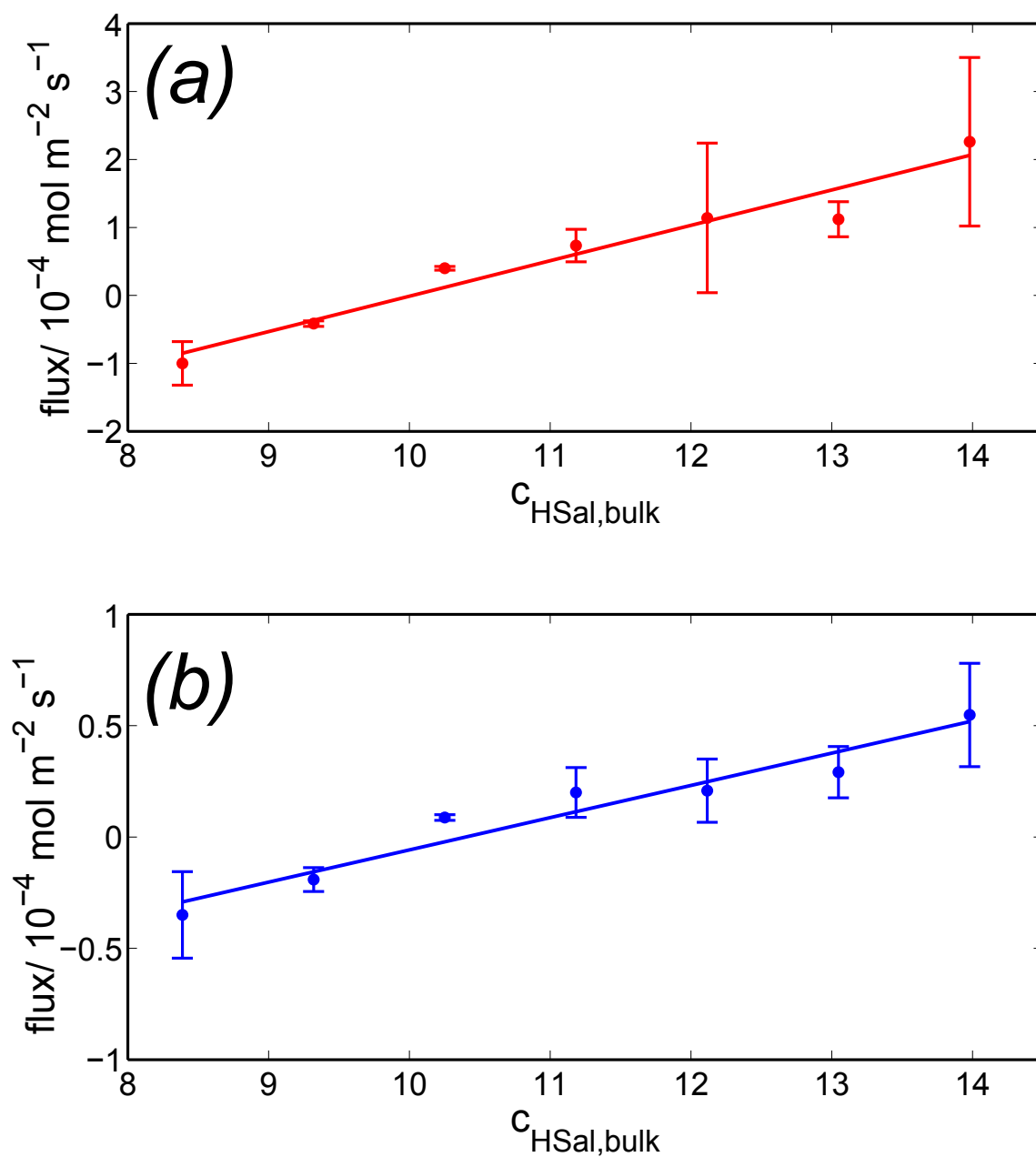
Figure 3.5: Plots showing how the flux per unit area into the crystal faces varies for change in bulk concentration. Data for the (001) face (a) and the ($\bar{1}$10) face (b).

($\bar{1}$10) faces, $c^*_{(001),bulk,\text{HSal}}$ and $c^*_{(\bar{1}10),bulk,\text{HSal}}$, respectively:

$$c^*_{(001),bulk,\text{HSal}} = 10.0^+_-0.5 \text{ mM} \tag{3.12}$$

$$c^*_{(\bar{1}10),bulk,\text{HSal}} = 10.3^+_-0.6 \text{ mM} \tag{3.13}$$

I notice that these values are similar, but slightly lower than the solubility of salicylic acid previously reported in literature. Nordström *et al.* [181] found that the solubility of salicylic acid was 11.6 mM at 20°C in water. Compton *et al.* [101] report a solubility of 14.9 mM for total salicylic acid and salicylate, which is equal to a value of 11.2 mM for just the salicylic acid species.

It is important to comment on the noticeable range in measured flux at each bulk concentration in Figure 3.5. This is largely due to the range of crystal sizes studied and the fact that the crystals grow and dissolve with a significant contribution of diffusion, which then has a major influence on the flux. Thus, while the composite plot in Figure 3.5 identifies general trends, the growth and dissolution behaviour of individual crystals was examined to extract kinetics using FEM simulations to mimic the precise crystal dimensions.

Typical example outputs of the FEM simulations for dissolution and growth are shown in Figure 3.6. For the case of growth the bulk concentration was 11.2 mM
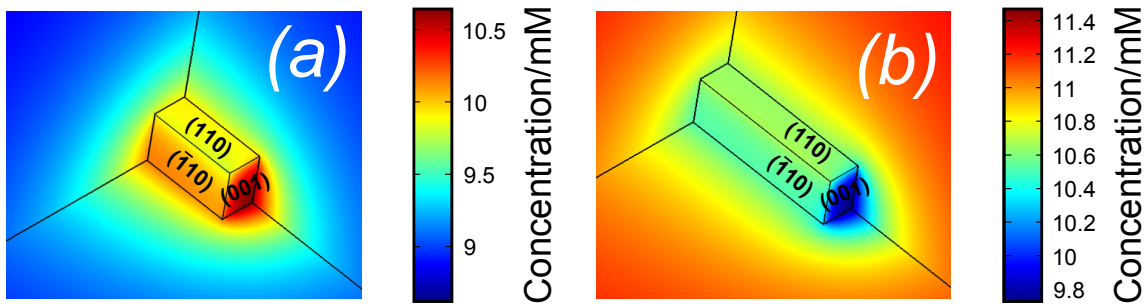
Figure 3.6: Examples of results of FEM simulations for dissolution in a bulk solution of 8.4 mM HSal with a crystal of largest dimension 39 µm (a) and growth in a bulk solution of 11.2 mM with a crystal of largest dimension 67 µm (b).

and for dissolution it was 8.4 mM and the crystal dimensions are indicated in the caption. During dissolution (Figure 3.6a) the salicylic acid concentration close to the crystal surface is higher than in the bulk solution, and there is evidently a concentration boundary layer (or diffusion layer) from the crystal to the bulk. This is particularly pronounced for the (001) face.

For the case of growth (Figure 3.6b), the simulations show broadly similar trends for the concentration on the faces, but with the crystal acting as a sink for salicylic acid. The concentration is now lower on the faster growing (001) face. Again, on the other faces, the concentration profile from the crystal to the bulk is less pronounced.

Figure 3.7 shows the concentration profiles perpendicular to the centre of the three crystal faces, for the cases of dissolution and growth shown in figure 3.6. This clearly shows that the crystal faces act as sinks and sources of salicylic acid to different degrees. Close to the crystal the gradient is steeper for the (001) surface (for dissolution and growth), as expected based on the optical microscopy data. The difference between the surface concentrations of salicylic acid on the (110) and ($\bar{1}$10)
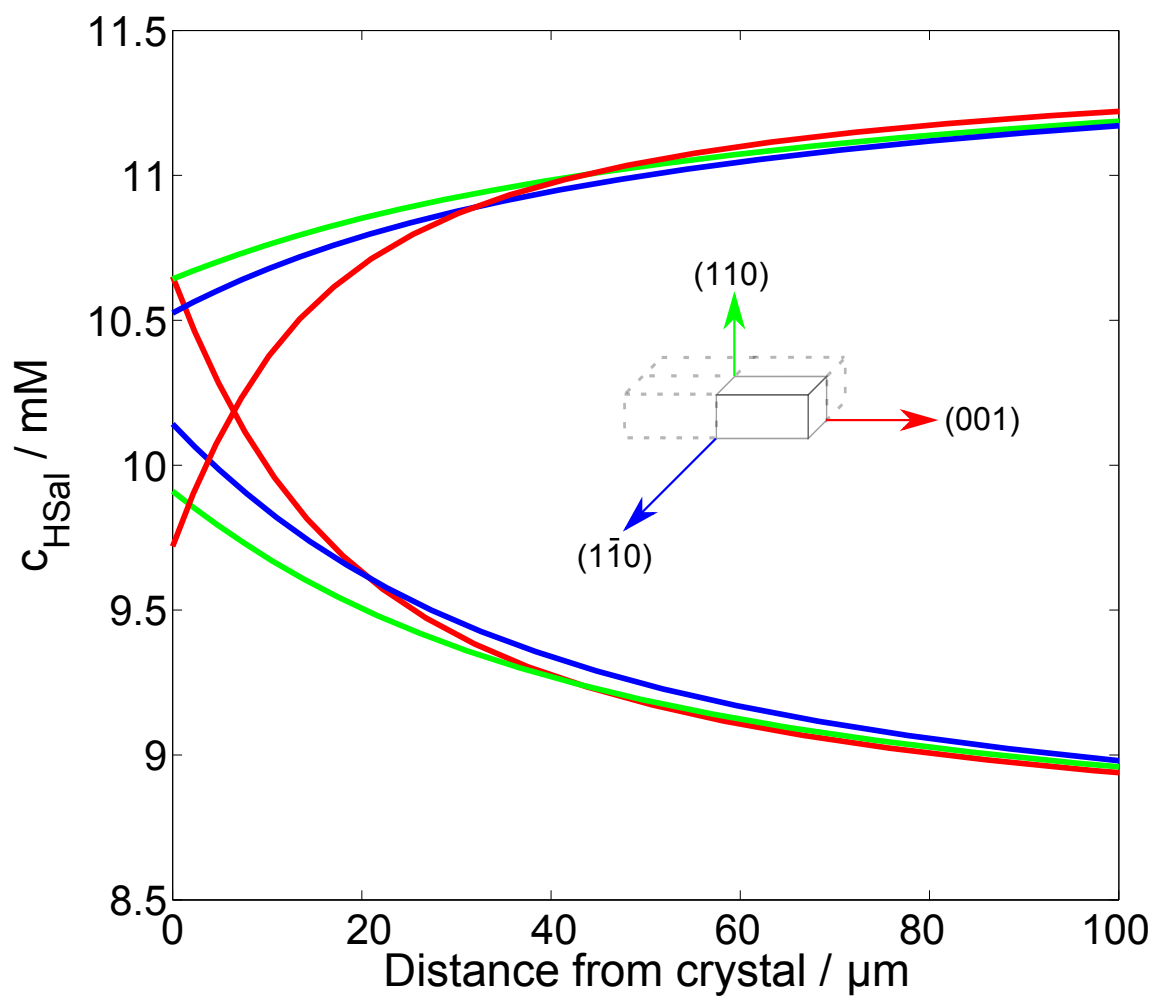
Figure 3.7: Plots showing the variation of concentration from the centre of each face, moving perpendicularly to the bulk solution, for the case of dissolution and growth (same crystals as shown in Figure 3.6)

faces for dissolution and growth indicates that although there is a significant mass transport component during dissolution and growth of these faces, there is some surface kinetic control. For the (001) face the surface concentrations are closer to those for a purely transport-controlled system. In fact, these surface concentrations cross over so that the value for growth is lower than for dissolution. This is not expected to be a real effect, but rather associated with the difficulty of precisely determining crystal dimensions and particularly measuring the morphology of dissolving crystals due to pitting. The fuzzy crystal outlines (see Figure 3.2a, for example) introduced a small systematic error defining the crystal surface, which tended to cause a slight underestimation of the crystal dimensions.

For the (001) face in the growth regime ($c_{bulk,\text{HSal}} > 10$ mM), the concentration does not change appreciably with bulk concentration, and attains values close to the saturated value. This indicates clearly that growth of this face is dominated by diffusion. In contrast, the ($\bar{1}10$) and (110) faces both show a small, systematic increase in the surface concentration with increased bulk concentration. However, concentration values are much lower than the bulk concentration, indicative of small, but detectable, contribution of surface kinetics to the overall rate, consistent with the arguments presented above. In the dissolution regime, all faces appear to show a small amount of surface kinetic control, but there is still a strong diffusion component. It was noiced that there is a perhaps a slight overestimate of the dissolution rate, reflected in higher surface concentrations, due to pitting of the crystal during dissolution, which makes it difficult to define the crystal size, as discussed above in

relation to Figure 3.2a. However, this does not prevent me from semi-quantitatively identifying the main trend.

As highlighted earlier, there has been little investigation into the growth and dissolution of salicylic acid, but it is informative to compare the results to prior work, where quantitative comparisons can be made. Compton *et al.* [101, 99] investigated the dissolution kinetics of large, exposed (110) and ($\bar{1}$10) faces of salicylic acid (typically $3 \times 3 \times 30$ mm), using a hydrodynamic AFM flow cell to measure the dissolution rate. For the ($\bar{1}$10) face with bulk concentrations of total dissolved salicylic acid of 0 mM, 3 mM and 10 mM they concluded that the dissolution process was surface-controlled with a surface flux of the order 10^{-5} mol cm^{-2} s^{-1} [99], while it was observed for the same faces a dominant mass transport component with comparable or higher fluxes for similar saturation levels. They measured the overall retreat of the surfaces as small changes in the mean height; such measurements are extremely sensitive to drift of the piezoelectric controller [189], and requires very careful surface control if the accuracy of AFM dissolution studies is to be compromised [190]. Moreover, in Figure 10 [101], the data for 7 mM and water could arguably just as easily be linearly fitted to the mass transport rate. It is also noted that a significant dissolution rate was reported for a saturated solution in these studies, whereas no net dissolution would be expected. As highlighted earlier, there has been little investigation into the growth and dissolution of salicylic acid, but it is informative to compare the results to prior work, where quantitative comparisons can be made. Compton *et al.* [101, 99] investigated the dissolution kinetics of large,

exposed (110) and ($\bar{1}$10) faces of salicylic acid (typically 3 × 3 × 30 mm), using a hydrodynamic AFM flow cell to measure the dissolution rate. For the ($\bar{1}$10) face with bulk concentrations of total dissolved salicylic acid of 0 mM, 3 mM and 10 mM they concluded that the dissolution process was surface-controlled with a surface flux of the order 10^{-5} mol cm^{-2} s^{-1} [99], while it was observed for the same faces a dominant mass transport component with comparable or higher fluxes for similar saturation levels. They measured the overall retreat of the surfaces as small changes in the mean height; such measurements are extremely sensitive to drift of the piezo-electric controller [189], and requires very careful surface control if the accuracy of AFM dissolution studies is to be compromised [190]. Moreover, in Figure 10 [101], the data for 7 mM and water could arguably just as easily be linearly fitted to the mass transport rate. Also noted is that a significant dissolution rate was reported for a saturated solution in these studies, whereas no net dissolution would be expected.

3.5.3 Hollow Features in Crystals

When larger dimensions (50-100 µm width) were achieved, the crystals were often found to exhibit hollow features in the (001) face. Example bright field microscopy images of such crystals are illustrated in Figure 3.8a. Confirmation of holes in the crystal was achieved by VSI measurements, such as the data shown in Figure 3.8b and c. It is evident that the hollow features extend in these cases about 100 µm into the body of the crystals.

100 μm   50 μm

(a)

(b)

(c)
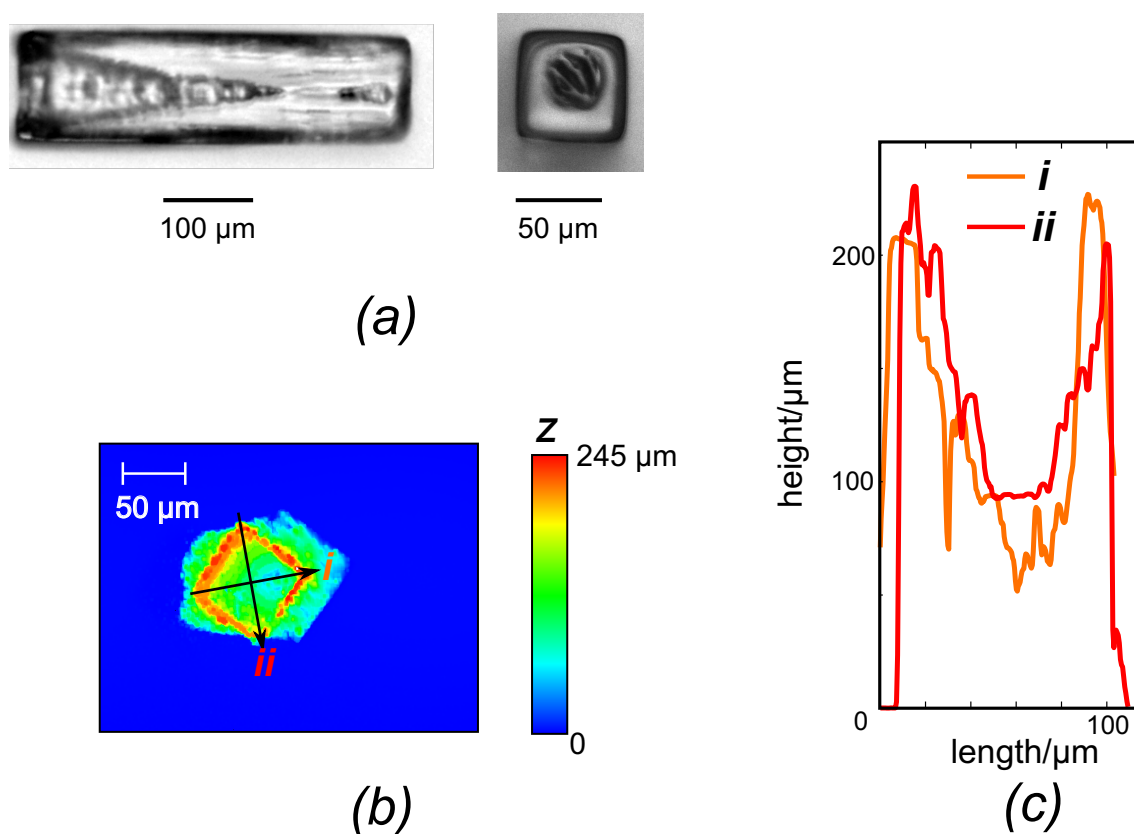
Figure 3.8: (a) Differential interference contrast optical microscope images of typical large salicylic acid crystals, showing hollow features in the (001) face, viewed from the side (left), and the top (right). (b) VSI image showing a hollow feature in a crystal oriented so that the (001) face was parallel with the glass surface with two cross sections of the crystal (i and ii), shown in more detail as cross-sections (c).
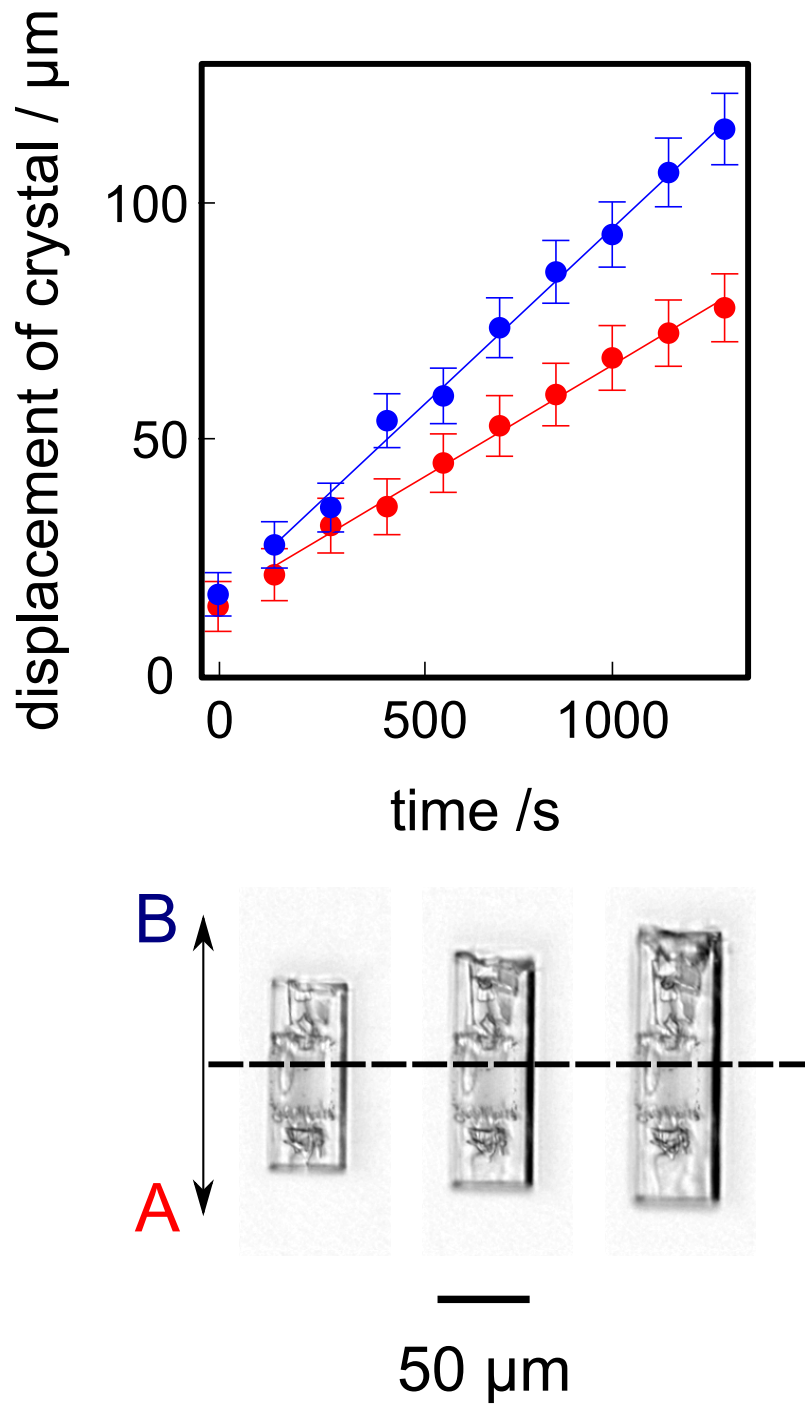
Figure 3.9: Plot showing the change in size of the crystal in both the A and B planes (top), from a particular reference plane illustrated by the horizontal dashed line across the time sequence images (bottom). It is observed from the time sequence images that a reasonable part of the growth in the B direction involves the existence of a hollow feature, and there is an increased growth rate compared to the other side of the crystal (A).

I can explain and rationalise the formation of these hollow features in terms of mass transport control which dominates the large micro-crystals (*vide supra*). Figure 3.9 compares the growth of the two (001) end planes of salicylic acid micro-crystals, labelled A and B (below the plot), with respect to a common reference plane shown by the dashed line across the centre of the crystal images. In the B direction, considerable hollow features are observed in the crystal during the time period shown, whereas in the A direction, the (001) face is flat and does not appear to show any of these characteristic holes. For this time period there is a noticeable difference between the growth rates observed in the A and B directions. The crystal grows more quickly in the B direction with an average growth rate of $0.075(^{+}_{-}0.006)$ µm s^{-1} compared to $0.047(^{+}_{-}0.006)$ µm s^{-1} in the A direction. This is because the active area at the end of the B face is smaller and so receives a high diffusive flux of material.

It is seen from simulations (e.g. Figure 3.6b) that during growth on the (001) face, the flux is higher at the edge of the face (steeper concentration gradient) than in the centre of the face. In contrast, growth of the (110) and ($\bar{1}$10) faces is under mixed diffusion/surface kinetic control. This picture of mass transport is shown schematically in Figure 3.10a. Because the (001) face is flat, but grows at a diffusion limited rate, the near interface concentration of salicylic acid has to be at the saturated level and to maintain a uniform growth rate of the surface, material has to be redistributed across the face (e.g. by surface diffusion). The larger the crystal, the greater the distance which the material has to diffuse from the edge to the centre, and it is evident that a point is reached where this cannot be sustained
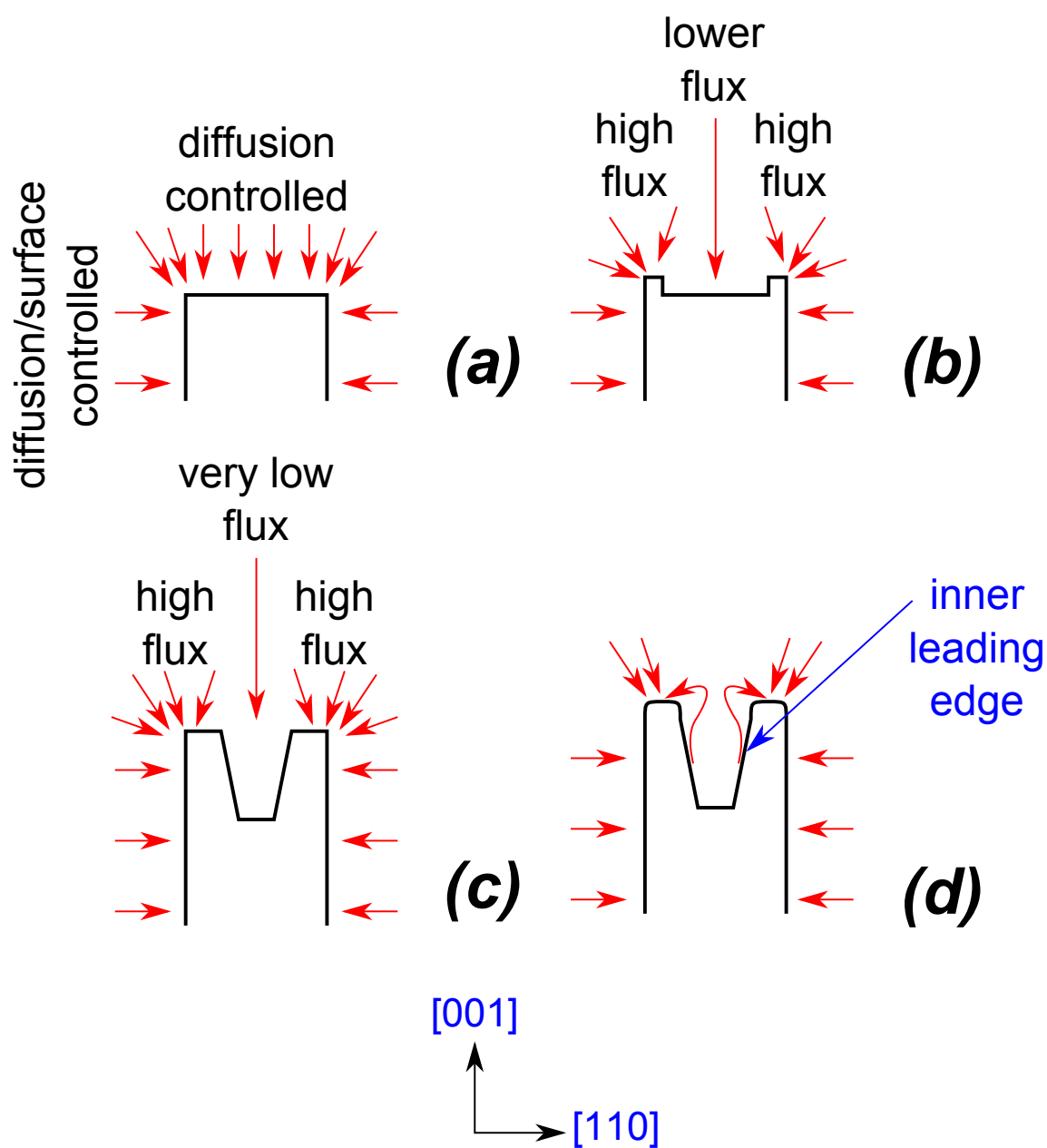
Figure 3.10: Illustration of the formation (a and b), growth (c) and closure (d) of hollow features on the (001) face of a salicylic acid crystal. The general flux of material is shown by the red arrows.

so that HSal is incorporated at the edges faster than at the centre. At this stage (Figure 3.10b) the edges of the (001) face start to grow preferentially, depleting material and slowing growth at the centre. Moreover, the availability of HSal in solution at the edges compared to the centre causes the edge to overgrow (Figure 3.10c). This process continues for a significant time, but an interesting aspect is that the hollows eventually close over. It is postulated that the inner leading edge created inside the hollow feature (Figure 3.10d) would be expected to be of higher energy (higher solubility) and as this region is recessed it is starved of growth material. Thus, the leading edge could start to dissolve, with diffusion from the inner leading edge toward the edges, therefore closing the hollow. Interestingly, and supporting this hypothesis, the higher mass transport on the edges of the (001) face leads to a slightly convex morphology during dissolution (Figure 3.2a).

In previous literature, hollow features have been observed when crystals are produced by vapour deposition [183], but little work on hollow crystals in solution has been carried to date. There has been some attempt at explaining the emergence of this phenomenon. It has been suggested that the origin of a hollow feature is a dislocation in the crystal structure [185], with a spiral dislocation being responsible for a pyramidal hollow like those observed in the present study for salicylic acid crystals [64]. The that data from FEM simulations show that the characteristic patterns of diffusive mass transport also appear to play a role in the emergence, growth and closure of hollow features.

3.6 Conclusions

This study has shown that time lapse optical microscopy combined with FEM modelling is an effective approach for probing micro-crystal growth and dissolution kinetics. In particular, using data from optical microscopy to parameterise a FEM model of a growing/dissolving crystal reveals direct information about concentration distribution around a crystal and the interfacial concentrations. This, in turn, allows the importance of diffusion compared to surface kinetics to be elucidated for each crystal face. For salicylic acid, the (001) face has been shown to be dominated by mass transport for both dissolution and growth, whereas the (110) and ($\bar{1}$10) faces show more surface kinetic control, although diffusion remains a significant component of the overall kinetics.

Knowledge of the importance of mass transport for this system has allowed a convincing explanation for the presence of hollow features seen when the crystals become large. These features are a direct consequence of differential flux across the (001) face with the edges experiencing a much higher diffusive flux than the centre position. Ultimately this leads to preferred growth at the edges compared to the centre, causing the formation of a hollow feature in this face. Interestingly, as time proceeds, these features become enclosed, with a roof structure. This suggests that the internal walls of the hollow feature (high index faces) become shielded from the growth flux that they dissolve so that the feature becomes enclosed. Hollow features have been seen in other micro-crystal systems and differential diffusive fluxes appear

to provide a satisfactory analysis of this phenomenon.

CHAPTER 4

SCANNING ELECTROCHEMICAL MICROSCOPY OF THE DISSOLUTION OF SALICYLIC ACID MICRO-CRYSTALS

4.1 Abstract

The dissolution rate of the (110) face of salicylic acid in aqueous solution is determined by hopping intermittent contact scanning electrochemical microscopy using a platinum 2 µm diameter UME. The method allows for the activity to be proved in a 3D volume adjacent to the solid-liquid interface. A 3D representation of the activity (flux and concentration profiles) close to the interface is observed in detail and individual approach curves are extracted for quantitative dissolution kinetics.

The system is modelled using FEM simulations which predict approach curves onto the crystal for a first order dissolution process. The approach curves produced are compared and the dissolution rate constant is predicted by analysing the current measured at the distance of closest approach, and the change in current slightly further from the surface. It was found that the values obtained show a surface with a large degree of heterogeneity.

4.2 Introduction

Crystalline substances are of wide ranging interest, for example in natural biochemical processes[191, 192, 193, 194], for use in building materials[195, 113] and the food and pharmaceutical industries[40, 196, 102]. This chapter focuses on the dissolution of pharmaceutical crystals for the current study. Organic crystalline materials generally have a higher solubility and large dissolution and growth rates, even at low supersaturations [197, 181], making them difficult to quantitatively study. However, the understanding of these processes is hugely valuable to the pharmaceutical industry for many reasons, as discussed in Section 1.3.1.

For the case of a crystal dissolving in a solution, the surface kinetics control the rate at which growth units detach from the surface, and the dissolution kinetics control the rate at which those species can then diffuse into bulk aqueous solution from the solid-liquid interface [195]. Additionally, dissolution processes are further

complicated by the fact that crystal surfaces are microscopically detailed which may impact the resulting kinetics. The crystal surface is built up of kinks, ledges and terrace surfaces by which the growth unit gradually detaches, firstly by detaching from the active site, followed by surface diffusion across a surface terrace, and finally desorption from the solid-liquid interface, as described by the BCF theory[69, 70, 71].

As discussed previously in Chapter 3, there have been studies which observe salicylic acid crystals by batch stirring systems[175, 96, 198]. It has been concluded that the results from these batch precipitations are difficult to compare with one another, let alone a technique where mass transport is carefully controlled and intrinsic interfacial kinetics are truly observed[96].

For salicylic acid, a hydrodynamic flow cell combined with AFM has been used [99, 100, 101]. As discussed in Section 3.5.2, it was assumed that sufficiently high mass transport rates were employed to produce a kinetic regime, but this was questioned in Chapter 3.5.2. In the previous chapter crystals with micro-scale dimensions were studied using *in situ* optical microscopy, combined with FEM simulations, and monitored dissolution/crystal growth in solution. Although this produced detailed information regarding the kinetic/diffusion behaviour of the crystals, the system was largely under diffusion control, although it was found that the dissolution behaviour was dependant on the plane of the crystal.

As mentioned, hydrodynamic methods of probing interfacial kinetics include the use of a rotating disk electrode (RDE)[199, 126, 125] and channel flow combined with
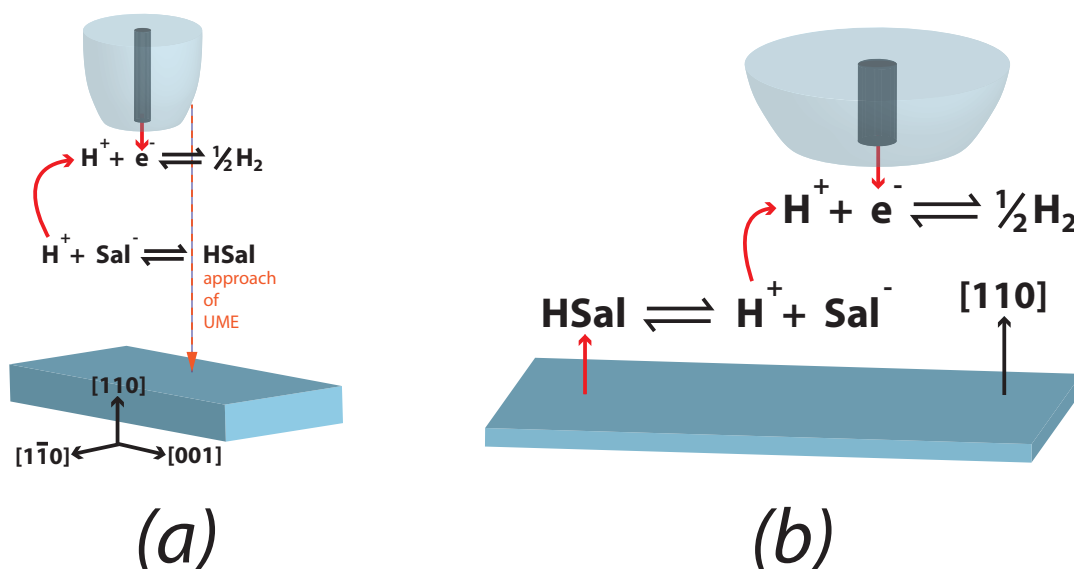
Figure 4.1: A schematic describing the experimental method and reactions occurring for HIC-SECM on the (110) face of salicylic acid. (a) The solution contained salicylic acid (HSal) which underwent equilibrium with protons and the salicylate ion (Sal$^-$), as shown. Protons from this reaction, and acid added to the solution, were oxidised at the surface of a 2 μm diameter platinum UME. The UME was then brought into intermittent contact with the surface of the (110) face of a salicylic acid crystal. The localised low concentration of protons at the UME surface caused the salicylic acid nearby to dissociate, therefore causing an undersaturation of salicylic acid. (b) When the UME was brought into closer contact with the (110) face of the salicylic acid crystal, this localised undersaturation caused the crystal surface to dissolve to replenish aqueous salicylic acid.

electrochemical measurements[127, 128], in both of these cases convection is used to increase the rate of mass transport. However, any hydrodynamic perturbation may not be favourable for the study of crystal growth and dissolution, as the method of measurement of surface kinetics is inferred from this hydrodynamic flow rather than measured directly.

The present study uses SECM[133, 44], where an UME is used to probe surface kinetics. There are several examples of this technique being applied to crystal dissolution in literature[200, 201, 202, 203, 204, 205, 206, 207]. The basic idea is to use

a local probe to change the local solution concentration near the crystal/solution interface, so as to create an undersaturated solution. This leads to dissolution, the flux of which is reflected in the tip current measured. In contrast, in the present study, local salicylic acid concentration is lowered by the reduction of protons at the electrode surface, as illustrated in Figure 4.1a. This causes the weak acid to dissociate, therefore lowering the concentration of salicylic acid and causing an undersaturation. When placed in close proximity of the crystal surface, the UME will therefore drive, and monitor, dissolution over z. This approach evidently expands the range of systems that can be studied, but is also advantageous because the product (H_2) is innocuous in the system in contrast to other earlier systems where the product may accumulate at the electrode or impact dissolution. A schematic of this is also shown in Figure 4.2, when the diffusion field of the UME overlaps with the crystal surface, a flux will be induced from the crystal surface.

In past studies, dissolution has been induced by removal of either the cation or anion at the tip, as the focus has been on ionic crystals [204, 202, 201]. The current study combines the large dataset obtained by HIC-SECM with FEM simulations. FEM simulations are increasingly being used to obtain quantitative information about interfacial chemistry [193, 102]. Herein, it is demonstrated that by comparison of experimental data with FEM, the dissolution rate constant of a crystal surface can be estimated.
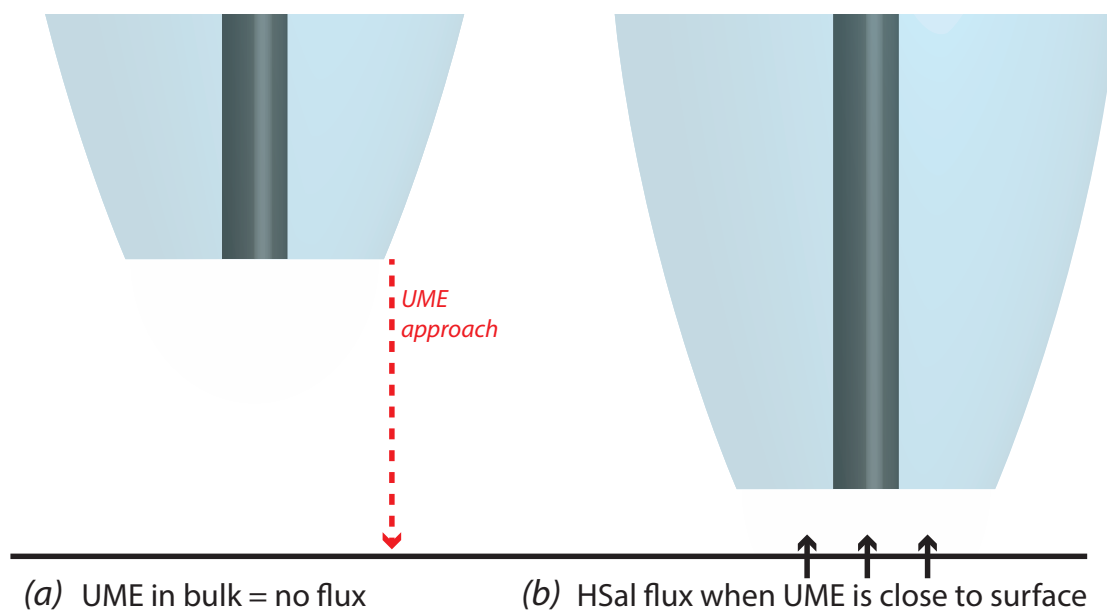
Figure 4.2: Schematic showing (a) the flux of protons at the UME, and (b) the effect this has on the (110) face of the salicylic acid crystal, when approached close to the surface.

4.3 Experimental

4.3.1 Solutions, samples and electrodes

Micro-crystals of salicylic acid were produced on PLL functionalised glass slides assembled into petri dishes as described recently in Perry *et al.*[102].

All solutions were prepared using ultrapure water (Milli-Q Reagent, Millipore) with a typical resistivity of 18.2 MΩ cm at 25 °C, and all chemicals were purchased from Sigma. For HIC-SECM measurements, 250 mM sodium salicylate was combined in equal parts with 10 mM sulphuric acid (Sigma) and stirred to mix thoroughly prior to scanning. These concentrations were chosen as they result in a solution with salicylic acid species concentration of 10 mM, as was determined by MINEQL+

software, which is just saturated [102] and ensures that the crystal will not grow or dissolve considerably during the period of an image of 45 minutes. This solution was filtered into the petri dish.

A two electrode set-up was used with a 2 µm diameter platinum-disk UME serving as the working electrode that was fabricated in house[166]. This approach evidently expands to a range of systems that can be studied, but is also advantageous because the product (H_2) is innocuous in the system, in contrast to other earlier studies, where the product may accumulate at the electrode or impact dissolution. A SCE was used as a reference electrode. The UME was characterised by a ratio of the glass radius to platinum radius, known as the RG value [133], of 15. Prior to scanning, the Pt UME was carefully polished using a moist microfibre pad (Bauer) covered with alumina suspension (0.05 µm particles, Buehler) in purified water. It was then rinsed and polished on a second microfibre pad containing only purified water.

4.3.2 Instrumentation

The hardware used was a modified version of the recently reported set-up for IC-SECM, and described in detail for HIC-SECM.[140] The instrumentation differed in the fine control of x, y and z of the SECM tip, which was realised by a multi-axis nanopositioning system in closed loop operation with a 100 x 100 x 100 µm range (P-61135 NanoCube XYZ Piezo Stage, PI). The stage was mounted on an inverted optical microscope (Zeiss), using a 40× lens, used to visualise and locate suitable
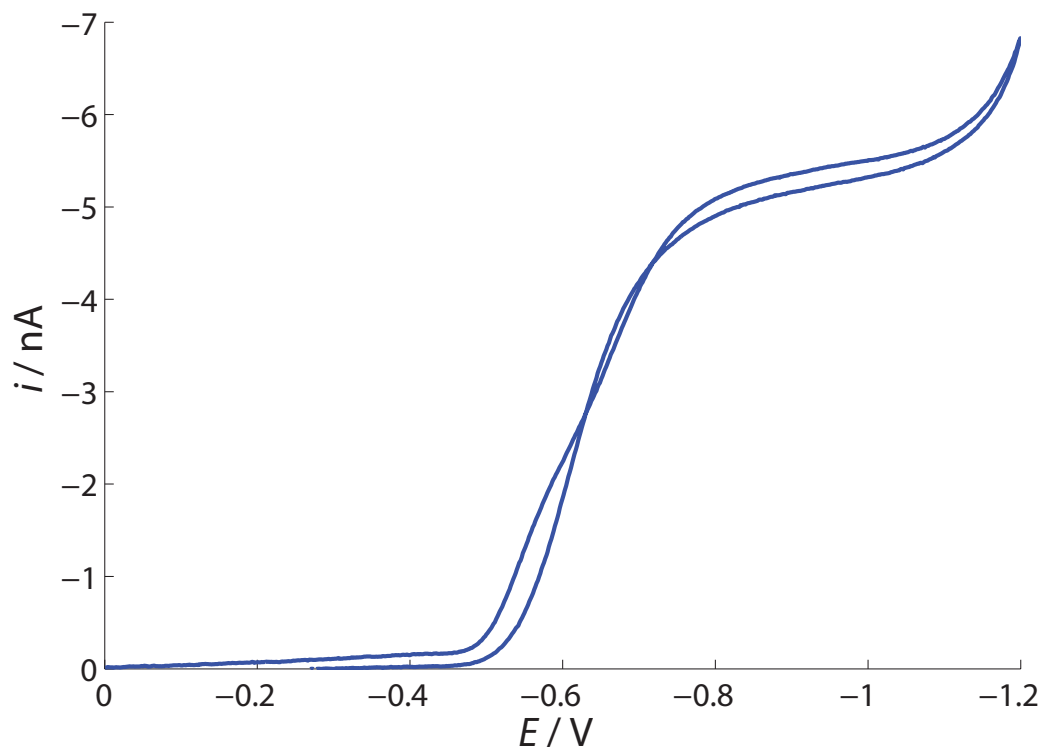
Figure 4.3: Cyclic voltammogram showing the reduction of protons at the surface of a UME. Using a solution mixture of 50% 250 mM sodium salicylate, 50% 10 mM sulphuric acid and a scan rate of 60 mV/s.

crystals for study.

Cyclic voltammetry (CV) was performed in bulk to identify the potential required for the diffusion-limited reduction of H^+ with respect to the reference SCE. Typically this was between -0.8 V and -1.0 V vs. SCE, and was determined by the plateau of the CV, indicating a limiting current[44]. A typical wide CV for proton reduction is shown in Figure 4.3, this plateau is illustrated in this potential range. The further change in current at more negative potentials is due to water reduction.

4.3.3 Imaging

A LabVIEW (National Instruments) program controlled the piezo bender actuator as follows. The tip was oscillated with a frequency of 80 Hz and an amplitude of 50 nm, and the crystal was approached with a step size of 50 nm. When the tip oscillation amplitude fell below 30 nm, indicating that the tip made physical contact with the crystal the tip retracted in z normal to the surface and moved in x-y parallel to the surface to the next point in a raster scan. During each tip approach, the DC working electrode current was measured as a function of z.

A petri dish containing the salicylic acid crystals was placed on the x-y stage of the instrumentation. A suitable crystal, 50-100 µm in its largest dimension, and isolated so that no other crystals were located within a region of at least 40× the largest dimension, was located using the inverted optical microscope. This meant that the crystal selected could be viewed as diffusionally isolated, aiding quantitative analysis of kinetics. The (110) face of the salicylic acid crystals were studied, as this is in the same plane as the glass slide [102]. The tip electrode was attached to the piezo bender actuator and positioned above an appropriate salicylic acid crystal using course control of the x-y position of the tip. The z position of the tip was also coarsely adjusted to be within 100 µm of the glass surface, using the optical microscope view as guidance. Typically, scan sizes of 20 × 20 µm in x-y, with a retraction in z position of 5 µm, were used.

4.4 Simulations and Modelling

4.4.1 Equilibria Involved in Crystal Dissolution

Salicylic acid is a weak acid and this needs to be accounted for in the treatment of dissolution kinetics. In solution, the following equilibrium occurs:

$$HSal_{(aq)} \underset{k_b}{\overset{k_f}{\rightleftharpoons}} Sal^-_{(aq)} + H^+_{(aq)} \qquad (4.1)$$
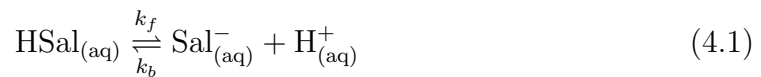
where HSal represents salicylic acid, Sal^- represents the salicylate ion and k_f and k_b represent the forward and backward reaction rates, used herein respectively. The presence of protons in the system is exploited by electrochemical methods as the protons may be reduced at the working electrode tip, as shown in the following equation:

$$H^+_{(aq)} + e^-_{(aq)} \rightleftharpoons \frac{1}{2}H_{2(aq)} \qquad (4.2)$$

These reactions are illustrated in Figure 4.1b.

The removal of protons at the electrode causes the equilibrium in Equation 4.1 to shift to the right, and therefore the concentration of salicylic acid (HSal) will decrease. When the UME surface is in close proximity to the crystal surface, this

undersaturation causes the crystal surface to dissolve:

$$\text{HSal}_{(s)} \rightleftharpoons \text{HSal}_{(aq)} \tag{4.3}$$

as is illustrated in Figure 4.1b.

During an SECM approach of a UME towards an inert surface, the current at the electrode would to decrease to zero (ultimately at contact of the UME with the surface), due to the hindered diffusion of species to the tip electrode close to the surface. However, the present situation, the crystal substrate provides a flux of HSal, J_{HSal}, caused by a local undersaturation between the tip and crystal. The magnitude of this flux is given by:

$$J_{\text{HSal}} = k_{dis}(c_{\text{HSal}} - c_{\text{HSal},sat}) \tag{4.4}$$

where c_{HSal} is the concentration of salicylic acid at the crystal/solution interface, and $c_{\text{HSal},sat}$ is the concentration of salicylic acid in saturated solution [102], and k_{dis} is the dissolution rate constant, which is determined from the current response.
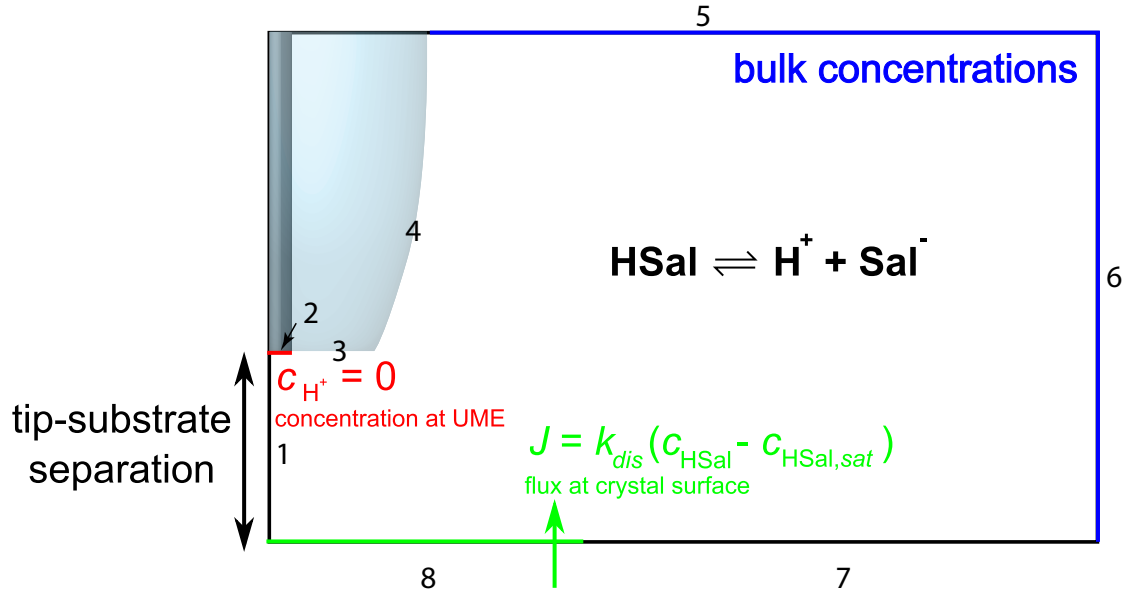
Figure 4.4: The geometry of the FEM model used to simulate approach curves at various values of dissolution rate, k_{dis}, of the active surface is shown. The simulations were also run at various tip-substrate separations (d).

4.4.2 Finite Element Method

FEM modelling was performed using Comsol Multiphysics 4.2a (Comsol AB, Sweden) using a Dell Intel core 7i Quad 2.93 GHz computer equipped with 16 GB of RAM running Windows 7 Professional ×64 bit. The basic geometry for the model is shown in Figure 4.4. To maximise computational efficiency, an axisymmetric, 2D model with symmetry plane boundary 1 was built with a much finer mesh near the surface of the electrode and the crystal. Three inter-dependant species were modelled as shown in Equation 4.1. For the experimental conditions observed, the transport of species was predominantly determined by diffusion, which is treated by

solving the following equation:

$$\nabla \cdot (D_j \nabla^2 c_j) + R_j = 0 \tag{4.5}$$

where D_j is the diffusion coefficient, c_j is the concentration and j is the species of interest. R_j is a kinetic term representing the loss and/or formation of species j according to Equation 4.1 which is always at equilibrium. $D_{\text{Sal}^-} = D_{\text{HSal}} = 8.4 \times 10^{-10}$ m^2 s^{-1} [187], and $D_{\text{H}^+} = 7.6 \times 10^{-9}$ m^2 s^{-1} [188].

The boundary conditions can be understood as follows. As discussed, boundary 1 represents a line of axisymmetric symmetry. On boundary 2, protons are reduced at a diffusion limited rate. Thus:

$$\text{boundary 2: } c_{\text{H}^+} = 0 \tag{4.6}$$

where c_{H^+} is the concentration of protons. For other species (Sal$^-$,HSal), a no flux boundary applies, as follows:

$$\text{boundary 2: } \mathbf{n} \cdot D_j \nabla c_j = 0 \tag{4.7}$$

Boundaries 3 and 4 are glass surfaces on the electrode where no activity occurs. Similarly, boundary 7 represents a no flux boundary, which is akin to the presence

of the glass petri dish, it is not strictly necessary, but less computationally intensive than making the whole of the surface have activity. These are therefore represented in the model by no flux boundaries, as follows:

$$\text{boundary 3,4 and 7: } \mathbf{n} \cdot D_j \nabla c_j = 0 \tag{4.8}$$

where $\mathbf{n}$ is a unit vector normal to the boundary. Boundaries 5 and 6 represent a bulk solution and are therefore determined by the bulk concentrations of HSal, Sal$^-$ and H$^+$, as calculated by MINEQL$^+$ (V-4.6, Environmental Research Software) which used the Davies equation to calculate activity corrected speciation.[208] In these regions,

$$\text{boundary 5-6: } c_j = c_{bulk,j} \tag{4.9}$$

where $c_{bulk,j}$ is the bulk concentration of species j. Finally, and most importantly on boundary 8, a flux condition is enforced, using Equation 4.4. Hence:

$$\text{boundary 8: } \mathbf{n} \cdot (D_{\text{HSal}} \nabla c_{\text{HSal}}) = -J_{\text{HSal}} \tag{4.10}$$

A range of values for k_{dis} were observed for the model. The entire approach curve was modelled using a parametric sweep which altered the geometry of the model by
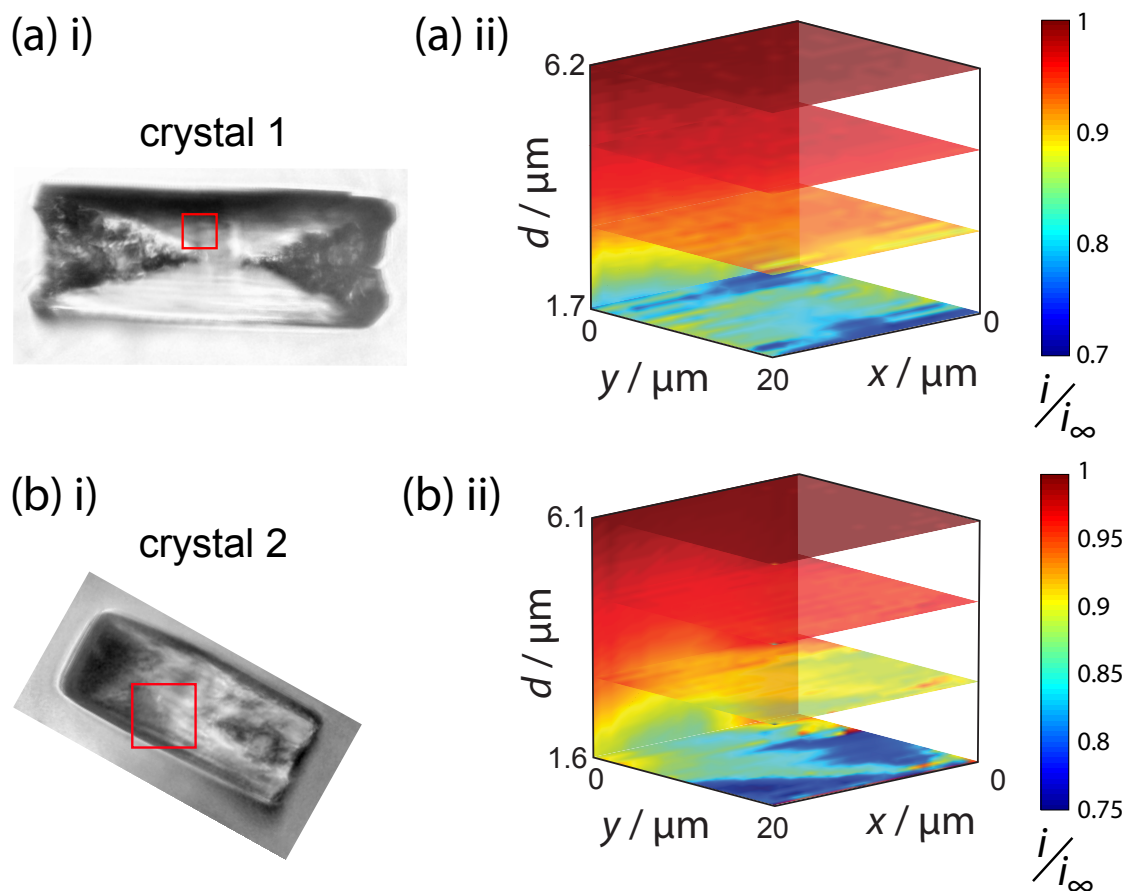
Figure 4.5: A representation of two typical $20 \times 20 \times \approx 5$ µm scans of a salicylic acid crystals. (a) i) Bright field optical microscopy image of crystal 1, the 20×20 µm scan area is represented by the red square. (a) ii) 4d plot showing the I_T of the scan, showing various horizontal and vertical slices through the scan. (b) i) and ii) shows the same information for another crystal imaged.

gradually reducing the separation between the UME and the crystal surface, d.

4.5 Results and discussion

As discussed above, and exemplified in recent work [140, 167], HIC-SECM allows electrochemical flux data to be acquired in 3D over, and above, a surface. Figure 4.5 shows the activity observed over two typical crystals imaged using HIC-SECM.
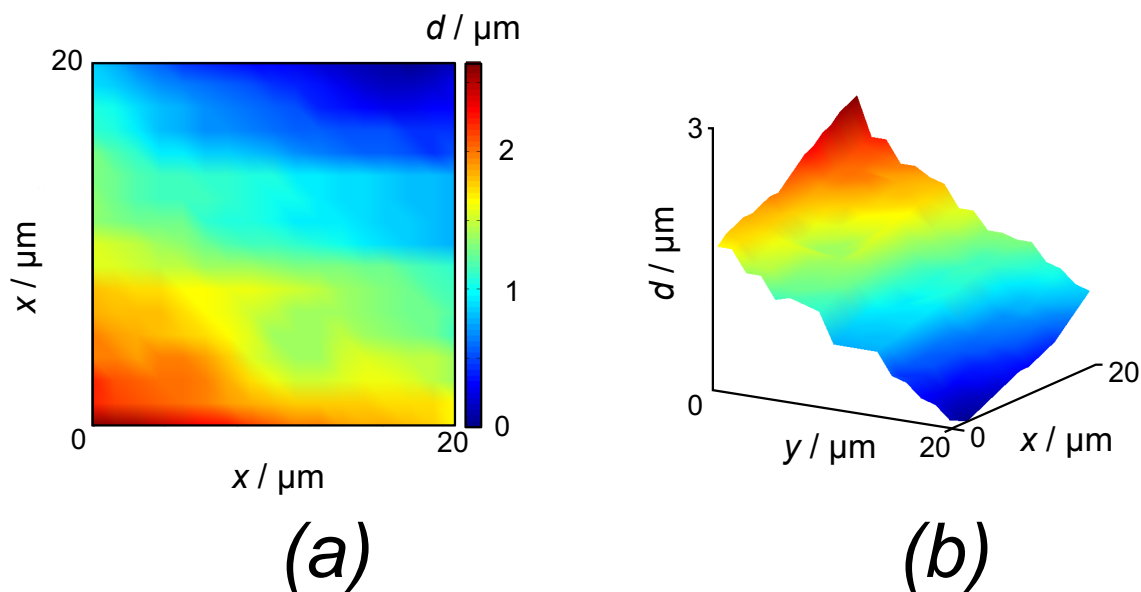
Figure 4.6: The topography of crystal 1 shown in a 2D plot (a) and a 3D plot (b)

Figures 4.5a, ii) and b, ii) show 2D normalised current plots representing slices of the scan in various x-y (parallel to the crystal surface) and x-z (perpendicular to the crystal surface) planes, orientated to show a 3D plot of the data. Herein, these two crystals are distinguished by naming them 'crystal 1' and 'crystal 2' respectively, as labelled. In the electrochemical images, d is the distance between the tip and the crystal. This was obtained from the IC-SECM response, with the 'distance of closest approach' of the tip and the point at which IC determined by knowing that the tip was well aligned over the glass petri dish. Measuring the topography of the crystal shown in Figure 4.6, which shows the topography observed for crystal 1, with the slope on the basal surface of the crystal defining how close the tip was able to approach. It is clear that the surface has an overall tilt, and there is a topographical feature which could be due to an etch pit on the surface.

One of the advantages of using IC-SECM is that the feedback allows for the topography of the surface to be plotted, and this allows for observation of a tilt on the crystal surface, as is shown in the example in Figure 4.6, which shows the topography observed for crystal 1. It is clear that the surface has an overall tilt, and there is a topographical feature which could be due to an etch pit on the surface. For each crystal, the overall tilt of the surface is calculated from the topography measurements, and the distance of closest approach can be calculated.

The images shown in Figure 4.5a, i) and b, i) show bright field optical microscope images of these crystals taken at the end of the scan, with a red square indicating the approximate positions of the 20×20 µm scans in relation to the crystal surface. The normalised UME current I_T of the scan slices is shown in Figure 4.5a, ii) and b, ii) is represented by the colour bars shown and is calculated by:

$$I_T = \frac{i_T}{i_{T,\infty}} \qquad (4.11)$$

where i_T is the measured current and $i_{T,\infty}$ is the current at infinity [44]. $i_{T,\infty}$ is estimated in this case as the furthest point in the approach from the crystal surface (the first current reading of each 5 µm approach).

From Figures 4.5 a ii) and b ii) it can be observed that there is a full drop in tip current from the bulk solution to the surface of crystal 1, typically with a value at the end of the approach curve between 75-80% of the initial current. This is
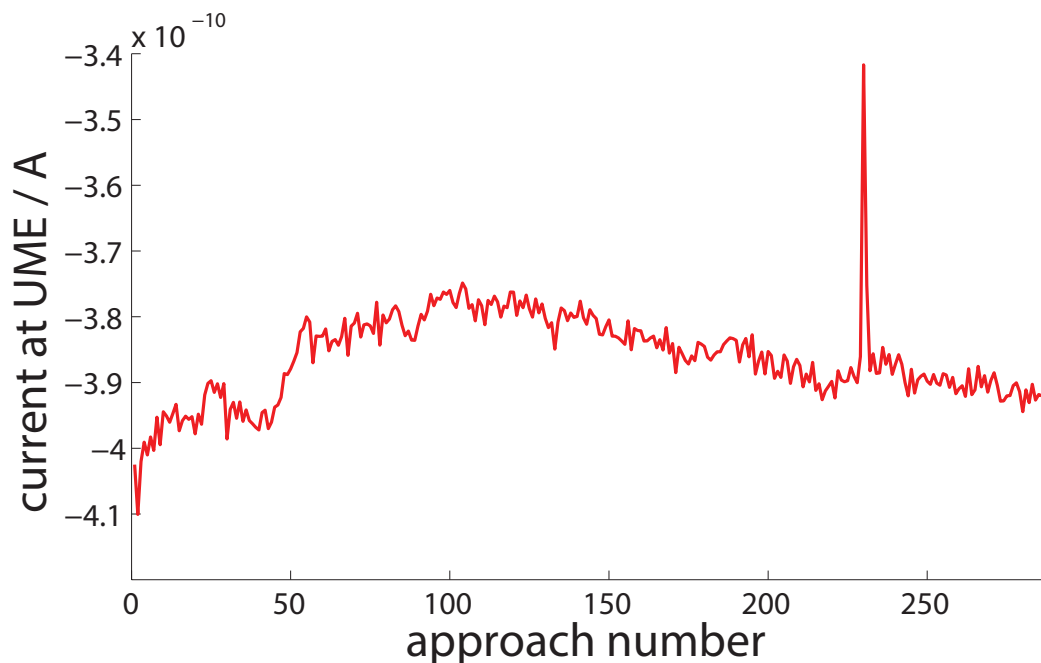
Figure 4.7: The current measured in bulk solution during the period of a HIC-SECM scan.

indicative of finite kinetics. At this distance, it is estimated that from experimental approach curves onto a glass surface that the activity measured would be slightly lower, between 0.6 and 0.65, for an inert surface.

Figure 4.7 shows the current measured in bulk solution (at the furthest value of d from the crystal surface), throughout the experiment for a typical scan. I observe that over time this is incredibly stable, with the exception of very early measurements in the scan. This exemplifies the strength of this method for measuring the kinetics of a surface. Furthermore, the typical current measured in bulk corresponds well with the concentration of protons expected in solution from chemical speciation calculations modelled by MINEQL+.

In order to match each experimental approach curve in the scan to k_{dis} (dissolution
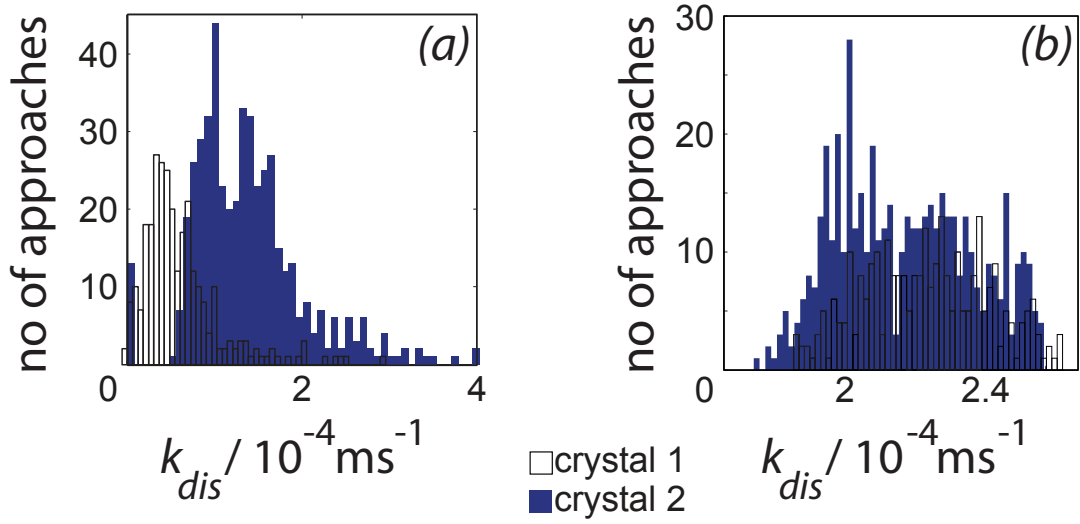
Figure 4.8: Histograms showing the spread of calculated k_{dis} values. for different kinds of analysis. In (a) the gradient of the approach curves are calculated and compared to simulated approach curves for various values of k_{dis}. In (b) the final tip current is compared to the simulated tip current at the predicted distance of closest approach.

rate constant), the gradient of each simulated approach was calculated at a tip-substrate separation of 2.5 µm. This value was chosen due to the fact that there is a considerable difference between the gradients of the simulated approach curves, and this value was in range of the experimental approach curves. This was performed for every approach in the scan, apart from those which were omitted due to their inaccuracies described above, and those which seemed largely anomalous ($> 2\sigma$ from the mean value obtained). The approach curves were analysed between $d = 2.4\text{-}2.6$ for crystal 1, and between $d = 2.3\text{-}2.7$ for crystal 2. The reason for choosing this region of the graph is because there is a larger difference between the gradient of the simulated approach curves as d decreases. Furthermore, the tip current at the distance of closest approach ($d = 0$) is also measured and compared to the simulated data at the corresponding tip-substrate separation.

The distribution of calculated k_{dis} is shown in the histograms in Figure 4.8 for both crystal 1 and crystal 2. Figure 4.8a shows the case where the gradient of the approach curves in a given region are compared to simulated approach curves, and Figure 4.8b shows the case where the final tip current in each approach curve is compared to the predicted distance of closest approach in the simulated approach curves. For crystal 1 the dissolution rate constant calculated from the approach curve gradient was, on average:

$$k_{dis,1} = 6.0(^+_- \ 5) \times 10^{-5} \ \text{m s}^{-1} \tag{4.12}$$

and for crystal 2:

$$k_{dis,2} = 1.4(^+_- \ 0.6) \times 10^{-4} \ \text{m s}^{-1} \tag{4.13}$$

and for the tip current at the distance of closest approach, as shown in Figure 4.8a, the calculated dissolution rate constant for crystal 1 was:

$$k_{dis,1} = 2.2(^+_- \ 0.2) \times 10^{-4} \ \text{m s}^{-1} \tag{4.14}$$

and for crystal 2:

$$k_{dis,2} = 2.0(^+_- 0.4) \times 10^{-4} \text{ m s}^{-1} \tag{4.15}$$

The error on this data may seem large (9-83%) but it is predicted that this is due to the fact that the crystal surface observed is heterogeneous, if active. By analysing the tip current at the distance of closest approach, a much more accurate dissolution rate constant is gained, as exemplified by the smaller error on these results. However, here it is seen that the measurement of k_{dis} is much more similar from one crystal to the next. Again, the dissolution rate is measured to be lower than discovered in previous studies, confirming furthermore that the dissolution is instantaneous.

In previous work combining optical microscopy with FEM simulations and VSI (Chapter 3), the flux values calculated for the (110) face were calculated to be of the order 10^{-5} mol/m^2/s[102].

In the previous chapter, for dissolution experiments, the displacement of crystal faces was measured under conditions where dissolution was extensive such that pitting of the surface reveals faces on the crystal surface which are very high index (highly reactive). In contrast, in the present study, dissolution only happens transiently when the probe encounters the crystal. As seen in the optical microscope images (Figure 4.5), there is no visible pitting behaviour. Therefore dissolution is only induced on the surface momentarily, and the value of dissolution rate is much closer
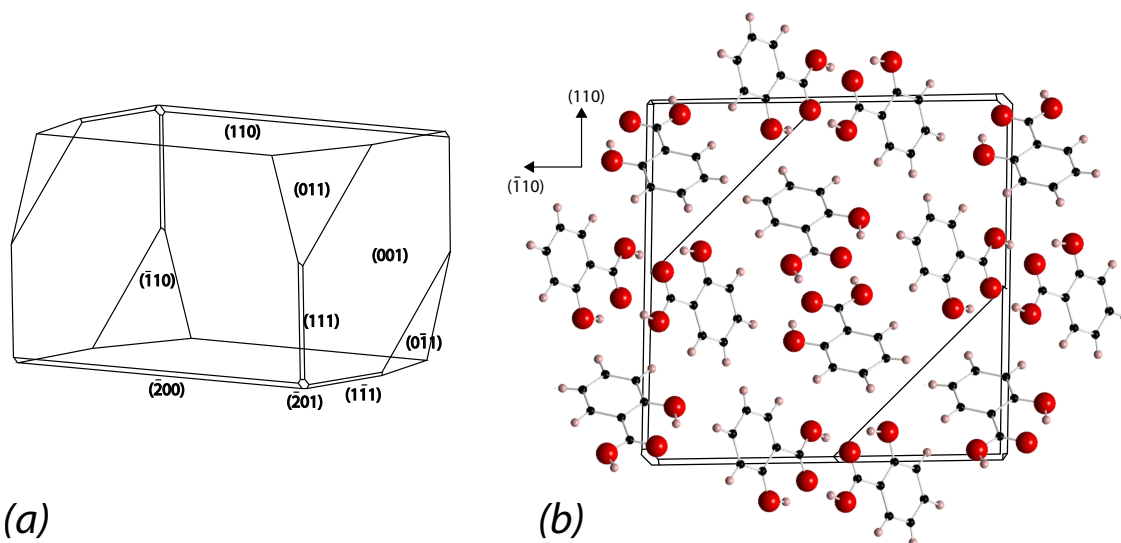
Figure 4.9: (a) The predicted morphology of the crystal and (b) the orientation of salicylic acid molecules with respect to the (110) face.

to that of the intrinsic kinetics of the (110) plane of salicylic acid.

Figure 4.9a shows the morphology of the crystal, as predicted by Mercury 3.0 (Cambridge Crystallographic Data Centre). Figure 4.9b shows the orientation of salicylic molecules in the crystal structure with respect to the (110) face, on which dissolution was investigated by the UME. It was observed from this that the form of the (110) face varies, and sometimes the phenyl groups in the molecules were at the surface, but sometimes the charged carboxylic acid groups were. The (001) face, which was shown to be much more active in Chapter 3, has a large presence of carboxylic acid groups at any given time. When the (110) face has a large presence of phenyl groups on the surface, the crystal is energetically stable, and it is more difficult to allow the surface of the crystal to become solvated, and therefore dissolution will be more difficult. This accounts for the relatively low intrinsic dissolution rate of the (110) face of salicylic acid crystals in water.

4.6 Conclusions

We conclude from this study that crystals of an organic nature do not always readily dissolve, and that exposure of high index facets is necessary before the crystal can dissolve efficiently. We also see that using IC-SECM allows for measurement of surface processes under very well-defined conditions. The method of measuring dissolution processes by SECM is not a new one, but we show here how it is enhanced by IC-SECM, and by studying organic crystals for the first time. We have introduced a new approach where a crystal is made to dissolve by removal of protons by reduction, an approach that could have many applications. Furthermore, the use of proton reduction in SECM is advantageous because the surface of the UME is not fouled by the presence of the hydrogen, which is sometimes problematic when inducing crystal dissolution of an inorganic crystal material, ensuring the tip area remains constant.

CHAPTER 5

NUCLEATION OF BARITE ON FOREIGN SURFACES

AT HIGH SUPERSATURATIONS

This chapter sees a move from general growth and dissolution, and investigate the initial stages of nucleation and growth of crystals. Furthermore, a different crystal system with applications outside of pharmaceutical crystallisation is dealt with; looking at the case of barium sulphate, which forms barite crystals, which are problematic to the off shore oil industry.

The nucleation of barium sulphate on glass substrates functionalised with a positive charge, using PLL, and a negative charge, using PGA, were investigated and compared. A detailed schematic of their structure, and their mechanism of attaching to glass is shown in Figure 2.1 These are of interest because they present different

surface functionalities (charge), and we assess the impact on the rate of nucleation and growth, as well as any impact on crystal morphology and orientation. The initial nucleation and early crystal growth is observed by flowing highly supersaturated solutions of barium sulphate (produced by mixing just before the visualisation over the glass using a strong, hydrodynamic, laminar flow and crystal deposition was visualised using an inverted optical microscope. The corresponding height distribution of the barite crystals produced over time was interpolated from AFM measurements. It was concluded that primitive barium sulphate nuclei are more attracted to the positively charged PLL than the negatively charged PGA surface, suggesting an overall negatively charged nucleus. It was found that during initial nucleation of barite single crystals, the changing flux suggested a mass transport controlled system, which tended towards a surface controlled system once the surface had become more populated and crystal growth was more dominant over crystal nucleation. The calculated flux during this surface controlled behaviour was $1.2(^+_-0.02)$ mol m^{-2} s^{-1} for PGA and 3.8 $(^+_-0.05)$ $\times 10^{-7}$ mol m^{-2} s^{-1} for PLL. These values are compared to the results of a FEM model in which the laminar flow inside the flow cell geometry is modelled and the concentration and flux of BaSO$_4$ is shown. It is shown that there is further evidence that crystal growth on the PLL functionalised surface is close to perfect surface control, and that the PGA experiments do not reach a stage where mass transport is completely negligible.

5.1 Introduction

Scaling is a major issue for the oil industry and many types of crystalline structures such as calcite, halite and gypsum can build up in pipes and cause blockages [103, 104, 209]. This can result in poor functioning of the pipes, and poses a serious danger. Barium sulphate forms a strong and insoluble crystal of barite from the mixture of a high concentration of barium ions in naturally occurring formation water (water as, which is contained in the pores of the rock surrounding the oil well rich in minerals from the rock [210], and the sulphate ions present in sea water, which is injected to maintain pressure in the oil well [211]. Therefore, there is a demand to study what drives the crystallisation of barite in aqueous solution. The system is ideal to study due to the fact that only one morphology of barium sulphate exists, and there are two important faces for stability of crystal structure, the (001) and (120) faces, which determine the morphology [212, 112]. Also, no complicated side reactions occur in the presence of, for example, carbon dioxide, as is the case for calcite and other morphologies of calcium carbonate [213]. On the other hand, this is a big issue for oil well maintenance as the sparingly soluble nature of barite means that it forms at even very low concentrations of barium and sulphate. This also means that it is very difficult to dissolve, and the incredibly strong structure of barite, ≈ 3 on the Mohs hardness scale, makes it difficult to remove by mechanical methods such as drilling [214].

Due to these issues, there are various chemical techniques used to remove scale. One

approach is to add acid, but this does not always work very effectively for sulphates. Now that the problem is commonly known, there is more emphasis on research which seeks to prevent scale from forming altogether, or to retard growth of scale which does form [215, 216, 53, 217]. Various additives can be added to the formation water or the sea water to combat this problem, and there are many studies in literature on this topic [218, 219]. More primitive studies look at altering the concentration of other minerals in water, in order that other more soluble compounds may form in solution, or that minerals will 'poison' the crystal surface and prevent further growth [104, 117, 118]. There is also some value in studies where the ratio of sulphate ions to barium ions in solution [220, 221, 119] is adjusted and the effect on kinetics is investigated. There are many studies into using molecules such as ethylenediaminetetraacetic acid (EDTA), which chelate barium ions in solution and prevent crystallisation [222, 223].

More recent studies involve the use of phosphonates [112, 113, 114, 115] and polymers [224] which have been shown to slow this process. However, there is discussion in literature about the underlying mechanism in particular, whether barium ions in solution are chelated in order to prevent barium sulphate from forming, or whether the crystal growth on certain planes of the growing nuclei is retarded by the (macro) molecules latching onto the surface and preventing incorporation of further crystal growth units [113, 114, 223, 116, 225]. There is also some investigations which suggest that the performance of the inhibitor may be affected by the presence of other ions in the solution [113], some of which occur naturally in either sea water

or formation water, and that the pH of the solution will affect the protonation extent of phosphonate groups [114], and therefore may be problematic in practical applications.

There is also some research into functionalising the surfaces on which the scale forms in order to make nucleation on the surface more or less likely [226]. For example, the use of SAMs can allow for great control and allow for very specific chemical properties to be achieved [109, 110]. Micro-emulsions can be used to produce an environment which encourages or inhibits the growth of barite [227]. This study looks at the simple case of changing the charge on the surface on which the scale forms. This approach could potentially be applied to many other surfaces and systems. Through a combination of chemical inhibitors, and functionalisation, the issue of barite scale can be prevented to a large degree.

In the current study, the result of studying crystallisation at high supersaturations using a flow cell is observed. The supersaturation, S, is defined as follows:

$$S = \sqrt{\frac{[\text{Ba}^{2+}][\text{SO}_4^{2-}]}{K_{sp}}} \tag{5.1}$$

where K_{sp} is the solubility constant. The K_{sp} of barite is very low at 9.81×10^{-11} [228] at 25 °C in atmospheric pressure. The value of the K_{sp} is further confirmed by many dissolution studies of crystal growth, using both bulk crystallisation studies [106, 107, 108] and through conductivity and turbidity measurements, and, more

recently, microscopic techniques such as AFM [229, 118, 230].

The current study focuses on nucleation and growth for which some (homogeneous) bulk studies have been reported [231, 107, 108, 224]. It has been observed by many studies that the initial nucleation of barite crystals follows a first order surface controlled process, whereas when the barite grows a little larger it tends towards a second order process [107, 108] and eventually becomes more mass transport controlled [231, 232].

It is common to use a quartz crystal microbalance (QCM) for a quantitative measure of general crystal heterogeneous nucleation on surfaces [115, 109]. For higher resolution measurements, AFM is also used for this purpose [116, 117, 118, 119] and also been used to observe nucleation islands and step edges on cleaved barite faces. In these AFM studies it has generally been observed that barite forms as 2D islands, supporting the birth and spread model of nucleation [229, 119, 232] as was discussed in Section 1.2.2.

Here, crystal nucleation and growth is investigated using dark field microscopy to determine the area of crystal coverage (size) and the height crystalline of the surface is interpolated from AFM data. This is combined with FEM simulations of mass transport to deduce it's role in the crystal growth process.

5.2   Experimental Methods

5.2.1   Material and Substrate Preparation

All solutions were prepared using 18.2 MΩ cm water (Millipore Inc.). For growth solutions barium sulphate ($BaCl_2$) and sodium sulphate (Na_2SO_4) were purchased (99%, Sigma). Glass slides with diameter 30 mm (Willco Wells) were cleaned with ethanol and then functionalised by covering with either PLL (>99%, Sigma) to create a positively charged surface, or PLL followed by PGA (>99%, Sigma) to create a negatively charged surface. To ensure good coverage, the PLL or PGA was left for at least 20 minutes in each case.

5.2.2   Optical Visualisation Using a Flow Cell

A flow cell was designed in house and built from a Teflon block. The approximate geometry of the flow cell is shown in Figure 5.1. For more detailed dimensions of the flow cell see Section 2.5.6. An inlet of diameter 1 mm was drilled into the top of the flow cell, and the dimensions of the chamber were dictated by the size of the o-ring which sat between the Teflon and the glass slide onto which solution was flowed and crystal nucleation was observed. The particular o-ring used resulted in an approximately cylindrical chamber with diameter 20 mm and a height of 5 mm. The flow cell was placed on an inverted optical microscope, which was used to obtain dark field time lapse images throughout the nucleation and growth process. Flow
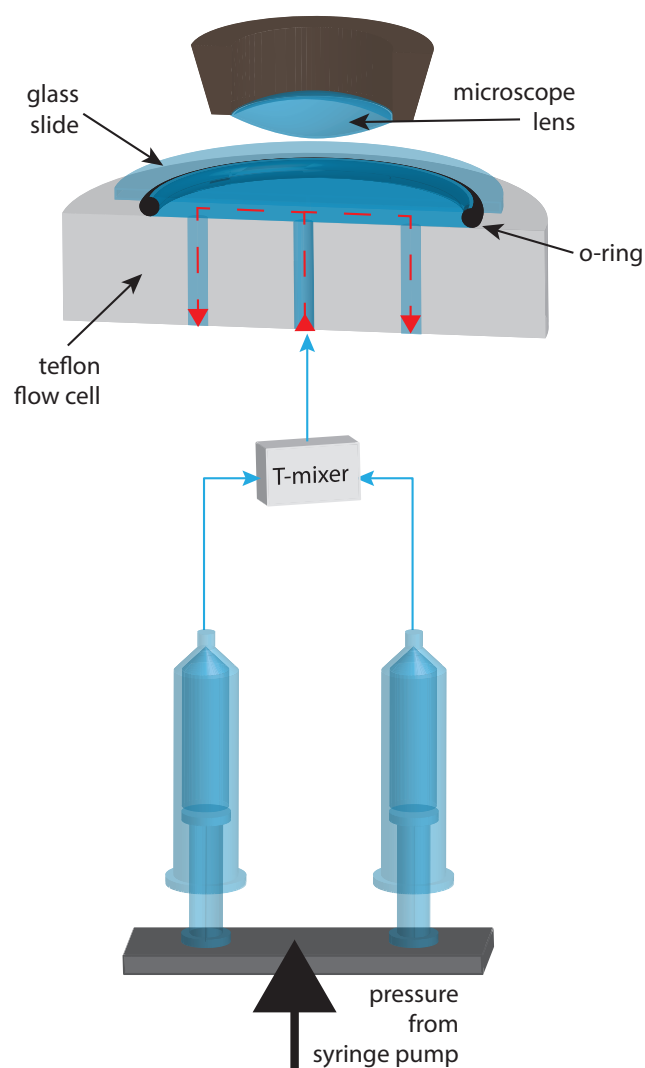
Figure 5.1: Diagram showing the set up for flow cell experiments. Syringes are filled with $BaCl_2$ and Na_2SO_4 solutions which result in a highly supersaturated solution with respect to barite when mixed at the T-mixer junction, using pressure from a syringe pump. This solution flows onto the glass surface contained by a Teflon flow cell. Nucleation is observed by optical microscopy.

was achieved by filling two 60 ml syringes with growth solutions of $BaCl_2$ in one and Na_2SO_4 in the other, and clamping to a syringe pump (KD Scientific), Teflon tubing and junctions were purchased from Omnifit Ltd. and assembled into a T-mixer to mix the growth solutions prior to introduction to the flow cell inlet. This has been shown to result in effective mixing [233].

Solutions of $BaCl_2$ and Na_2SO_4 with equal concentrations were used for all experiments with supersaturations of $S = 10$, 20 and 30 (concentrations of 0.1, 0.2 and 0.3 mM) with respect to barite, when mixed in equal parts, to give a solution with a pH of 6.5. Each syringe was pushed at a flow rate of 1 ml min^{-1}, resulting in a total flow rate of 2 ml min^{-1} at the inlet, and two substrates of PLL and PGA coated on glass slides were used. For each substrate/concentration combination, nucleation was observed continuously for times of 15, 30 and 45 minutes. Between each experiment, the whole system was flushed with 0.05 M sulphuric acid and then with water, using the syringe pump, to remove any crystals or growth solution left in the system.

5.2.3 Observation of Crystal Volume distribution using AFM

For each sample obtained using flow cell experiments, the centre of the glass slide (above the flow cell inlet) was marked and located using a Catalyst Bioscope AFM Bruker. This particular AFM was equipped with an inverted microscope which was used to visualise the surface prior to scanning. Peak Force tapping mode was used
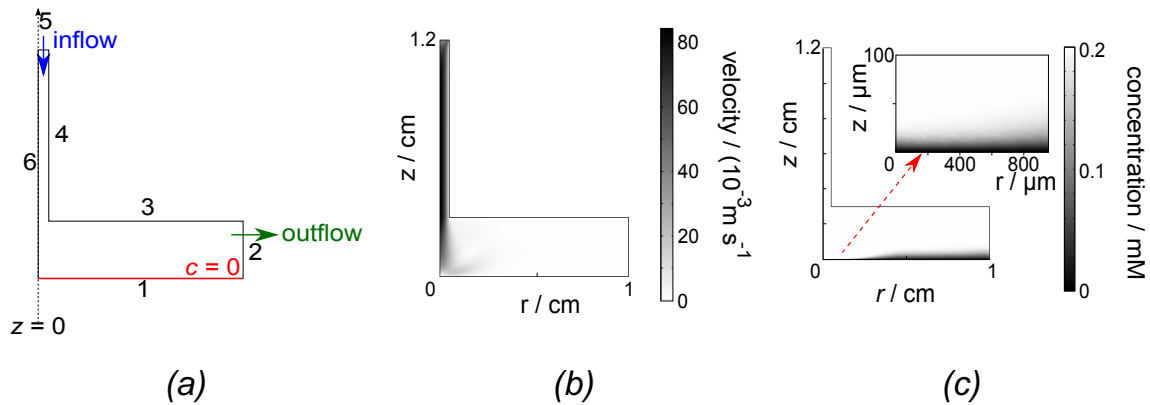
Figure 5.2: Figure showing the results of a FEM model of mass transport in the flow cell used for barite nucleation and growth. (a) The geometry of the model showing the key boundaries and some of the boundary conditions applied. (b) The velocity profile calculated from applying a laminar flow to the inlet of the flow cell at a flow rate of 2 ml min^{-1}. (c) The concentration of $BaSO_4$ in the model, with a small area close to the surface enlarged.

to image the crystals and produce images of a few areas within close proximity of the inlet, for each of the various experiments described above.

5.3 FEM simulations

Simulations were performed on a Dell Intel i7 3.4 GHz computer with 32 GB RAM running Windows 7 Enterprise 64 bit edition. Comsol Multiphysics 4.3b (Comsol AB, Sweden) was used to create and run all simulations.

Comsol was used to model the flow cell in order to determine the concentration profile close to the surface of the glass slide. A 2D axisymmetric geometry was used to model the chamber created by the o-ring in the Teflon cell and the inlet. The boundaries of this geometry are labelled in Figure 5.2a.

Firstly, a laminar flow was applied to the domain enclosed by the boundaries. For this an incompressible Navier-Stokes condition is true, as follows:

$$\rho \mathbf{v} \cdot \nabla \mathbf{v} = -\nabla p + \mu \nabla^2 \mathbf{v} \tag{5.2}$$

$$\nabla \cdot \mathbf{v} = 0 \tag{5.3}$$

where ρ and μ are the density and dynamic viscosity of water respectively, $\mathbf{v}$ is the velocity field and p is pressure. Boundary 6 is the axis of cylindrical symmetry and therefore there is no normal velocity imposed:

$$\mathbf{n} \cdot \mathbf{v} = 0 \tag{5.4}$$

where $\mathbf{n}$ is the unit vector normal to the boundary. Boundary 1 is an inlet with a flow imposed, allowing for sufficient length in order for the inlet to have reached parabolic Poiseuille flow on the boundary. Boundaries 2, 3 and 5 are all defined as walls with a 'no slip' condition, so that:

$$\mathbf{v} = 0 \tag{5.5}$$

Finally, the outlet was defined on boundary 5. Although this was not entirely accurate to the flow cell, it is a fair approximation as the relevant geometric region of the flow cell is that which is closer to the axisymmetric boundary. For this an outlet with no viscous stress or pressure is imposed.

A second step to the calculation was then performed from the solution of this problem, the concentration (c) distribution of soluble barium sulphate is calculated within the flow cell using the transport of diluted species module in Comsol. Mass transport is convective-diffusive in all domains, as follows:

$$-D\nabla^2 c = +\mathbf{v} \cdot \nabla c \qquad (5.6)$$

where c is the concentration of the species of interest, and the velocity field, $\mathbf{v}$ is the calculated by flow. For this problem, boundary 6 is the axis of symmetry and boundaries 2 and 3 are no flux boundaries where the following conditions apply:

$$-\mathbf{n} \cdot \mathbf{N} = 0 \qquad (5.7)$$

$$\mathbf{N} = -D\nabla c + \mathbf{v}c \qquad (5.8)$$

In order to predict the concentration boundary layer close to the surface of the glass

slide, some concentration conditions are applied to the remaining boundaries. The inlet (boundary 1) assumes that the bulk concentration c_b is held:

$$c = c_b \tag{5.9}$$

At the surface of the glass slide (boundary 5) it is assumed that the concentration is equal to zero:

$$c = 0 \tag{5.10}$$

The model thus predicts the maximum possible rate of mass transport controlled growth, for comparison to the experimental data. Over the region of interest, it is a wall tube flow [234]. The model was calculated for the three bulk concentrations performed experimentally, which were 0.1, 0.2 and 0.3 mM. It can be observed from the solutions that the depletion region (concentration boundary layer) close to the surface of the glass slide spans over 100 µm normal to the surface. This is approximately an order of magnitude larger than the size of crystals obtained during experiment and the inter-crystal distance (*vide infra*). It is also observed that for the region which is imaged by the inverted optical microscope, a constant, planar field diffusion is observed, it is only much further along the radius of the flow cell that the depletion layer vastly increases.
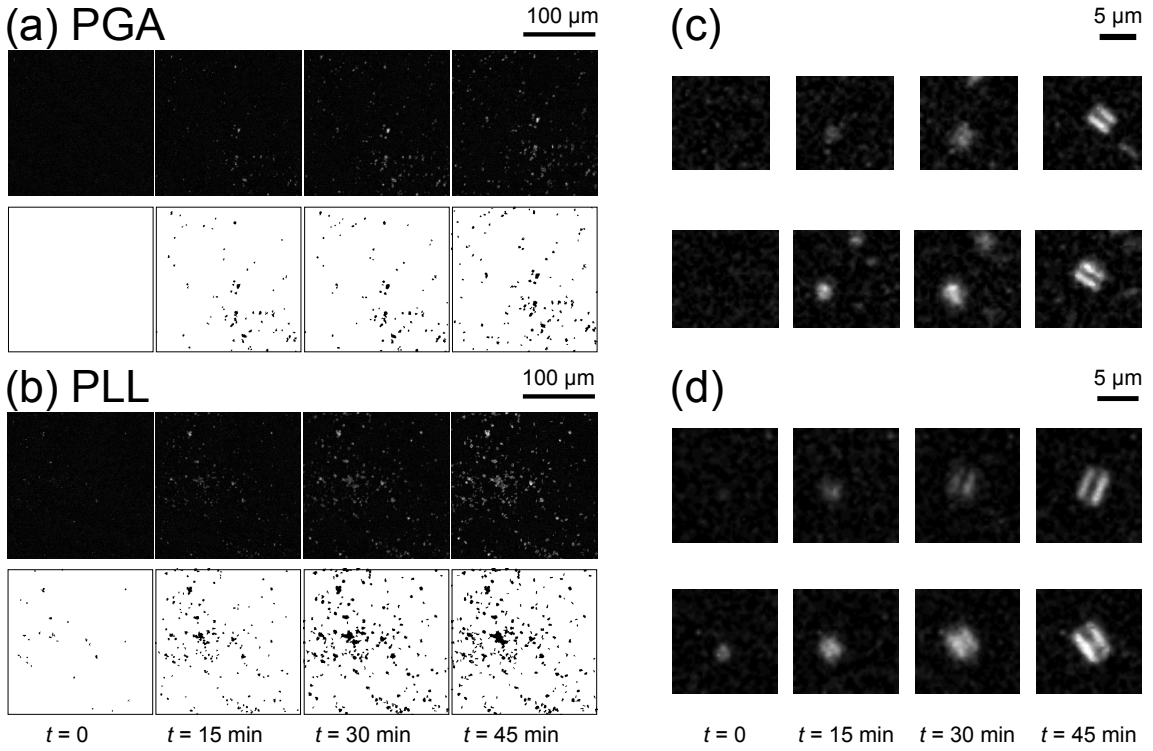
Figure 5.3: A selection of time lapse images for the flow cell experiments shown over 45 minutes for a concentration of barium sulphate of 0.2 mM on a glass surface coated with PGA (a) and PLL (b). For each case, the top row shows a small area of the original dark field microscopy images taken, and the bottom row shows the corresponding mask of the image taken from image processing the time lapse images. (c) the growth of two individual micro-crystals of barite on PLL taken from these dark field images.

Further disscussion of the model, and comparision to experimental data, will be included below in Section 5.4.3.

5.4 Results and Discussion

5.4.1 Time Lapse Videos

For the three concentrations investigated, different behaviour was observed. For 0.1 mM changes in area were difficult to measure on this timescale due to the

resolution of the microscope, as there was relatively little deposition. Particularly for the PGA surface, for which there was found to be less barite deposition, there was very little coverage at all. At the higher concentration of 0.3 mM it was observed that the nucleation was sporadic and not consistent from one experiment to the next. It is assumed that at this concentration there is a much larger amount of homogeneous nucleation in the flow system. This could result in build up of material in the inlet which will be emitted at uncontrolled times and some particles may not ever deposit. As well as causing extra material formed in solution to deposit on the surface observed, uncontrolled turbulence of the system is also likely.

The experiments performed at a concentration of 0.2 mM did not show any of these problems, and nucleation appeared to be controlled and heterogeneous. For the two surfaces, PGA and PLL, the deposition over time is shown in Figure 5.3a and b respectively. The top row of images show a set of dark field images, for a cross section of the images captured and analysed, cropped from the original image. The bottom row shows the mask of particles on the surface. This was produced using ImageJ, by subtracting the background from an 8 bit version of the original image, enhancing the contrast and then converting to a binary image. Any particles below 3.5 μm^2 were ignored and removed from the binary image, as they can not be distinguished from extraneous noise from the image.

It is clear from Figures 5.3a and b that the barite crystals have a higher affinity for the surface coated with the positively charged PLL than the negatively charged
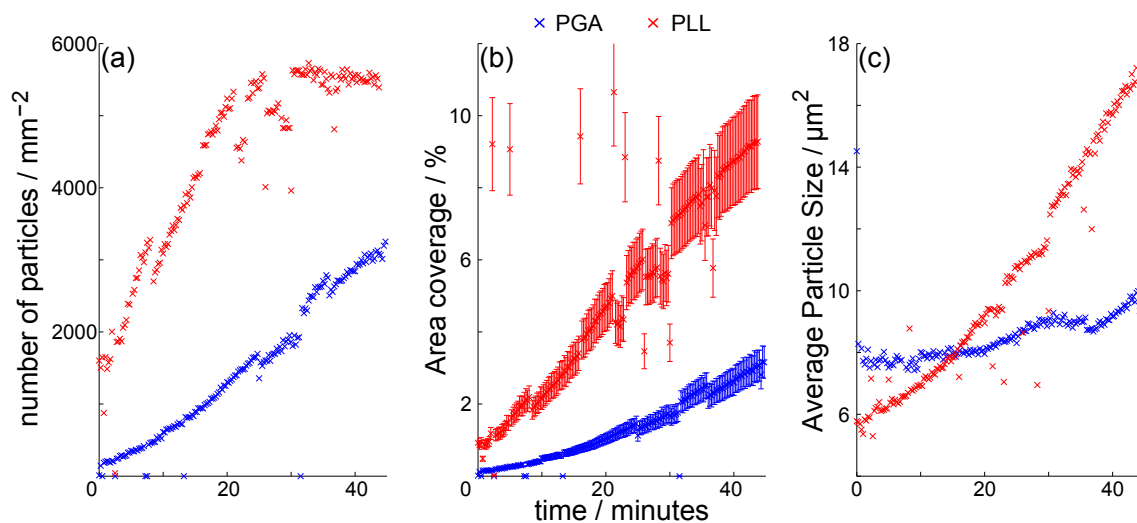
Figure 5.4: Results of particle analysis of time lapse images from flow cell experiments, for PGA (blue) and PLL (red) coated glass surfaces. (a) The number of particles deposited on the surface over time. (b) The percentage total coverage over time. (c) The average particle size over time.

PGA. When the crystals have a fully formed tabular structure it is clear that both surfaces have crystals with the same orientation and morphology. Some typical, reasonably isolated, crystals are shown in Figures 5.3c and d for PGA and PLL respectively. Again, the PLL forms slightly larger crystals during the time period observed.

In all cases where it is possible to track the morphology throughout the flow cell experiment, and for which it is possible to obtain qualitative conclusions about the morphology observed, the crystals eventually grow into a tabular structure. There is no observable amorphous material, and all particles which deposit on the surface, are still observable at the end of the flow cell experiment, continuing to grow. It is therefore reasonable to assume that the glass surface is only populated by barite crystals, as this is the only known morphology of the barium sulphate.

ImageJ was used to analyze the dark field images, using the same process described above, to form a mask of the whole image, which had an area of 618 × 462 µm. A particle analysis was performed on this binary image and then the population of crystals on the surface could be calculated. Typical results of this are shown in Figure 5.4. Again, it is clear that the PLL surface has a higher coverage over time. The PGA surface seems to have a constantly increasing number of particles (Figure 5.4a) whose size does not increase drastically (Figure 5.4c). The PLL surface quickly becomes very populated and these large, fast growing crystals consume material quickly, preventing further nucleation, as can be seen from the plateau in Figure 5.4a, and the much steeper curve for PLL in (Figure 5.4c). It is also clear that PGA continues to nucleate throughout the period of the time lapse sequence as the number of particles continues to increase approximately linearly, and a great deal of the flux on the surface is required to overcome the energy barrier for nucleation, rather than contributing to general crystal growth of existing nuclei.

5.4.2 AFM Analysis

AFM images are shown in Figure 5.5 for flow cell experiments of times 15, 30 and 45 minutes, for both substrates investigated. These show typical 50 × 50 µm areas of the surface. As expected, the longer the time of the flow cell experiment, the greater the coverage and the taller are the crystals on average. The typical crystal height is slightly higher for barite nucleation on PLL than PGA.
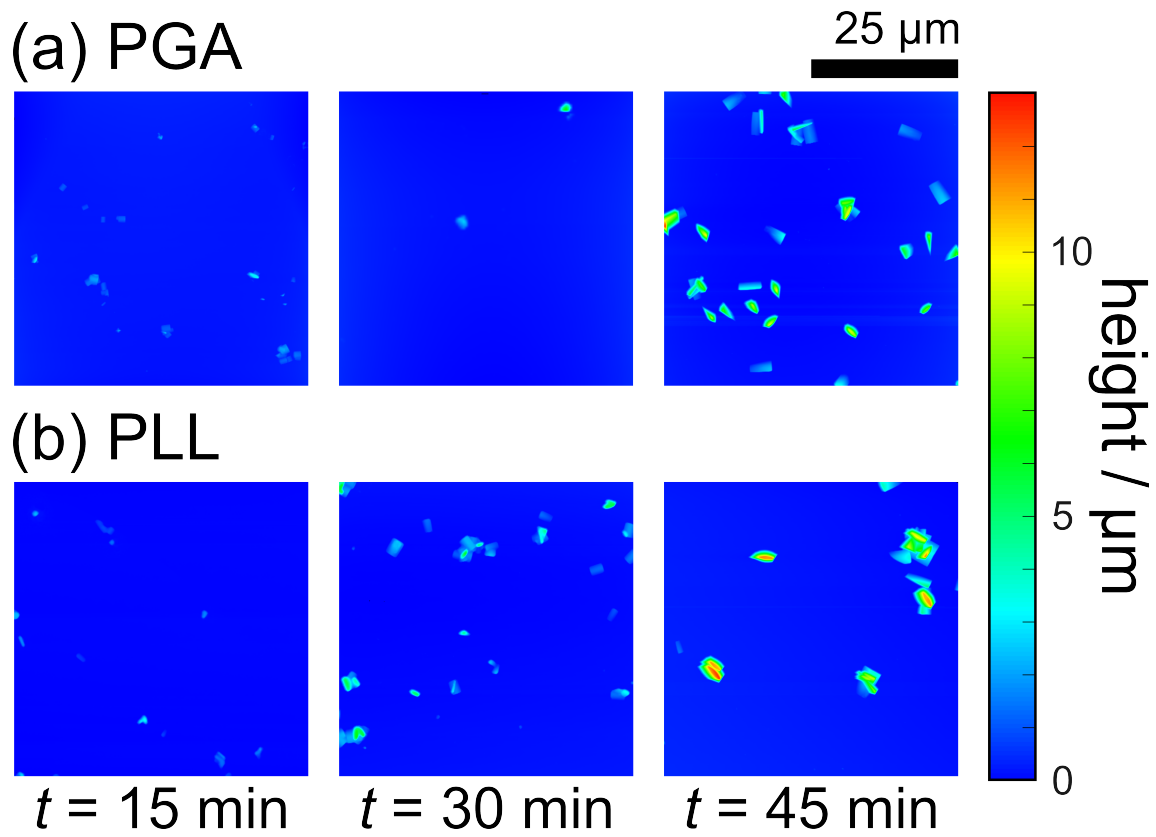
Figure 5.5: Peak force tapping AFM images showing typical areas of the samples for flow cell experiments of 15, 30 and 45 minute runs for a concentration of 0.2 mM on (a) aPGA coated surface and (b) a PLL coated surface.
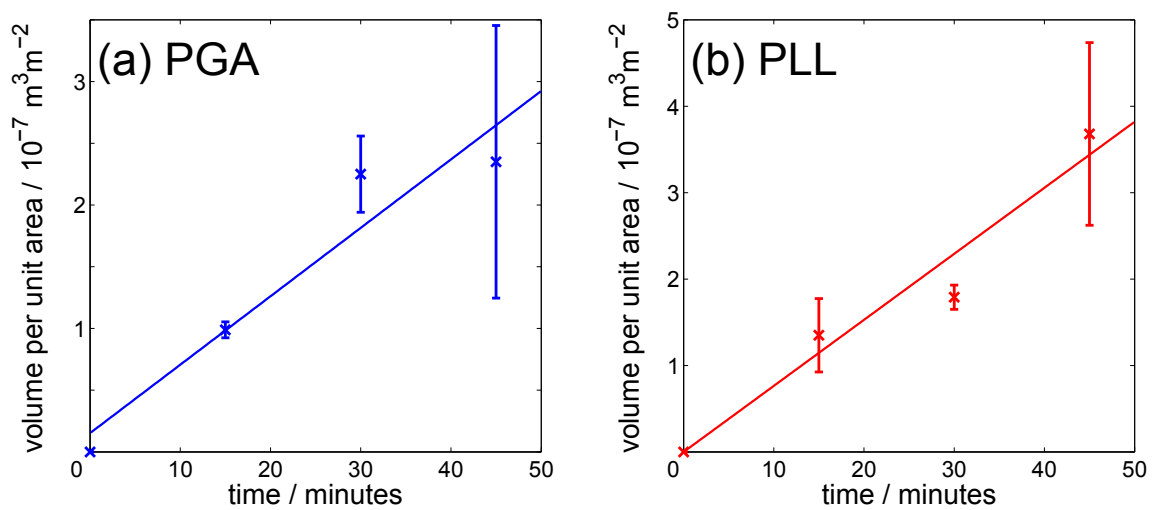
Figure 5.6: The average unit volume per unit area for AFM samples from flow cell experiments for a surface coated with (a) PGA and (b) PLL.
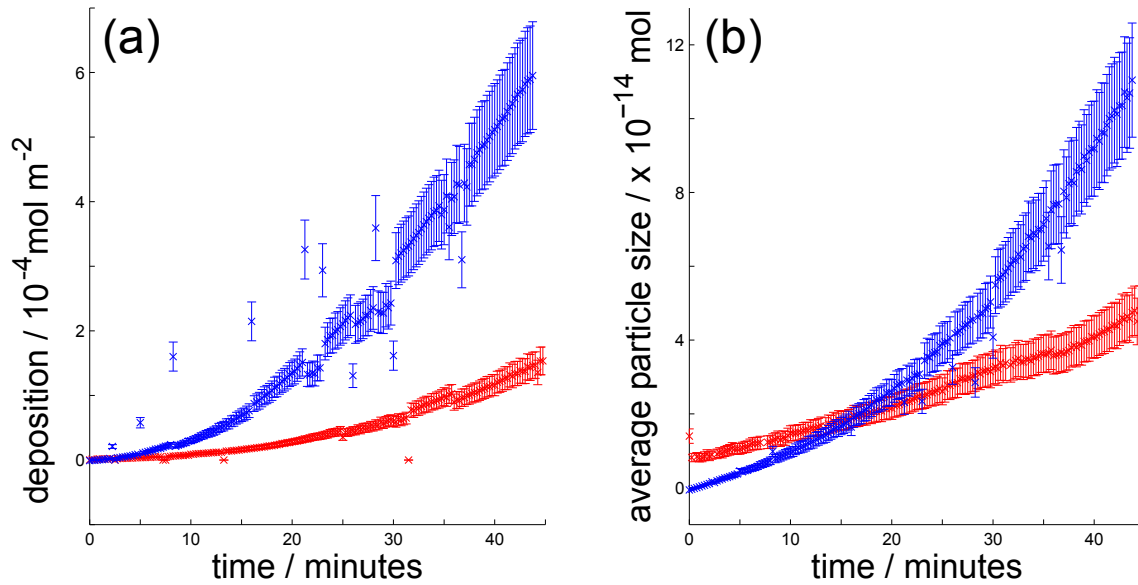
Figure 5.7: The molar volume of material deposited on the surface during a flow cell experiment over time for glass coated with PGA (red) and PLL (blue). (a) Shows the molar volume per unit are of the surface (b) shows the molar volume on average for a particle.

Figure 5.6 shows the average crystal volume per unit area of crystals for the case of PGA and PLL, over time. This correlation is used to estimate the overall volume on the area imaged by dark field microscopy, using the percentage area coverage shown in Figure 5.4b. The result of this is shown in Figure 5.7.

It is observed from Figure 5.7a that crystal growth occurs much more readily on the PLL surface than PGA consistent with the images in Figure 5.3, but both growth curves show broadly similar behaviour. The flux towards the surface (slope of the amount of deposition vs time at any time) is initially low, and gradually increases as more barite deposits on the surface. This is indicative that the crystal initially grows under surface control and gradually tends towards a mass transport controlled system. For the case of PLL this mass transport control seems to be reached by

about 30 minutes into the experiment, whereas the PGA seems to take much longer to reach this stage, and it is arguable that it isn't reached at all. As was noted earlier, Figure 5.4a, the number of particles on the PLL seems to plateau, whereas the number of particles on PGA does not reach that stage before the end of the 45 minutes.

In the final five minutes of the experiment, the average flux of material on the area observed for each surface is as follows:

$$J_{\text{PGA}} = 1.2(^+_-0.02) \times 10^{-7} \text{mol m}^{-2} \text{ s}^{-1} \tag{5.11}$$

$$J_{\text{PLL}} = 3.8(^+_-0.05) \times 10^{-7} \text{mol m}^{-2} \text{ s}^{-1} \tag{5.12}$$

Figure 5.7b shows the average molar volume for a particle, based on the distribution of particles over the whole of the surface observed by optical microscopy. Again, there is an induction period before a steady state is observed, which shows further evidence that the system takes time to reach a mass transport controlled state. This induction period suggests that the initial step of forming nuclei on the surface of the glass is the most energetically difficult, and as larger nuclei form, growth units attach more readily to the surface.

5.4.3 Results of FEM Model

Figure 5.2 shows the results of the FEM model described in Section 5.3. The resulting velocity field produced by the laminar flow condition is shown in Figure 5.2b. It can be seen that this is well defined along the inlet, but that the velocity varies closer to the surface of the flow cell, suggesting that a reasonably small number of species flowing into the surface actually arrive at the area of the glass surface being imaged.

To investigate the effect of this, the concentration profile is shown in Figure 5.2c. The concentration of the $BaSO_4$ is constant for the majority of the domain, but there is a layer close to the surface where the concentration falls. It is observed that, due to the inlet flow, the boundary layer is much smaller close to the inlet, and becomes larger moving away from the centre. This suggests a high mass transport. The other 2D plot in Figure 5.2c shows a zoomed in region of the flow cell, to show this concentration boundary layer more clearly. The largest dimension of the optical microscope images obtained from flow cell experiments is 618 µm, and it is clear that the concentration boundary is uniform in this region. The concentration changes to bulk value within 50 µm of the surface. This is much larger than the length-scale considered for which individual crystals on the surface grow. Maximum crystal dimensions observed for the case of PLL surface at 0.2 mM are around 5 µm and even early on in the experiment, the measured average separation of these particles is less than 30 µm.
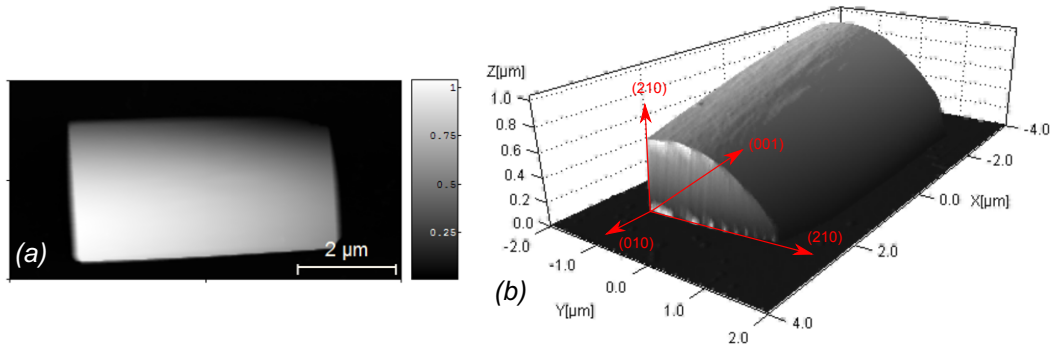
Figure 5.8: AFM image showing the morphology of a single micro-crystals seeded on PGA in (a) 2D and (b) a 3D representation with predicted faces.

The flux measured from the model, normal to the surface of the glass, for an area covering the largest dimension of the optical microscope images is on average $3.8(^{+}_{-}0.3) \times 10^{-7}$ mol m^{-1}. These values are compared to those measured by image processing and AFM analysis. The predicted flux on the surface is between 3×10^{-7} and 6×10^{-7} mol m^{-2} s^{-1}. This is very similar to the rate at which of material was deposited. For the case of the PLL surface, the experimental calculated flux is 3.8×10^{-7} mol m^{-2} s^{-1} in the last five minutes of the experiment. This is in range of the calculated theoretical flux, suggesting a system that is transport controlled, as almost all species diffusing to the surface become deposited as solid barite. For the case of PGA, the average surface flux is a little lower at 1.2×10^{-7}.This is indicative of a more surface controlled system where not all material available is able to successfully diffuse to the glass surface.

5.4.4 Discussion of crystal orientation

As was mentioned previously, crystals observed eventually achieve the tabular barite structure, which suggests that crystals develop with the same orientation with respect to the surface. From observations of morphology and comparison to data in literature, it is inferred that the crystals have the (010) plane in line with the glass surface, regardless of whether the substrate is coated with PLL or PGA. An example of a typical crystal on PGA, which has been seeded using a solution of $BaSO_4$ of supersaturation $S = 22.5$ (concentration = 0.225 mM), is shown in Figure 5.8. The orientation of the crystal has been derived from observations in literature [119, 115]. The indifference to the surface functionality is probably due to the repeating orthorhombic structure of barite, and it is likely that growth units can attach in different ways, favouring the positively charged barium ions for the case of PLL, and favouring negatively charged sulphate ions for PGA. The fact that the positively charged PLL is more successful as a functionalised surface suggests that there is a greater chance of the surface charge of primitive nuclei having a negatively charged surface.

5.5 Conclusion

It has been shown that the substrate charge can have a great effect on the affinity for scales, such as barite, to deposit on a surface. Therefore the materials used to

produce oil well tubing, and other surfaces where these scales are prolific, should be considered for their suitability if they are to be robust enough to last without scale build up. In the current study the simple case where the surface is functionalised with a positive and a negative charge is considered, and found that nanoparticles much more readily nucleate and grow on surfaces with a positive charge, such as PLL than a negatively charged surface such as PGA.

Much research into preventing barite scale focuses on the use of additives to retard crystal nucleation and growth, but here it is shown that the nature of the surface also plays a great role in influencing the extent to which scale builds up. Here simple polymer films to produce different surface charges are used, but there are plenty of more specific methods of functionalising the surface with particular functional groups, some of which are explored in the literature, but there is a lack of focus on this work in general.

Furthermore, a method is developed for monitoring the nucleation of any crystal system, by visualisation and image processing techniques. It was also possible to gauge information about the mass transport behaviour of the system by utilising additional data from the FEM.

CHAPTER 6

NANOPRECIPITATION OF BARITE USING ION CONDUCTANCE

In this chapter, the early stage of nucleation and growth of barite is investigated, using a new technique, based on nanoprecipitation in a small capillary with monitoring of the current to reveal the early stages of crystal nucleation and growth time.

A nano-scale pipette filled with electrolyte and a sodium sulphate solution was immersed in another electrolyte bath containing barium chloride, with a QRCE contained in each of the pipette and the bath. Precipitation of barium sulphate was induced by production of a strong ion current by applying a bias (typically in the range of 1-3 V) between the two QRCEs. The current measured by the electrode inside the

capillary showed strong evidence of nucleation, and eventually complete blockage of the nanopipette. When a larger bias was applied, a larger current (higher ion flux) was observed, and a shorter time from initial nucleation to complete blockage was observed. Phosphonate scale inhibitors were added to the bath in increasing concentrations to investigate their effect and it was shown that the inhibitors caused the nucleation time, to increase. nitrilotris(methylene)triphosphonic acid (NTMP) was shown to be a more effective inhibitor than hexamethylenediamine tetra(methylene phosphonic acid) (HDTMP) in these experiments. Occasionally a more complicated transient is observed, where it is assumed that nucleation of the particle is less straightforward, and possible explanations for this are explored within. This simple new approach appears to be a particularly effective way to probe the nucleation and growth of inorganic crystals.

6.1 Introduction

As discussed in the previous chapter, barite scale is a major issue for maintenance of off-shore oil rigs, and is produced when naturally barium-rich formation water comes into contact with sea water, which has high concentrations of sulphate [103]. This practical application, as well as the fact that barium sulphate is a model crystal system in which complicated side reactions do not occur, mean that the growth and dissolution behaviour and kinetics of barite have been researched extensively [235, 212, 229, 231, 107, 221, 116]. Other scales such as calcite and gypsum also cause

similar issues [236, 215, 217], but barite is particularly insoluble, meaning that only trace supersaturations can still give a very high likelihood of precipitation, and the barite crystal is incredibly strong and dense, making removal by mechanical methods incredibly challenging [214]. Removal by chemical methods involves acidic conditions, which are not always successful for sulphates.

Studies thus commonly focuses on prevention of barium sulphate crystallisation, rather than removal. The most common way to prevent nucleation from occurring is by using additives which retard growth or prevent nucleation. Some methods have investigated the use of increased concentration of additional minerals [117, 118] in aqueous solution, in order that compounds of more soluble scales form, which cause fewer problems. However, a more directly effective method is to add chemicals which prevent growth by binding to barium ions in solution, often using molecules which chelate, such as EDTA [237, 222, 223]. Molecules chosen for this purpose often contain functional groups which readily bind to the barium ions, or attach to sites on the crystals. At present, the most prominent of these is to use phosphonate inhibitors [104, 112, 224, 115], which contain phosphate groups attached to amino groups. The strong polarity of the nitrogen-phosphorus bond means that the phosphate groups of these inhibitors readily attach to barium ions, and sometimes dock onto vacancies in the barium sulphate lattice where sulphate ions would usually attach.

The nature of the phosphonate molecule can affect its inhibition properties. De-

pending on the length of the alkyl chain between phosphonate groups in some (macro)molecules may effect a molecule's suitability to latch onto the lattice, or its ability to form a complex with metal cations. This has been investigated using various modelling methods [238, 239, 114, 225]. However, smaller molecules such as NTMP contain bonds with much higher polarity, and improve the molecule's ability to bind and prevent inhibition. There is some debate in literature as to the favoured mechanism of inhibition, and one of the aims of this chapter is to separate these processes and attempt to resolve this, by studying NTMP, which contains no hydrocarbon component at all, and HDTMP, which contains a hexyl chain between the active amino-phosphate groups. These two inhibitors have been studied both individually [240, 237, 241] and compared [242] in literature, with an application of retarding the growth of barite.

As was discussed in previous chapters, electrochemical methods can be used to obtain quantitative information about crystal growth and dissolution. The use of UMEs as in Chapter 4 allows crystal growth processes to be measured under highly surface controlled conditions, where mass transport is well defined. In this chapter, even smaller scale conductometric electrochemistry was used, and produce nanopipettes [243, 244] which consist of a capillary pulled to a very fine point (typically 10-100 nm), which contains a QRCE. The capillary is filled with an electrolyte and bathed in a further electrolyte solution. Nanopipettes and artificial nanopores are often used to mimic biological systems [245, 246], as they are similar in design as nanopores produced by proteins which behave as ion channels [247, 248].

There is some application of nanopipettes as imaging probes for SICM and the analysis of surface processes [249]. However, the method of interest in this thesis is the use of the nanopipette to produce strong ion current densities, and therefore highly supersaturated solutions (locally), which induce precipitation. This 'nanoprecipitation' [247, 248, 250] allows a particle to form in the nanopipette, which affects the ion current which is able to flow, as the blockage essentially alters the nanopipette's dimensions. Equally, the nanopipette can be used to produce very low supersaturations and cause the dissolution of nanoparticles. Therefore, great control over the nucleation, and initial stages of crystal growth is possible, and made more effective by advances in nanopipette fabrication, allowing for very small dimensions to be achieved.

6.2 Experimental

6.2.1 Solutions

All solutions were made up using 18.2 MΩ cm water (Millipore Inc.). All chemicals used were purchased from Sigma Aldrich. A supporting electrolyte of 100 mM KCl was used in all solutions, alongside a buffer of Trizma-HCl, with a concentration of 10 mM. This ensured that all inhibitors used are held at a pH 7, which meant that the protonation of the inhibitors can be controlled (see discussion later on in Section 6.3.2). The nanopipette also contained Na_2SO_4 of concentration 10 mM

and the electrolyte bath contained $BaCl_2$ with a concentration of either 2 or 4 mM (detailed below for individual experiments). Inhibitors were NTMP and HDTMP, added to the electrolyte bath in varying concentrations of the order µM.

6.2.2 Nanopipettes

Nanopipettes were fabricated using borosilicate glass capillaries (outer diameter 1.2 mm, inner diameter 0.69 mm, Harvard apparatus) pulled to a fine point with a tip radius of 60 nm, using a commercial laser puller (P-2000, Sutter Instruments; parameters of: Line 1: Heat 350, Fil 3, Vel 30, Del 220; Line 2: Heat 350, Fil 3, Vel 30, Del 180, Pul 120). The nanopipette was filled with an electrolyte solution as specified above and a Ag/AgCl QRCE was placed inside the pipette. It was then immersed in the electrolyte bath, contained in a petri dish (Will-co Wells).

6.2.3 Instrumentation

A second Ag/AgCl QRCE was placed in the electrolyte bath and connected to the QRCE in the nanopipette, and a bias was applied directly to it. The current was measured at the QRCE in the nanopipette using a current-to-voltage converter.
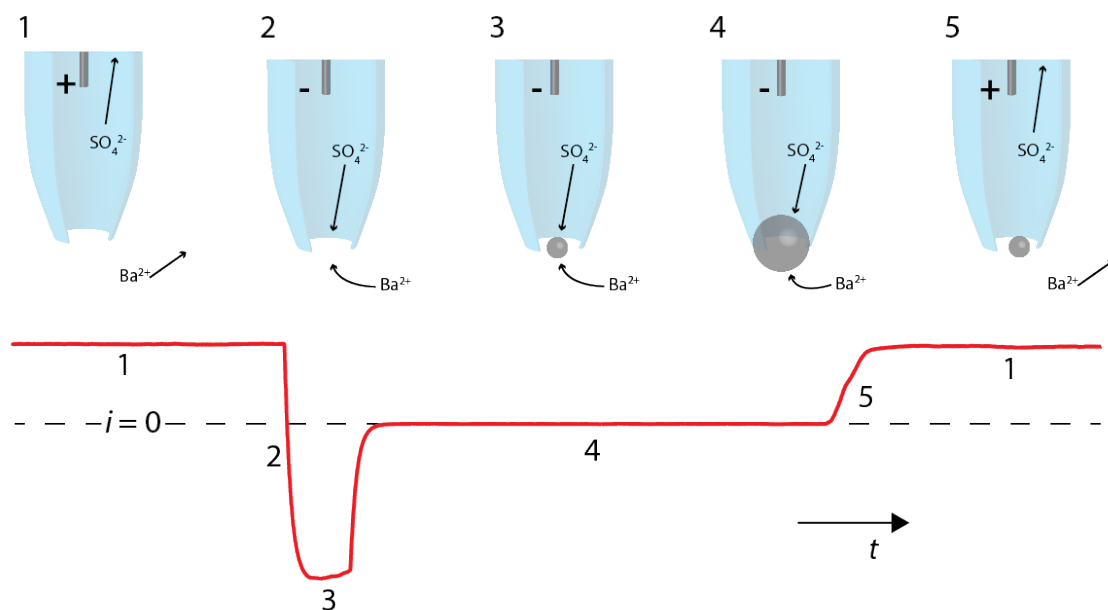
Figure 6.1: Diagram showing the process of nanoprecipitation in the nanopippette and the corresponding current transient observed. 1) A positive potential was held and the QRCE inside the pipette behaved as an anode, drawing ions required for nanoprecipitation to occur away from the pipette opening. 2) The potential was switched to a negative bias, causing the QRCE inside the pipette to become a cathode. Sulphate ions were pushed out of the pipette opening, meanwhile barium ions in solution were pushed towards the cathode. 3) The supersaturation at the pipette opening was then above the K_{sp} of barium sulphate, and precipitation started to occur. As the nanoprecipitate started to grow, the pipette opening became more obscured and less ion current was able to flow through the tip. 4) Eventually the nanoparticle became large enough to completely block the tip and the current measured fell to zero. 5) The potential was changed again, so that the QRCE in the pipette was negative, which caused the area around the precipitate to be undersaturated causing dissolution and sometimes ejection of the precipitate.

6.2.4   Current Measurements

The general shape of a typical current transient for the experiments performed is shown in Figure 6.1, along with cartoons of the tip which explain the behaviour. Initially a positive potential was applied to the QRCE in bulk solution (1), the potential was then flipped to a negative potential in order to induce nucleation (2, 3 and 4). Eventually the potential is flipped back to positive, and this process was repeated.

Variable potential measurements

Initial experiments performed involved holding the electrode in bulk solution at a potential of +3 V for 4 s and then flipping to a negative potential for 1 s and repeating. The negative potentials used are 0 V, -1 V, -2 V and -3 V consecutively, and this process was repeated to observe repeatability and robustness of the nanopipette.

Measuring Inhibitor Effectiveness

For inhibitor experiments, the electrolyte bath also contained low concentrations of inhibitors NTMP and HDTMP of concentrations 10, 30, 50, 70 and 90 µM. The potential was held at +3 V for 20 s and flipped to -3 V for 5 s, for nanoprecipitation to occur. This was repeated several times for each inhibitor concentration.

6.3 Results and Discussion

The process of nucleation and blockage of the tip opening was shown in Figure 6.1, and the explanation for this transient is described in more detail in this section. Initially, the potential at the QRCE in bulk was held at a positive value, (Step 1 in Figure 6.1) which resulted in a positive current being measured at the QRCE in the pipette. Nothing of note happened inside the pipette apart from that an ion current flowed causing sulphate ions to move towards the cathode (in the pipette) and barium ions to move towards the anode, thus giving an undersaturation of barium sulphate at the tip opening.

When the potential was changed to a negative value (Step 2), the current measured also changed polarity, and this caused the ions to flow in the opposite direction, causing a higher saturation of barium sulphate to exist near the capillary opening. If the potential is large enough in magnitude, and the supersaturation at the tip opening exceeds the K_{sp} of barite, nucleation will occur in the tip (Step 3). As the nucleus got larger, the current measured was smaller (less negative, until eventually the tip becomes completely blocked and the current measured drops to zero (Step 4). Upon switching back to a positive potential, the current became more positive (step 5) as the nanoprecipitate decreased in size from the undersaturation at the tip opening and/or was ejected due to electrophoresis.

6.3.1 Varying the negative potential

Figure 6.2 shows the change in current observed at the pipette electrode when a positive potential was applied to the electrode in bulk solution and then flipped to a potential of 0, -1, -2 and -3 V for a short period of 5 s. Previous studies using nanoprecipitation have observed that at lower driving forces there were oscillations in the current, due to small nuclei forming and then being apparently removed by translocation due to electrophoresis [250, 248], but this was not observed for any of the voltages tested here, there was considerable nucleation leading to pipette blockage for all three negative potentials applied.

The initial drop in current was not immediate, which may suggest that it takes a few tens of milliseconds for the maximum current to be achieved, as the change in direction of ion current in the system stabilises. At a higher potential a larger ion current was able to flow, and this is almost linearly related to the applied potential, suggesting roughly ohmic behaviour for the range of potentials used.

As the driving force for nucleation was higher for a larger applied potential (higher ion flux), the time taken for the barite particle in the tip opening to achieve a size where it is able to completely block the ion current was much shorter. When the potential was flipped back to positive, slightly different behaviour is also observed. Typically the current reached the maximum possible positive value for transients produced at very low negative potentials, where no observable nucleation occurs, as shown in Figure 6.2, for the case of applying a potential of 0 V.
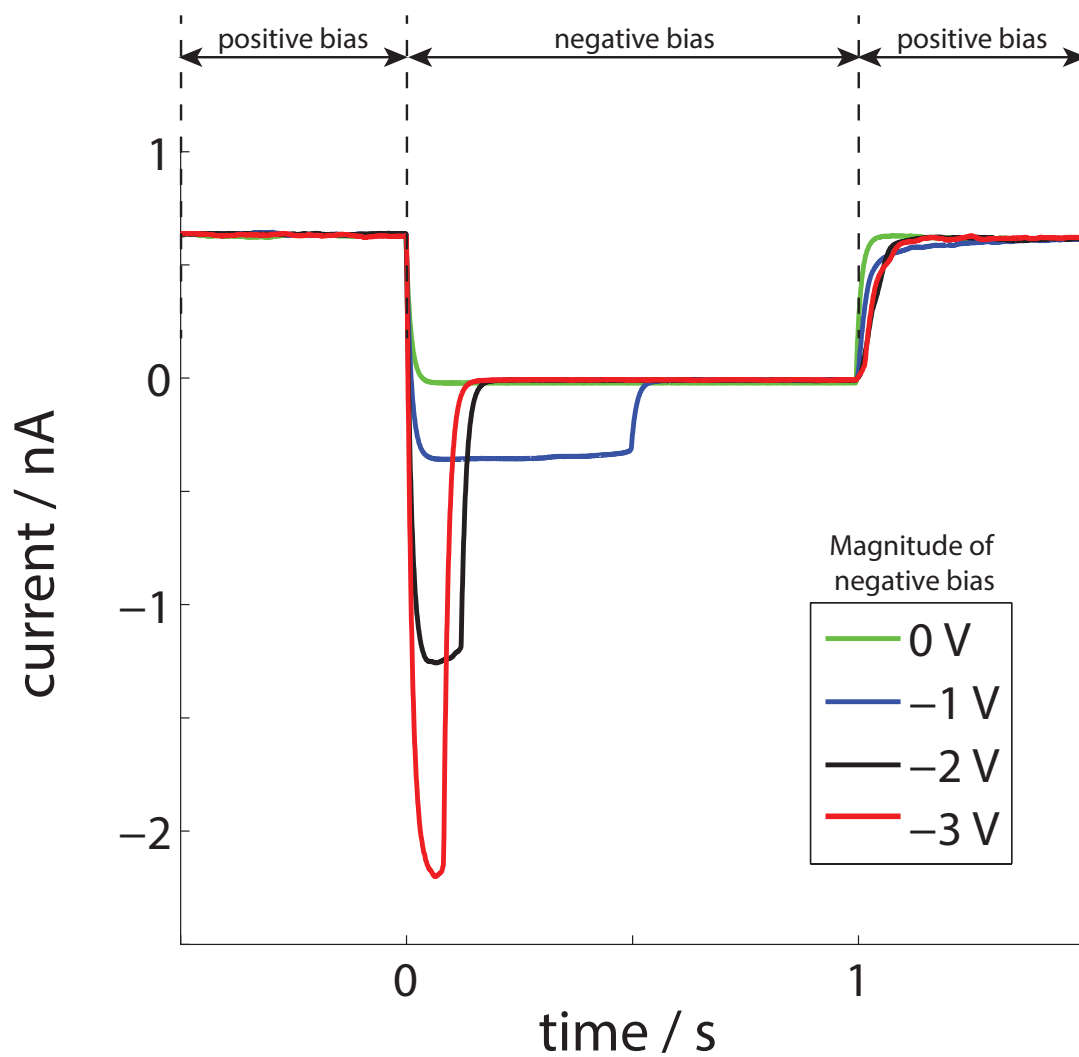
Figure 6.2: Transient observed when the QRCE potential is flipped from a positive potential to a negative one to induce nanoprecipitation, for different applied biases.

At a slightly higher potential, as observed for the case of -1 V, the ejection was more gradual. This is attributed to the fact that complete blocking of the tip has happened under reasonably controlled conditions, with a large induction time. Therefore, the nucleus has had reasonable time during this blocking to grow in all possible dimensions, and the pipette takes slightly longer to clear. When a more negative potential was applied, such as for the transient showing a potential of -3 V, the clearing of the pipette is much more rapid, this could be due to the rapid blockage of the tip, where it is likely that the nanoparticle produced is slightly smaller than those produced under lower negative potentials. However, it is common for the clearing to be delayed for larger potentials, suggesting that for larger ion currents it is possible for crystal growth to continue slightly (possibly in such a way which prevents easy ejection of the particle).

6.3.2 Transients with inhibitors

Figure 6.3 shows the currents observed for several typical experiments, in particular the effect of adding increasing amounts of a phosphonate inhibitor to the bulk solution. It was observed that, in general, as the inhibitor concentration was increased, the time taken for complete blockage of the nanopipette increased also. This suggests that, as would be expected, the inhibitors retarded nucleation and growth of the nanoparticle.

We also observed a clear difference in effectiveness of the two inhibitors. Figure 6.3a
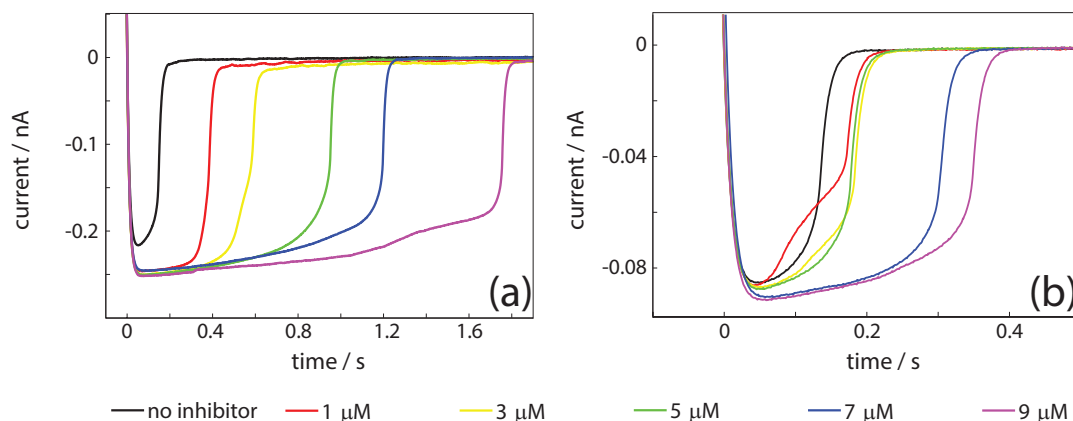
Figure 6.3: Plot showing the current transient observed for different inhibitor concentrations for (a) NTMP and (b) HDTMP.

shows the case where NTMP is used as an inhibitor, whereas HDTMP is shown in Figure 6.3b. HDTMP produced nucleation curves with a considerably shorter period, and therefore retarded growth of barite to a smaller degree than was observed for NTMP. Typically, the observed nucleation time, before the pipette completely blocked the ion current was about 3 or 4 times longer when NTMP was used compared to the same experiment with equivalent concentration of HDTMP.

This is contrary to a study in literature which suggested that HDTMP is shown to be a more effective inhibitor for barite crystallisation [242]. The reasoning behind this is likely to be due to the structure of the molecules of HDTMP and NTMP, shown in Figure 6.4. Both have in common the phosphate groups, NTMP contains 3 per molecule, and HDTMP contains 4 per molecule. However, the key to the difference in their behaviour is in the carbon backbone in the HDTMP molecule. HDTMP is sold as a chelating agent and so works by chelating barium ions in solution [251]. However, there is some discussion in literature as to whether this is, in fact, the

correct mechanism, and it is also observed that the chain length of HDTMP is similar to the barium ion spacing in the crystal structure of barite. Therefore, some consider that it is possible that HDTMP molecules can dock on to the structure of barite itself [239, 225, 117], and prevent further growth once the nucleation has been initiated.

The pK_a values of the inhibitors are shown in Figure 6.1 [252, 236] and their structure is shown in Figure 6.4. It is seen from this that the inhibitor molecules in solution, in the presence of Trizma-HCl, held at pH 7, are likely to be largely protonated. NTMP molecules were very likely to have dissociation of two protons, from two separate phosphonate groups (Figure 6.4a (i)), and some molecules will have a third deprotonation site on the third (Figure 6.4a (ii)). HDTMP is most likely to either have all phosphonate groups deprotonated (Figure 6.4b (i)), and an additional nitrogen atom deprotonated (Figure 6.4b (ii)).

Therefore, it is unlikely that the difference in the effectiveness of the inhibitors is due to their different pK_a, and are not too affected by the electric field applied, which means that the inhibitor concentration close to the pipette opening is likely to be very low indeed, especially compared to the much larger concentration of barium ions in this region. Therefore, this experiment is believed to be a better test of whether the inhibitive properties of HDTMP is determined by the ability of the phosphonate groups to form a metal centred-complex in solution, or by latching onto the crystal structure. The fact that the HDTMP is shown to be much less active as

an inhibitor suggests that the latter is also important process for the effectiveness of this additive. However, the fact that there is an increase in the typical nucleation period observed suggests that chelation also plays a role.

We furthermore consider that for all of the examples discussed above, nucleation and growth was observed over times longer than several minutes, and the experiments performed herein were done over a shorter time regime and observed the first stages of nucleation. It is likely to be that particular inhibitors were more effective at preventing those initial stages of nucleation, and others are more effective at preventing already established nuclei from growing further. Therefore it is predicted that HDTMP was more effective, because it can easily dock onto barite crystals which have well established faces, but, prior to this stage, NTMP appears to be more effective at blocking nucleation.

Table 6.1: Table showing pK_a values of inhibitors used during nanoprecipitation [252].

pK_a	**NTMP**	**HDTMP**
1	12.30	11.82
2	6.66	7.71
3	5.46	6.23
4	4.30	5.68
5		5.12
6		3.25

On the other hand, the NTMP was shown in these experiments to be an excellent inhibitor, and should not be disregarded. The reasoning above suggests that the NTMP molecules in solution do bind to barium ions in solution. The molecule con-
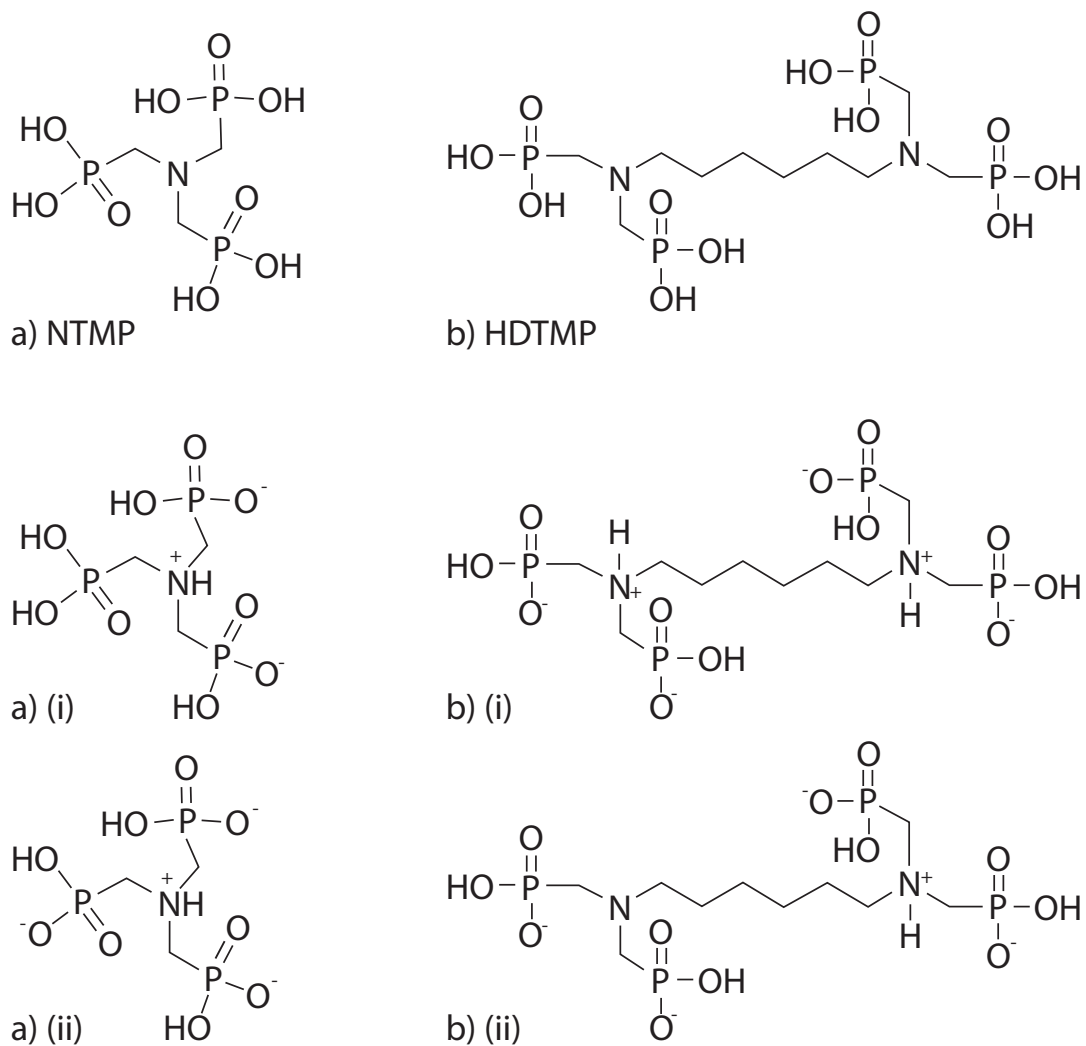
Figure 6.4: Molecular structures of NTMP and HDTMP kinetics. (i) and (ii) show likely charge distributions for each molecule at pH 7.
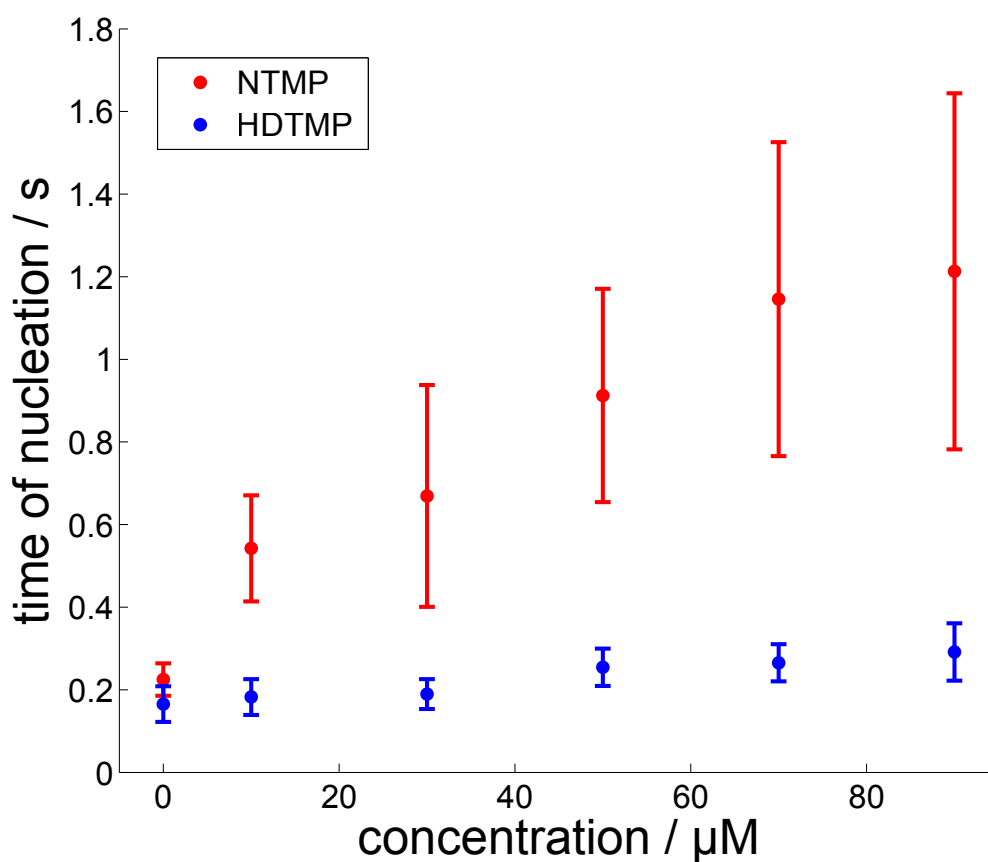
Figure 6.5: Plot showing the time for complete blocking of a nanopipette when different concentrations of inhibitor are added to the bulk solution containing barium ions.

sisted of a nitrogen atom covalently bonded to three phosphate groups. These three groups are in much closer proximity than the case where an alkyl chain separates the phosphonate side groups. On the other hand, previous work suggested that this also puts increased strain on the nitrogen-phosphorus bonds, which means that NTMP is likely to degrade over time when exposed to various conditions, such as heating and sunlight [242]. Therefore, despite having good inhibiting properties initially, it may be found that this rapidly deteriorates, making HDTMP a better choice over long periods of time.

Figure 6.5 illustrates how altering the inhibitor concentration in bulk solution changes the time taken for the pipette tip to become completely blocked. The error bars are mostly due to the fact that this is a stochastic process and each event is different. Although there was a general trend that as the inhibitor concentration increases, so does the nucleation period. Therefore, this is an interesting way of screening the inhibitive behaviour of additives on a crystal growth process.

6.3.3   Two stages of the crystal nucleation

The variation in nucleation time becomes much larger when more inhibitor was added to solution. For example, in Figure 6.3 b, for the case where 1 μM of HDTMP was added to bulk solution, rather than seeing a smooth transition from a negative current to zero, the transient had a 'double-humped' feature. This was observed in several other cases, when inhibitors were added, and a typical example is shown in Figure 6.6a. Figure 6.1 shows a schematic of what happened when a negative potential was applied and a nanoprecipitate formed in the tip, however, it may be possible to predict more specifically how this occurs.

The schematic in Figure 6.1 assumes that the precipitation occurred in the centre of the pipette. It is possible also that the particle developed closer to the glass capillary. The schematic also assumes spherical nucleation, like that modelled in CNT (See Section 1.2.2. This is probably a fair approximation at very primitive stages in the nucleus formation, but as the crystal became more established certain

directions of crystal growth may have become more important.

We established in the previous chapter that growth and nucleation occurs more readily on surfaces with a positive charge than a negative charge. Therefore it is fair to assume that the nucleus formed might have a negative surface charge overall. This assumption is further supported by the fact that the concentration of Na_2SO_4 in the pipette was much higher than the barium concentration in solution. During nucleation, the QRCE inside the pipette behaves as a cathode, and ejected particles would tend to travel inside the nanopipette. Due to the fact that an increase in the current magnitude during nanoprecipitation is never observed, it can be assumed that this never happened, due to the fact that nanoprecipitation was rapid and the particle quickly became large enough that it did not move easily by electrophoresis. However, when the potential was flipped and the particle dissolved, the QRCE inside the pipette became an anode, and the negatively charged particle would either dissolve completely or be ejected out of the pipette. Therefore, barite should not accumulate in the capillary, and the tip can be used repeatedly for several nucleation events.

Now to consider what will happen when nucleation is less rapid, such as the cases where there is a high inhibitor concentration. It is possible that the particle will be affected by electrophoresis to some extent, and this may cause the particle to drift slowly towards the cathode whilst still growing, as is illustrated in Figure 6.6b, (Step 1). The tip of the capillary is more open as a result, and the measured cathodic
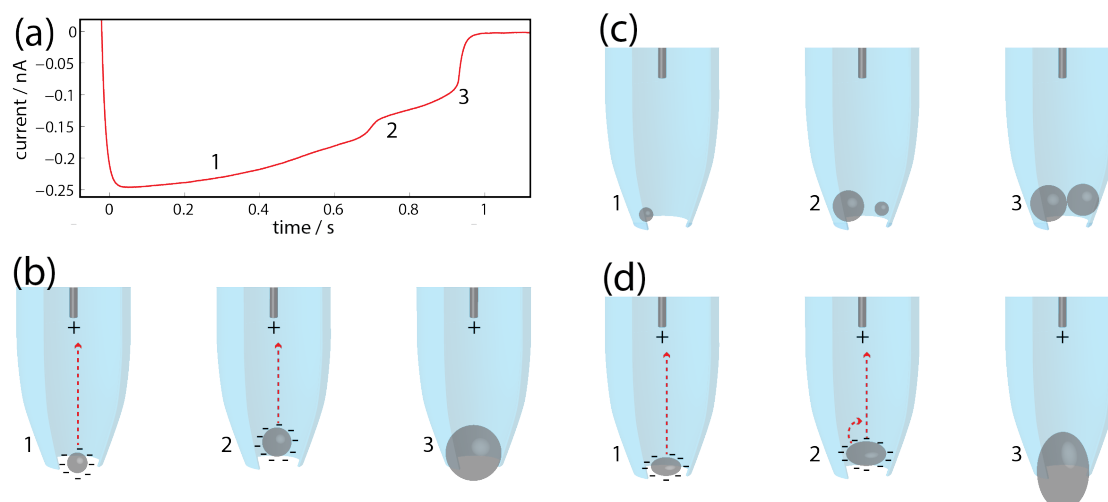
Figure 6.6: Schematics which speculate the cause of 'double-humped' nanoprecipitation transients. (a) The form of a typical transient where nucleation is not straightforward, with a concentration of 5 µM of HDTMP in bulk solution. (b) The electrophoresis of a nanoprecipitate which then slows and blocks the pipette completely as it becomes larger. (c) The occurrence of more than one nucleus in the pipette during the blockage. (d) The occurrence of an irregular morphology which rotates during the nanoprecipitation process.

current stops decreasing in magnitude (Step 2). When the particle's size becomes significant enough that this effect becomes negligible, the particle can continue to grow and block the tip completely (Step 3). This is one possible explanation for this double nucleation event.

A second explanation could be that there is more than one nucleus formed, as illustrated in Figure 6.6c. Although nucleation is more likely for low inhibitor concentrations, once an event occurs it is very rapid and the particle will grow very quickly to fill the tip. In this short time, there is not chance for another nucleus to form. For the case where more inhibitor is added, crystal growth happens more slowly and there is a chance that a second nanoprecipitate will form (Step 2). Once established, the second nanoparticle continues to grow, which will retard growth of

the first. Eventually the volume occupied by the two nanoparticles, collectively, will be large enough to result in complete blockage of the tip (Step 3).

A final explanation is that the primitive form of the nucleus can be considered to be approximately spherical initially, but when it becomes more established it develops a morphology which is more typical of barite micro-crystals. Barite crystals studied at a slightly larger scale generally have a tabular structure and are elongated on the (001) face. It is possible that the particle will become elongated with time, as is shown in Figure 6.6 d (Step 1) and then electrophoresis will cause it to rotate and continue growing with a different orientation (Step 2). This rotation is observed as a second event in the transient.

A further correlation which is observed, apart from this behaviour being more apparent at higher inhibitor concentrations, is that the occurrence of this feature in the transient was observed more regularly when HDTMP rather than NTMP was used. This could simply be due to the fact that longer nucleation times were observed for this inhibitor, and there was thus more chance of one of these processes occurring.

6.4 Conclusion

These initial results show that nanoprecipitation in a nanopipette is an effective technique for monitoring early stage nucleation and crystal growth, and the transients produced reveal features that may provide considerable insight into the process of

nucleation and blockage of the tip. It is also an effective way of screening how well an additive can inhibit a crystal growth process, and of showing how different inhibitors perform against one another. However, the process is stochastic with large variation in the i-t responses, making many multiple measurements necessary.

We saw in this study that NTMP, which contained no hydrocarbon component, was a more effective inhibitor under these circumstances than HDTMP, which contains a hexyl chain between phosphonate groups. This suggested that the ability of HDTMP to form metal complexes is not as important a consideration as previously believed. Also observed are current-time transients of different forms, and although it is not possible to definitively identify the cause of this, it is speculated that under certain conditions, blockage of the nanopipette cannot always be explained by straightforward growth of one spherical nanoparticle.

For the application of offshore oil rigs, it is further confirmed, in addition to extensive further literature, that the use of these phosphonate inhibitors is an important consideration to prevent the formation of barite scale. The method of using nanopipettes to monitor these nucleation processes and screen inhibitors is shown to be a promising one, and is one which can be developed further and applied to many other crystal systems.

CHAPTER 7

CONCLUSIONS

The aim of this thesis was to investigate crystal growth and dissolution, using techniques which allowed for study of the microscopic properties of crystals and analysed the nature of the solid/liquid interface, particularly the crystal surface. A key theme throughout the thesis has been the combination, theory and modelling of mass transport and surface kinetics. Each system has been optimised so that the mass transport between the crystal surface and bulk solution is as high as possible, with the prospect of observing systems where the measurements taken are representative of the surface behaviour of the crystal in question. Most of these studies have been supported by taking advantage of FEM modelling, which allowed for a detailed representation of concentration and mass transport within the experimental geometry, and therefore facilitated the separation of mass transport effects in the

studies.

There has been an emphasis on systems which have an application to industrial processes, and, to that end, two systems have been studied. The first of these systems looks at the case of salicylic acid, which is an organic crystal with pharmaceutical applications, and the second is barite, which forms scale on oil wells, causing problems for their maintenance. These cases allowed for a great range of aspects of crystal dissolution and growth to be studied, due to different applications of each system to their relevant industries. For example, for crystals with pharmaceutical applications, the important areas to investigate are control over crystal growth rate and morphology, in order to produce a consistent dose, and analysis of crystal dissolution in order to predict the bioavailability of the drug. For the case of oil well scaling, the main research focus in the field of crystal growth is to control the nucleation and growth by use of inhibitors in order to prevent the formation of barite scale.

The first study in Chapter 3 discussed the growth and dissolution of salicylic acid and used a simple optical microscope to visualise the changing dimensions of a single crystal using in-situ measurements. From these measurements, the individual crystal was modelled using a FEM simulation, and the surface behaviour of specific faces was determined. This allowed for observation of the fact that there was a great difference in reality between particular faces and that this greatly influenced the rate of diffusion towards the different crystal faces. It was shown that the (001) face was

particularly active and that for crystals of the dimensions discussed in this chapter, the mass transport rate was low enough that true surface behaviour could not be observed. However, less active faces showed less dependence on mass transport, and the system was much closer to being surface controlled. The existence of hollow features in crystals was also briefly discussed, where high index faces appear in the most active (001) face. The theories surrounding this mechanism are also greatly supported by simulation, as it is shown that for active faces with low mass transport, the growth rate near the edges of the face are much higher than centrally, driving localised pitting due to local undersaturation.

The investigation into salicylic acid was continued in Chapter 4, using an UME to probe a particular face of the crystal. It was found that by approaching the crystal using HIC-SECM, proton reduction at the UME surface could be used to induce dissolution when the UME tip was in very close proximity of the crystal surface, as was reflected by the difference in the form of the approach curve, compared to approach towards an inert surface. A complete approach curve was modelled for a variety of theoretical rate constants, for a first order dissolution process, using FEM. The surprisingly low calculated dissolution rate constant, paired with the lack of pitting on optical microscope experiments, suggests that initial dissolution from the basal surface was measured and the system does not reach a stage where high index faces are revealed and pits form on the surface, which evidently greatly enhances the dissolution rate.

Chapter 5 studies barite nucleation and growth using a hydrodynamic cell on a foreign surface. Two surfaces, one with a positive charge, and one with a negative surface charge, were investigated. A high flow, to encourage high mass transport, was applied and the surface was visualised using optical microscopy. By image processing deposition on the surface could be tracked, and calculate the predicted mass transport flux on the surface from this result. This was close to the measured value for the case of PLL at long times, the positively charged surface, which exhibited a higher deposition rate than the case of PGA.

The investigation into barite was further developed by some initial investigations into nanoprecipitation in Chapter 6, where a strong ion current was applied to produce a high concentration of barium sulphate at the tip opening. From these measurements it was possible to observe very early stages of nucleation, using the small dimensions of a nanopipette to contain the crystal and prevent growth beyond this early stage. Although the process was stochastic, there was a general trend between the concentration of a particular inhibitor in solution, and the time-scale of nucleation and complete blockage of the nanopipette, it was also possible to compare the effectiveness of two different inhibitors. This work was extended by discussing what further processes might occur during nucleation, which may have been responsible for variations in the transients observed.

As mentioned earlier, these systems result in observations regarding the microscopic behaviour of the crystals observed, but on various scales. The initial work on salicylic

acid in Chapter 3 observes crystals with dimensions of between 100-200 µm, and tracks changes of tens of µm in the crystal dimensions. The study with SECM in Chapter 4 uses crystals of similar dimensions, but due to the use of an UME to probe the surface kinetics, the scale over which observations are made is much smaller, with a resolution determined by the UME, on the µm scale. In Chapter 5, growth over a large area of hundreds of µm is averaged, although individual nuclei as small as a few µm could be distinguished. Finally, in Chapter 6, the size that the nucleus can achieved is limited by the opening of the pipette, meaning that it is possible to observe particles of up to 100 nm. This ability to observe fundamental crystal growth at a range of length-scales means that macroscopic and microscopic behaviourcould be spanned.

Aside from the final study in Chapter 6, FEM was used to support the theories proposed. It was found that in all cases this strengthened the arguments made. In Chapter 3 it would have been very speculative to assume the mass transport behaviour of salicylic acid crystal faces without calculating the diffusion layer normal to the surface, and the explanation as to the mechanism of hollow features in organic crystals was greatly supported by them. The simulation performed to model approach curves in the HIC-SECM scan in Chapter 4 allowed for the quantification of the dissolution rate constant of the dissolution process. In Chapter 5 the flow cell used was modelled and it was proved that the growth of barite on the surface reaches the kinetically controlled regime once nucleation is produced.

Our final Chapter 6 did not take advantage of FEM but one way in which it could be developed would be to use simulations to investigate what effect different particle shapes and sizes have on the ion current flowing inside the tip, FEM would be ideal to produce this kind of simulation. Nevertheless, these transients are characteristic and show interesting behaviour, and I envisage applying nanoprecipitation to many other crystal systems in the future.

The possible applications of many of the techniques discussed here extend far beyond the systems discussed in this thesis. By visualising and tracking the growth rate of individual faces of a crystal, mass transport can be modelled and the behaviour of the surfaces can be determined. This method can be extended to combine optical microscopy with other methods. For example, by analysing crystals growing in-situ, and imaging using electrochemical techniques such as SICM to determine the height of the crystal, alongside simple optical microscopy. This would prove particularly powerful because it means that all three dimensions are tracked in real time, rather than having to interpolate from ex-situ methods.

Our application of SECM can be applied to any system, but is incredibly valuable when observing crystals which are build from molecules of weak organic acids, due to the fact that it was possible to take advantage of the presence of protons required to allow the crystal to remain in a saturated solution. As was discussed in Chapter 4, it was possible to analyse quantitative kinetics without modification to the electrode by the indused dissolution reaction, and without adding electrolyte material which

may inhibit crystal growth or dissolution.

Research into barite is typically focused around the use of additives to prevent further nucleation and growth, but in Chapter 5 I suggest that making a simple modification to a surface can allow for a great difference in deposition. Therefore, it would be worthwhile for more investigation into whether surfaces could be designed to inhibit growth to a much greater extent, for example by using SAMs. The flow cell system used in this study is an excellent method of testing various surfaces.

To summarise, this thesis shows the considerable scope of fundamental work on crystal nucleation, growth and dissolution. As set out in the goals of my thesis, I have been able to separate mass transport effects from surface kinetics, often down to the observation of single crystals and individual crystal planes. These methods are combined with FEM models which allow for a more detailed insight into the behaviour of these systems, and can be used to calculate quantitative surface kinetic rate constants. There are evidently prospects to further develop some of these methods and apply them to other systems.

REFERENCES

[1] Oaki, Y.; Imai, H. *Cryst. Growth Des.* **2003,** *3,* 711–716.

[2] Cai, A.; Xu, X.; Pan, H.; Tao, J.; Liu, R.; Tang, R.; Cho, K. *J. Phys. Chem. C* **2008,** *112,* 11324–11330.

[3] Addadi, L.; Raz, S.; Weiner, S. *Adv. Mater.* **2003,** *15,* 959–970.

[4] Weiner, S.; Addadi, L. *Trends Biochem. Sci.* **1991,** *16,* 252–256.

[5] Aizenberg, J.; Weaver, J. C.; Thanawala, M. S.; Sundar, V. C.; Morse, D. E.; Fratzl, P. *Science* **2005,** *309,* 275–278.

[6] Smith, B. L.; Schäffer, T. E.; Viani, M.; Thompson, J. B.; Frederick, N. A.; Kindt, J.; Belcher, A.; Stucky, G. D.; Morse, D. E.; Hansma, P. K. *Nature* **1999,** *399,* 761–763.

[7] Naka, K.; Carney, C. K. "Biomineralization I: Crystallization and Self-Organization Process", 2007.

[8] Koutsopoulos, S. *J. Biomed. Mater. Res.* **2002,** *62,* 600–612.

[9] Luquet, G.; Marin, F. *Comptes Rendus Palevol* **2004,** *3,* 515–534.

[10] Meldrum, F. *Internat. Mater. Rev.* **2003,** *48,* 187–224.

[11] Falini, G.; Albeck, S.; Weiner, S.; Addadi, L. *Science* **1996,** *271,* 67–69.

[12] Weiner, S.; Addadi, L. *J. Mater. Chem.* **1997,** *7,* 689–702.

[13] Söhnel, O.; Mullin, J. *J. Cryst. Growth* **1982,** *60,* 239–250.

[14] Teng, H. H.; Dove, P. M.; De Yoreo, J. J. *Geochim. Cosmochim. Acta* **2000,** *64,* 2255–2266.

[15] Walsh, D.; Kingston, J. L.; Heywood, B. R.; Mann, S. *J. Cryst. Growth* **1993,** *133,* 1–12.

[16] Wu, W.; Nancollas, G. H. *Colloids Surf., B* **1997,** *10,* 87–94.

[17] Koutsopoulos, S. *Langmuir* **2001,** *17,* 8092–8097.

[18] Berman, A.; Addadi, L.; Kvick, Å.; Leiserowitz, L.; Nelson, M.; Weiner, S. *Science* **1990,** *250,* 664–667.

[19] Elhadj, S.; De Yoreo, J.; Hoyer, J.; Dove, P. *Proc. Natl. Acad. Sci.* **2006,** *103,* 19237–19242.

[20] Falini, G.; Fermani, S.; Goisis, M.; Manganelli, G. *Cryst. Growth Des.* **2009,** *9,* 2240–2247.

[21] Rieger, J.; Thieme, J.; Schmidt, C. *Langmuir* **2000,** *16,* 8300–8305.

[22] Arellano, M. P.; Aguilera, J. M.; Bouchon, P. *Carbohydr. Res.* **2004,** *339,* 2721–2730.

[23] Ma, C. Y.; Wang, X. Z.; Roberts, K. J. *Adv. Powder Technol.* **2007,** *18,* 707–723.

[24] Wang, X.; Calderon De Anda, J.; Roberts, K. *Chem. Eng. Res. Des.* **2007,** *85,* 921–927.

[25] Davey, R.; Fila, W.; Garside, J. *J. Cryst. Growth* **1986,** *79,* 607–613.

[26] Sweegers, C.; Meekes, H.; Van Enckevort, W.; Hiralal, I.; Rijkeboer, A. *Cryst. Growth Des.* **2004,** *4,* 185–198.

[27] Kovler, K. *Cem. Concr. Res.* **1998,** *28,* 523–531.

[28] ORourke, B.; McNally, C.; Richardson, M. G. *Constr. Build. Mater.* **2009,** *23,* 340–346.

[29] Chindaprasirt, P.; Pimraksa, K. *Powder Technol.* **2008,** *182,* 33–41.

[30] Charola, A. E.; Pühringer, J.; Steiger, M. *Environ. Geol.* **2007,** *52,* 339–352.

[31] Tomson, M. B.; G., F.; Watson, M. A.; Kan, A. T.; U., R. *Symposium on Oilfield Scale* **2002,** .

[32] Sorbie, K.; Laing, N. *Symposium on Oilfield Scale* **2004,** .

[33] Amor, M. B.; Zgolli, D.; Tlili, M.; Manzola, A. *Desalination* **2004,** *166,* 79–84.

[34] Al-Anezi, K.; Hilal, N. *Desalination* **2007,** *204,* 385–402.

[35] Bosbach, D.; Junta-Rosso, J. L.; Becker, U.; Hochella Jr, M. F. *Geochim. Cosmochim. Acta* **1996,** *60,* 3295–3304.

[36] Yang, Q.; Liu, Y.; Gu, A.; Ding, J.; Shen, Z. *J. Colloid Interface Sci.* **2001,** *240,* 608–621.

[37] House, W. A. *J. Colloid Interface Sci.* **1987,** *119,* 505–511.

[38] Garside, J. *Chem. Eng. Sci.* **1985,** *40,* 3–26.

[39] Fujiwara, M.; Nagy, Z. K.; Chew, J. W.; Braatz, R. D. *J. Process Control* **2005,** *15,* 493–504.

[40] Chen, J.; Sarma, B.; Evans, J. M. B.; Myerson, A. S. *Cryst. Growth Des.* **2011,** *11,* 887-895.

[41] Markande, A.; Nezzal, A.; Fitzpatrick, J.; Aerts, L. *Part. Sci. Technol.* **2009,** *27,* 373–388.

[42] Ristic, R.; Finnie, S.; Sheen, D.; Sherwood, J. *J. Phys. Chem. B* **2001,** *105,* 9057–9066.

[43] Rashid, A.; White, E.; Howes, T.; Litster, J.; Marziano, I. *Chem. Eng. Res. Des.* **2012,** *90,* 158–161.

[44] Bard, A. J.; Faulkner, L. R. "Electrochemical methods: fundamentals and applications", 1980.

[45] Ma, C. Y.; Wang, X. Z.; Roberts, K. J. *AIChE J.* **2008,** *54,* 209–222.

[46] Derdour, L.; Sivakumar, C.; Skliar, D.; Pack, S.; Lai, C.; Vernille, J.; Kiang, S. *Cryst. Growth Des.* **2012,** *12,* 5188–5196.

[47] Stapley, A. G.; Himawan, C.; MacNaughtan, W.; Foster, T. J. *Cryst. Growth Des.* **2009,** *9,* 5061–5068.

[48] Land, T.; Malkin, A.; Kuznetsov, Y. G.; McPherson, A.; De Yoreo, J. *Phys. Rev. Lett.* **1995,** *75,* 2774.

[49] Malkin, A.; Land, T.; Kuznetsov, Y. G.; McPherson, A.; DeYoreo, J. *Phys. Rev. Lett.* **1995,** *75,* 2778.

[50] Nielsen, A. E.; Toft, J. M. *J. Cryst. Growth* **1984,** *67,* 278–288.

[51] Mullin, J. W. "Crystallization", 2001.

[52] Boistelle, R.; Astier, J. *J. Cryst. Growth* **1988,** *90,* 14–30.

[53] Sangwal, K. "Additives and Crystallization Processes: From Fundamentals to Applications", 2007.

[54] Leite, E. R.; Ribeiro, C. "Crystallization and growth of colloidal nanocrystals", 2011.

[55] Frenkel, J. *J. Chem. Phys.* **1939,** *7,* 538.

[56] Bennema, P. *J. Cryst. Growth* **1967,** *1,* 287–292.

[57] Larson, M.; Garside, J. *Chem. Eng. Sci.* **1986,** *41,* 1285–1289.

[58] Nỳvlt, J. *J. Cryst. Growth* **1968,** *3,* 377–383.

[59] Myerson, A. "Handbook of industrial crystallization", 2002.

[60] Schmelzer, J. W.; Gutzow, I.; Schmelzer Jr, J. *J. Colloid Interface Sci.* **1996,** *178,* 657–665.

[61] Gebauer, D.; Völkel, A.; Cölfen, H. *Science* **2008,** *322,* 1819–1822.

[62] Clarkson, J. R.; Price, T. J.; Adams, C. J. *J. Chem. Soc., Faraday Trans.* **1992,** *88,* 243–249.

[63] Lacmann, R.; Herden, A.; Mayer, C. *Chem. Eng. Technol.* **1999,** *22,* 279-289.

[64] Nabarro, F. R. "Theory of crystal dislocations", 1967.

[65] Jones, A. G. "Crystallization process systems", 2002.

[66] Kossel, W. *Nachr. Ges. Wiss. Goettingen, Geschaeftliche* **1927,** *1927,* 135–143.

[67] Stranski, I. *Z. Phys. Chem.* **1928,** *136,* 259–278.

[68] Volmer, M.; Schultz, W. *Z. Phys. Chem.* **1931,** *156,* 1–22.

[69] Burton, W.; Cabrera, N. *Discuss. Faraday Soc.* **1949,** *5,* 33–39.

[70] Cabrera, N.; Burton, W. *Discuss. Faraday Soc.* **1949,** *5,* 40–48.

[71] Frank, F. *Discuss. Faraday Soc.* **1949,** *5,* 48–54.

[72] Kwon, Y.-I.; Dai, B.; Derby, J. J. *Prog. Cryst. Growth Charact. Mater.* **2007,** *53,* 167–206.

[73] Teng, H. H.; Dove, P. M.; DeYoreo, J. J. *Geochim. Cosmochim. Acta* **1999,** *63,* 2507–2512.

[74] Dobson, P. S.; Bindley, L. A.; Macpherson, J. V.; Unwin, P. R. *Langmuir* **2005,** *21,* 1255–1260.

[75] Van Kemenade, M.; De Bruyn, P. *J. Colloid Interface Sci.* **1987,** *118,* 564–585.

[76] Bernstein, J.; Davey, R. J.; Henck, J.-O. *Angew. Chem., Int. Ed.* **1999,** *38,* 3440–3461.

[77] Kitamura, M. *Pure Appl. Chem.* **2005,** *77,* 581–591.

[78] Cano, H.; Gabas, N.; Canselier, J. *J. Cryst. Growth* **2001,** *224,* 335–341.

[79] Brittain, H. G. "Polymorphism in pharmaceutical solids", 2009.

[80] Mukuta, T.; Lee, A. Y.; Kawakami, T.; Myerson, A. S. *Cryst. Growth Des.* **2005,** *5,* 1429–1436.

[81] Ostwald, W. "Studies upon the forming and changing solid bodies", 1897.

[82] Lindenberg, C.; Krattli, M.; Cornel, J.; Mazzotti, M.; Brozio, J. *Cryst. Growth Des.* **2008,** *9,* 1124–1136.

[83] Singhal, D.; Curatolo, W. *Adv. Drug Delivery Rev.* **2004,** *56,* 335–347.

[84] Morissette, S. L.; Almarsson, Ö.; Peterson, M. L.; Remenar, J. F.; Read, M. J.; Lemmo, A. V.; Ellis, S.; Cima, M. J.; Gardner, C. R. *Adv. Drug Delivery Rev.* **2004,** *56,* 275–300.

[85] Etter, M. C. *Acc. Chem. Res.* **1990,** *23,* 120–126.

[86] Etter, M. C. *J. Phys. Chem.* **1991,** *95,* 4601–4610.

[87] Stanton, M. K.; Tufekcic, S.; Morgan, C.; Bak, A. *Cryst. Growth Des.* **2009,** *9,* 1344–1352.

[88] McNamara, D. P.; Childs, S. L.; Giordano, J.; Iarriccio, A.; Cassidy, J.; Shet, M. S.; Mannion, R.; O'Donnell, E.; Park, A. *Pharm. Res.* **2006,** *23,* 1888–1897.

[89] Cheney, M. L.; Weyna, D. R.; Shan, N.; Hanna, M.; Wojtas, L.; Zaworotko, M. J. *Cryst. Growth Des.* **2010,** *10,* 4401–4413.

[90] Sheikh, A. Y.; Rahim, S. A.; Hammond, R. B.; Roberts, K. J. *Cryst. Eng. Comm.* **2009,** *11,* 501–509.

[91] Zipp, G. L.; Randolph, A. D. *Ind. Eng. Chem. Res.* **1989,** *28,* 1446–1448.

[92] Su, Y.-F.; Kim, H.; Kovenklioglu, S.; Lee, W. *J. Solid State Chem.* **2007,** *180,* 2625–2629.

[93] Cochran, W. *Acta Crystallogr.* **1953,** *6,* 260–268.

[94] Sundaralingam, M. t.; Jensen, L. *Acta Crystallogr.* **1965,** *18,* 1053–1058.

[95] Nallet, V.; Mangin, D.; Klein, J. *Comput. Chem. Eng.* **1998,** *22,* S649–S652.

[96] Blandin, A.; Mangin, D.; Nallet, V.; Klein, J.; Bossoutrot, J. *Chem. Eng. J.* **2001,** *81,* 91–100.

[97] Franck, R.; David, R.; Villermaux, J.; Klein, J. *Chem. Eng. Sci.* **1988,** *43,* 69–77.

[98] Tavare, N. S.; Gaikar, V. G. *Ind. Eng. Chem. Res.* **1991,** *30,* 722–728.

[99] Coles, B. A.; Compton, R. G.; Suárez, M.; Booth, J.; Hong, Q.; Sanders, G. H. *Langmuir* **1998,** *14,* 218–225.

[100] Wilkins, S. J.; Suárez, M. F.; Hong, Q.; Coles, B. A.; Compton, R. G.; Tranter, G. E.; Firmin, D. *J. Phys. Chem. B* **2000,** *104,* 1539–1545.

[101] Wilkins, S. J.; Coles, B. A.; Compton, R. G.; Cowley, A. *J. Phys. Chem. B* **2002,** *106,* 4763–4774.

[102] Perry, A. R.; Peruffo, M.; Unwin, P. R. *Cryst. Growth Des.* **2013,** *13,* 614–622.

[103] Sorbie, K.; Mackay, E. *J. Pet. Sci. Eng.* **2000,** *27,* 85–106.

[104] Benton, W. J.; Collins, I. R.; Grimsey, I. M.; Parkinson, G. M.; Rodger, S. A. *Faraday Discuss.* **1993,** *95,* 281–297.

[105] Hill, R. *Can. Mineral.* **1977,** *15,* 522–526.

[106] Heywood, B. R.; Mann, S. *J. Am. Chem. Soc.* **1992,** *114,* 4681–4686.

[107] Christy, A. G.; Putnis, A. *Geochim. Cosmochim. Acta* **1993,** *57,* 2161–2168.

[108] Liu, S.; Nancollas, G.; Gasiecki, E. *J. Cryst. Growth* **1976,** *33,* 11–20.

[109] Eun, H.; Umezawa, Y. *Anal. Chim. Acta* **1998,** *375,* 155–165.

[110] Rautaray, D.; Kumar, A.; Reddy, S.; Sainkar, S.; Sastry, M. *Cryst. Growth Des.* **2002,** *2,* 197–203.

[111] Ulman, A. *Chem. Rev.* **1996,** *96,* 1533–1554.

[112] Black, S. N.; Bromley, L. A.; Cottier, D.; Davey, R. J.; Dobbs, B.; Rout, J. E. *J. Chem. Soc., Faraday Trans.* **1991,** *87,* 3409–3414.

[113] Barouda, E.; Demadis, K. D.; Freeman, S. R.; Jones, F.; Ogden, M. I. *Cryst. Growth Des.* **2007,** *7,* 321-327.

[114] Jones, F.; Richmond, W. R.; Rohl, A. L. *J. Phys. Chem. B* **2006,** *110,* 7414–7424.

[115] Mavredaki, E.; Neville, A.; Sorbie, K. S. *Cryst. Growth Des.* **2011,** *11,* 4751–4758.

[116] Pina, C. M.; Becker, U.; Risthaus, P.; Bosbach, D.; Putnis, A. *Nature* **1998,** *395,* 483–486.

[117] Sánchez-Pastor, N.; Pina, C. M.; Fernández-Díaz, L.; Astilleros, J. M. *Surf. Sci.* **2006,** *600,* 1369–1381.

[118] Risthaus, P.; Bosbach, D.; Becker, U.; Putnis, A. *Colloids Surf., A* **2001,** *191,* 201–214.

[119] Kowacz, M.; Putnis, C.; Putnis, A. *Geochim. Cosmochim. Acta* **2007,** *71,* 5168–5179.

[120] Atkins, P.; De Paula, J. "Atkins' physical chemistry", 2014.

[121] Newton, M. D.; Sutin, N. *Annu. Rev. Phys. Chem.* **1984,** *35,* 437–480.

[122] Sun, P.; Mirkin, M. V. *Anal. Chem.* **2006,** *78,* 6526–6534.

[123] Aoki, K.; Osteryoung, J. *J. Electroanal. Chem. Interfacial Electrochem.* **1981,** *122,* 19–35.

[124] Li, R.; Thomson, G.; White, G.; Wang, X.; De Anda, J. C.; Roberts, K. *AIChE J.* **2006,** *52,* 2297–2305.

[125] Gasteiger, H. A.; Markovic, N. M.; Ross Jr, P. N. *J. Phys. Chem.* **1995,** *99,* 8290–8301.

[126] Opekar, F.; Beran, P. *J. Electroanal. Chem. Interfacial Electrochem.* **1976,** *69,* 1–105.

[127] Orton, R.; Unwin, P. R. *J. Chem. Soc., Faraday Trans.* **1993,** *89,* 3947–3954.

[128] Wilkins, S. J.; Compton, R. G.; Taylor, M. A.; Viles, H. A. *J. Colloid Interface Sci.* **2001,** *236,* 354–361.

[129] Zhan, D.; Yang, D.; Zhu, Y.; Wu, X.; Tian, Z.-Q. *Chem. Commun.* **2012,** *48,* 11449–11451.

[130] Chen, C.-C.; Zhou, Y.; Baker, L. A. *Annu. Rev. Anal. Chem.* **2012,** *5,* 207–228.

[131] Mezour, M. A.; Morin, M.; Mauzeroll, J. *Anal. Chem.* **2011,** *83,* 2378–2382.

[132] Basha, C. A.; Rajendran, L. *Int. J. Electrochem. Sci* **2006,** *1,* 268–282.

[133] Kwak, J.; Bard, A. J. *Anal. Chem.* **1989,** *61,* 1794–1799.

[134] Ballesteros Katemann, B.; Schulte, A.; Schuhmann, W. *Chem. - Eur. J.* **2003,** *9,* 2025–2033.

[135] Bard, A. J.; Fan, F. R. F.; Kwak, J.; Lev, O. *Anal. Chem.* **1989,** *61,* 132–138.

[136] Seegmiller, J. C.; Buttry, D. A. *Journal of The Electrochemical Society* **2003,** *150,* B413–B418.

[137] Cortés-Salazar, F.; Momotenko, D.; Girault, H. H.; Lesch, A.; Wittstock, G. *Anal. Chem.* **2011,** *83,* 1493–1499.

[138] Sun, P.; Mirkin, M. V. *Anal. Chem.* **2007,** *79,* 5809–5816.

[139] Mirkin, M. V. *Anal. Chem.* **1996,** *68,* 177A–182A.

[140] Lazenby, R. A.; McKelvey, K.; Unwin, P. R. *Anal. Chem.* **2013,** .

[141] Hansma, P.; Drake, B.; Marti, O.; Gould, S.; Prater, C. *Science* **1989,** *243,* 641–643.

[142] Pastré, D.; Iwamoto, H.; Liu, J.; Szabo, G.; Shao, Z. *Ultramicroscopy* **2001,** *90,* 13–19.

[143] Morris, C. A.; Friedman, A. K.; Baker, L. A. *Analyst* **2010,** *135,* 2190–2202.

[144] Novak, P. *et al. Nat. Methods* **2009,** *6,* 279–281.

[145] Takahashi, Y.; Murakami, Y.; Nagamine, K.; Shiku, H.; Aoyagi, S.; Yasukawa, T.; Kanzaki, M.; Matsue, T. *Phys. Chem. Chem. Phys.* **2010,** *12,* 10012–10017.

[146] Shevchuk, A. I.; Gorelik, J.; Harding, S. E.; Lab, M. J.; Klenerman, D.; Korchev, Y. E. *Biophys. J.* **2001,** *81,* 1759–1764.

[147] Mertz, J. "Introduction to optical microscopy", 2010.

[148] Chartier, G. "Introduction to optics", 2005.

[149] Bauer, W. **2011,** *311,* 012030.

[150] Meyer, E. *Prog. Surf. Sci.* **1992,** *41,* 3–49.

[151] Kuznetsov, Y. G.; Malkin, A.; McPherson, A. *J. Cryst. Growth* **1999,** *196,* 489–502.

[152] McPherson, A.; Malkin, A.; Kuznetsov, Y. G.; Plomp, M. *Acta Crystallogr. , D* **2001,** *57,* 1053–1060.

[153] Binnig, G.; Quate, C. F.; Gerber, C. *Phys. Rev. Lett.* **1986,** *56,* 930.

[154] Hembacher, S.; Giessibl, F. J.; Mannhart, J.; Quate, C. F. *Proc. Natl. Acad. Sci.* **2003,** *100,* 12539–12542.

[155] Torii, A.; Sasaki, M.; Hane, K.; Okuma, S. *Meas. Sci. Technol.* **1996,** *7,* 179.

[156] Tipler, P. A.; Mosca, G. "Physics for scientists and engineers", 2007.

[157] Anton, S. R.; Sodano, H. A. *Smart Mater. Struct.* **2007,** *16,* R1.

[158] Polla, D. L.; Francis, L. F. *Annu. Rev. Mater. Sci.* **1998,** *28,* 563–597.

[159] Rushbrooke, G.; Wood, P. *Mol. Phys.* **1958,** *1,* 257–283.

[160] Sodano, H. A.; Inman, D. J.; Park, G. *Shock and Vibration Digest* **2004,** *36,* 197–206.

[161] Shankar, R.; Shankar, R.; Shankar, R. "Principles of quantum mechanics", 1994.

[162] Hansma, P. *et al. App. Phys. Lett.* **1994,** *64,* 1738–1740.

[163] Hölscher, H. *Encycl. Nanotechnol.* **2012,** 99–99.

[164] Radmacher, M.; Tillamnn, R.; Fritz, M.; Gaub, H. *Science* **1992,** *257,* 1900–1905.

[165] Babuška, I.; Banerjee, U.; Osborn, J. E. *Int. J. Comput. Methods* **2004,** *1,* 67–103.

[166] Wightman, R.; Wipf, D.; Bard, A. *Electroanal. Chem.* **1989,** *15,*.

[167] McKelvey, K.; Edwards, M. A.; Unwin, P. R. *Anal. Chem.* **2010,** *82,* 6334–6337.

[168] Unwin, P. R.; Macpherson, J. V. *Chem. Soc. Rev.* **1995,** *24,* 109–119.

[169] Onuma, K.; Kameyama, T.; Tsukamoto, K. *J. Cryst. Growth* **1994,** *137,* 610–622.

[170] Vekilov, P.; Kuznetsov, Y. G.; Chernov, A. *J. Cryst. Growth* **1992,** *121,* 643–655.

[171] Danesh, A.; Connell, S. D.; Davies, M. C.; Roberts, C. J.; Tendler, S. J.; Williams, P. M.; Wilkins, M. *Pharm. Res.* **2001,** *18,* 299–303.

[172] Vavouraki, A. I.; Putnis, C. V.; Putnis, A.; Koutsoukos, P. G. *Cryst. Growth Des.* **2009,** *10,* 60–69.

[173] Shenoy, D. B.; Sukhorukov, G. B. *Eur. J. Pharm. Biopharm.* **2004,** *58,* 521–527.

[174] Van Driessche, A. E.; Otálora, F.; Sazaki, G.; Sleutel, M.; Tsukamoto, K.; Gavira, J. A. *Cryst. Growth Des.* **2008,** *8,* 4316–4323.

[175] Calderon De Anda, J.; Wang, X.; Roberts, K. *Chem. Eng. Sci.* **2005,** *60,* 1053–1065.

[176] Briançon, S.; Colson, D.; Klein, J. *Chem. Eng. J.* **1998,** *70,* 55–64.

[177] Subero-Couroyer, C.; Mangin, D.; Rivoire, A.; Blandin, A.; Klein, J. *Powder Technol.* **2006,** *161,* 98–109.

[178] Haleblian, J.; McCrone, W. *J. Pharm. Sci.* **1969,** *58,* 911–929.

[179] Land, T. A.; Martin, T. L.; Potapenko, S.; Palmore, G. T.; De Yoreo, J. J. *Nature* **1999,** *399,* 442–445.

[180] Mukuta, T.; Lee, A. Y.; Kawakami, T.; Myerson, A. S. *Cryst. Growth Des.* **2005,** *5,* 1429–1436.

[181] Nordström, F. L.; Rasmuson, Å. C. *J. Chem. Eng. Data* **2006,** *51,* 1668–1671.

[182] Xu, Y.; Yin, H.; Lu, Y.; Yin, S.; Wu, H.; Jiang, T.; Wada, Y. *Mater. Lett.* **2006,** *60,* 2873–2876.

[183] Simov, S. *J. Mater. Sci.* **1976,** *11,* 2319–2332.

[184] Natarajan, V.; Subramanian, C.; Ramasamy, P. *J. Mater. Sci. Lett.* **1988,** *7,* 511–512.

[185] Chandrasekharaiah, M.; Krishna, P. *J. Cryst. Growth* **1969,** *5,* 213–215.

[186] Papadopoulos, N.; Avranas, A. *Journal of solution chemistry* **1991,** *20,* 293–300.

[187] Polakovic, M.; Gorner, T.; Villiéras, F.; De Donato, P.; Bersillon, J. L. *Langmuir* **2005,** *21,* 2988–2996.

[188] Compton, R.; Unwin, P. *Philos. Trans. R. Soc., A* **1990,** 1–45.

[189] Kim, J.; Shen, M.; Nioradze, N.; Amemiya, S. *Anal. Chem.* **2012,** *84,* 3489–3492.

[190] Clifford, C. A.; Seah, M. P. *Meas. Sci. Technol.* **2009,** *20,* 125501.

[191] Qin, Z.; Gautieri, A.; Nair, A. K.; Inbar, H.; Buehler, M. J. *Langmuir* **2012,** *28,* 1982-1992.

[192] Romberg, R. W.; Werness, P. G.; Riggs, B. L.; Mann, K. G. *Biochemistry* **1986,** *25,* 1176-1180.

[193] McGeouch, C.-A.; Edwards, M. A.; Mbogoro, M. M.; Parkinson, C.; Unwin, P. R. *Anal. Chem.* **2010,** *82,* 9322-9328.

[194] McGeouch, C.-A.; Peruffo, M.; Edwards, M. A.; Bindley, L. A.; Lazenby, R. A.; Mbogoro, M. M.; McKelvey, K.; Unwin, P. R. *J. Phys. Chem. C* **2012,** *116,* 14892-14899.

[195] Peruffo, M.; Mbogoro, M. M.; Edwards, M. A.; Unwin, P. R. *Phys. Chem. Chem. Phys.* **2013,** *15,* 1956-1965.

[196] Bode, A. A. C.; Jiang, S.; Meijer, J. A. M.; van Enckevort, W. J. P.; Vlieg, E. *Cryst. Growth Des.* **2012,** *12,* 5889-5896.

[197] Wang, X. Z.; De Anda, J. C.; Roberts, K. J.; Li, R.; Thomson, G.; White, G. *KONA Powder Part. J.* **2005,** *23,* 69–85.

[198] Briançon, S.; Colson, D.; Klein, J. *Chem. Eng. J.* **1998,** *70,* 55–64.

[199] Lennart Sjöberg, E.; Rickard, D. *Geochim. Cosmochim. Acta* **1983,** *47,* 2281–2285.

[200] Macpherson, J. V.; Unwin, P. R.; Hillier, A. C.; Bard, A. J. *J. Am. Chem. Soc.* **1996,** *118,* 6445–6452.

[201] Macpherson, J. V.; Unwin, P. R. *J. Phys. Chem.* **1995,** *99,* 14824–14831.

[202] Macpherson, J. V.; Unwin, P. R. *J. Phys. Chem.* **1995,** *99,* 3338–3351.

[203] Macpherson, J. V.; Unwin, P. R. *Anal. Chem.* **2000,** *72,* 276–285.

[204] Macpherson, J. V.; Unwin, P. R. *J. Phys. Chem.* **1994,** *98,* 1704–1713.

[205] Barker, A. L.; Macpherson, J. V.; Slevin, C. J.; Unwin, P. R. *J. Phys. Chem. B* **1998,** *102,* 1586–1598.

[206] Fushimi, K.; Seo, M. *Electrochim. acta* **2001,** *47,* 121–127.

[207] Etienne, M.; Schulte, A.; Mann, S.; Jordan, G.; Dietzel, I. D.; Schuhmann, W. *Anal. Chem.* **2004,** *76,* 3682–3688.

[208] Davies, C. W. *Washington, DC* **1962,** 37–53.

[209] Cowan, J. C.; Weintritt, D. J. "Water-formed scale deposits", 1976.

[210] Land, L. S.; Prezbindowski, D. R. *J. Hydrol.* **1981,** *54,* 51–74.

[211] Moghadasi, J. *et al.* "Scale formation in Iranian oil reservoir and production equipment during water injection", 2003.

[212] Hartman, P.; Perdok, W. *Acta Crystallogr.* **1955,** *8,* 525–529.

[213] Wiechers, H.; Sturrock, P.; Marais, G. *Water Res.* **1975,** *9,* 835–845.

[214] Estes, J. C. *J. Pressure Vessel Technol.* **1978,** *100,* 188–193.

[215] Gu, T.; Su, P.; Liu, X.; Zou, J.; Zhang, X.; Hu, Y. *J. Pet. Sci. Eng.* **2013,** *102,* 41–46.

[216] El Dahan, H.; Hegazy, H. *Desalination* **2000,** *127,* 111–118.

[217] Hoang, T. A.; Ang, M.; Rohl, A. L. *Chem. Eng. Technol.* **2011,** *34,* 1003–1009.

[218] Bader, M. *J. Pet. Sci. Eng.* **2007,** *55,* 93–110.

[219] Oremland, R. S.; Taylor, B. F. *Geochim. Cosmochim. Acta* **1978,** *42,* 209–214.

[220] Li, S.; Xu, J.; Luo, G. *J. Cryst. Growth* **2007,** *304,* 219–224.

[221] Kucher, M.; Babic, D.; Kind, M. *Chem. Eng. Process.: Process Intensification* **2006,** *45,* 900–907.

[222] Dunn, K.; Yen, T. F. *Environ. Sci. Technol.* **1999,** *33,* 2821–2824.

[223] Jones, F.; Jones, P.; Ogden, M. I.; Richmond, W. R.; Rohl, A. L.; Saunders, M. *J. Colloid Interface Sci.* **2007,** *316,* 553–561.

[224] Leung, W. H.; Nancollas, G. H. *J. Inorg. Nucl. Chem.* **1978,** *40,* 1871–1875.

[225] Bosbach, D.; Coveney, P. V.; Griffin, J. L.; Putnis, A.; Risthaus, P.; Stackhouse, S.; Whiting, A. *J. Chem. Soc.* **2002,** 1238–1245.

[226] Heywood, B. R.; Mann, S. *Advanced Mater.* **1994,** *6,* 9–20.

[227] Hopwood, J. D.; Mann, S. *Chem. Mater.* **1997,** *9,* 1819–1828.

[228] Monnin, C.; Galinier, C. *Chem. Geol.* **1988,** *71,* 283–296.

[229] Higgins, S. R.; Jordan, G.; Eggleston, C. M.; Knauss, K. G. *Langmuir* **1998,** *14,* 4967–4971.

[230] Kuwahara, Y. *Geochim. Cosmochim. Acta* **2011,** *75,* 41–51.

[231] Turnbull, D. *Acta Metall.* **1953,** *1,* 684–691.

[232] Higgins, S. R.; Bosbach, D.; Eggleston, C. M.; Knauss, K. G. *J. Phys. Chem. B* **2000,** *104,* 6978–6982.

[233] Peruffo, M. *Functionalisation of surfaces and interfaces: molecules, particles and crystals,* Thesis, University of Warwick, 2010.

[234] Tritton, D. J. *Oxford, Clarendon Press, 1988, 536 p.* **1988,** *1,.*

[235] Taguchi, K.; Garside, J.; Tavare, N. S. *J. Cryst. Growth* **1996,** *163,* 318–328.

[236] Hamza, S. M.; Hamdona, S. K. *J. Chem. Soc., Faraday Trans.* **1992,** *88,* 2713–2716.

[237] Bosbach, D.; Hall, C.; Putnis, A. *Chem. Geol.* **1998,** *151,* 143–160.

[238] He, S.; Kan, A. T.; Tomson, M. B. *Langmuir* **1996,** *12,* 1901–1905.

[239] Rohl, A.; Gay, D.; Davey, R.; Catlow, C. *Jour. Am. Chem. Soc.* **1996,** *118,* 642–648.

[240] Gardner, G.; Nancollas, G. *J. Phys. Chem.* **1983,** *87,* 4699–4703.

[241] Barouda, E.; Demadis, K. D.; Freeman, S. R.; Jones, F.; Ogden, M. I. *Cryst. Growth Des.* **2007,** *7,* 321–327.

[242] Dyer, S.; Anderson, C.; Graham, G. *J. Pet. Sci. Eng.* **2004,** *43,* 259–270.

[243] Wei, C.; Bard, A. J.; Feldberg, S. W. *Anal. Chem.* **1997,** *69,* 4627–4633.

[244] Umehara, S.; Pourmand, N.; Webb, C. D.; Davis, R. W.; Yasuda, K.; Karhanek, M. *Nano Lett.* **2006,** *6,* 2486–2492.

[245] Siwy, Z. S.; Howorka, S. *Chem. Soc. Rev.* **2010,** *39,* 1115–1132.

[246] Cervera, J.; Schiedt, B.; Neumann, R.; Mafé, S.; Ramírez, P. *J. Chem. Phys.* **2006,** *124,* 104706.

[247] Innes, L.; Powell, M. R.; Vlassiouk, I.; Martens, C.; Siwy, Z. S. *J. Phys. Chem. C* **2010,** *114,* 8126–8134.

[248] Powell, M. R.; Sullivan, M.; Vlassiouk, I.; Constantin, D.; Sudre, O.; Martens, C. C.; Eisenberg, R. S.; Siwy, Z. S. *Nature Nanotechnol.* **2007,** *3,* 51–57.

[249] McKelvey, K.; Perry, D.; Byers, J. C.; Colburn, A. W.; Unwin, P. R. *Anal. Chem.* **2014,** *86,* 3639–3646.

[250] Vilozny, B.; Actis, P.; Seger, R. A.; Pourmand, N. *ACS Nano* **2011,** *5,* 3191–3197.

[251] Knepper, T. P. *TrAC, Trends Anal. Chem.* **2003,** *22,* 708–724.

[252] Rizkalla, E. N. *J. Chem. Soc., Faraday Trans. 1* **1983,** *79,* 1857–1867.